The Resistivity Switching of Iron Doped Strontium Titanate Single Crystals and Thin Films.

Marcin Wojtyniak

Institute of Physics, Departament of Biophysics and Molecular Physics

University of Silesia

A thesis submitted for the degree of

Doctor of Philosophy

Work done under the supervisors of: prof. dr hab. Krzysztof Szot and dr hab. Roman Wrzalik, prof. UŚ

2014 July

Acknowledgements

At the beginning I wish to to say "Thank you" to everybody who contributed in any way to this thesis.

First of all, I thank Prof. Krzysztof Szot who was and still is the brain under the successful investigations of many oxide materials, with the special contribution in the strontium titanate. By his guidance I have learned many things, from basic to advanced physics, and the most appreciated - know-how of a productive experiments. What is more I am very grateful for his kindness and care he gave to me.

I would also like to thank Prof. Roman Wrzalik, who greatly contributed to my work and my development as a scientist. He was always ready to help me with anything, and provided plenty of useful comments and suggestions. By I am also grateful for his caring attitude and constant good humor.

I am also grateful to Prof. Jacek Szade for sharing his experience with me, many scientific discussions and all opportunities that he provided.

There are also several friends I would like to thank: Dr. Jurek Kubacki, who introduced me to UHV experiments and for being a kind spirit in the labolatory, Christian Rodenbücher for his friendship and kindness, Dr. Katarzyna Balin for her positive attitude and many good results and Mateusz Dulski for just about everything, starting from the long hours spent together in the office, to the scientific collaboration. The talking, laughing and having a good time at the table tennis were things that I needed greatly.

I am also very grateful to my parents, which were always open minded and supportive for my carrier. I knew that no matter what, they have always been there for me.

Last but not least I am very grateful to two special people: my best friend Adam Dusza and my fiancée Kasia Bilewska. You two always wanted the best for me and I am very grateful for that. Adam thank you for your everlasting friendship and support. Your sense of humor, frighteningly similar to mine, was a source of many great moments. Do not change ever! And Kasia thank you for your constant support and care, you always kept me motivated, both in my work and life. Your very presence is encouraging me to be a better man. Without you any of my work would not be possible.

In the end I humbly acknowledge all support that I received during my study: the SFB 917 funded by the Deutsche Forschungsgemeinschaft and two scholarships: UPGOW and DoktroRIS funded by the European Union through the European Social Funds (ESF).

Contents

List of Figures

List of Tables

Glossary

AFM Atomic Force Microscopy

CEMS Conversion Electron Mössbauer Spectroscopy

DFT Density Functional Theory

HRTEM High Resolution Transmission Electron Microscopy

I-M Insulator - Metal

LC-AFM Local Conductivity Atomic Force Microscopy

LEED Low Energy Electron Diffraction

MS Mössbauer Spectroscopy

PEEM Photoelectron Emission Microscopy

PLD Pulsed Laser Deposition

red-ox reduction oxidation process

RMS Root Mean Square

RRAM Resistive Random Access Memory

RS Resistive Switching

SPM Scanning Probe Microscopy

SQUID Superconducting Quantum Interference Device

STM Scanning Tunneling Microscopy

STO Strontium Titanate

TMO Transition Metal Oxides

TOF-SIMS Time Of Flight Secondary Ion Mass Spectrometry

UHV Ultra High Vacuum

V-I Voltage - Current

VB Valence Band

VCM Valency Change Mechanism

XANES X-ray absorption near-edge spectroscopy

XMCD X-ray Magnetic Circular Dichroism

XPS X-ray Photoelectron Spectroscopy

XRF X-ray Fluorescence Spectroscopy

1

Introduction

Transition metal oxides (TMO) have received a great deal of attention in recent years. They exhibit a variety of physical properties and can be easily produced in single crystals, ceramics and thin films. Due to a number of oxidation states of the transition-metal cation the TMO are one of the most stable compounds. There is an extensive literature about the macroscopic physical properties of many TMO's, however the many details of the microscopic mechanisms and processes remain largely undiscovered. For example the influence of the external stimuli, such as the temperature or electric field, on the surface geometry and electronic structure can be of vital use to many applications. The ABO_3-type perovskites and the strontium titanate - $SrTiO_3$ (STO) in particular, attracted significant attention due to variety of their physical phenomena. The STO is considered as a model material due to extensive literature gathered on its properties. Thanks to high electrical permitivity at room temperature it is also used in electronics(1), especially as an replacement for SiO_2 in Si-based electronics(2). The STO is also being used as an oxygen gas sensors in high temperature(3) or as an anode in ceramic fuel cells(4). Additionally, due to its availability as a relatively large single crystals with appropriate doping, STO is commonly used as a substrate for high T_c superconductors(5). The other possible implementations involves the photocatalists and high temperature superconductors technologies.

Recently, the most prominent application came from the discovered resistive switching (RS) phenomena. The principle of RS can be simply explained as the ability of the material to change the resistivity upon electrical stress in a non-volatile way. This phenomenon is interesting especially from the application point of view, as it can be used as base for new type of memory - the Resistive Ran-

dom Access Memory (RRAM)(6). In fact many binary(7, 8, 9, 10) and ternary transition metal oxides exhibits RS phenomenon(11). Among other, the STO is especially suited for the fundamental research thanks to its simple structure, the possibility to tune electrical properties from insulating through semiconducting to metallic via electrical or chemical gradients (or combination of both) and large available literature. Moreover it was already shown that the RS in the undoped STO has filamentary character(12) and that the defects, especially the oxygen vacancies, are playing crucial role in the RS behavior. Thus from the application point of view the control over the defect density is desirable. One way to obtain such control is to introduce appropriate dopants. For the RRAM applications several different elements were proposed, among other the Nb, La, Fe or Cr were considered(13). What is interesting contrary to the filamentary character of RS phenomena in pure STO, the Nb doped samples of STO exhibited a cluster like switching(14). It was discussed that the ionic movements led to creation of secondary phases in a form of nano-filaments that influenced the RS phenomena.

Recently Fe doping was also proposed to be suitable for applications(15), however the macroscopic and microscopic influence of the doping is not fully understood. Therefore, the main goal of this thesis is to investigate the Fe doped STO single crystals for the origin of RS phenomenon, especially the insulator-to metal transition. Additionally for more practical approach the epitaxial thin films were also characterized. The complexity of the interaction between sample exposed to electrical and chemical gradients (or combination of both) *per se* requires usage of interdisciplinary techniques like physico-chemistry of surface layer and detailed macroscopic characterization. Therefore we focused on general characterization by many techniques, to mention some of them: X-ray Powder Diffraction, X-ray Fluorescence Spectroscopy, X-ray Photoelectron Spectroscopy, Time of Flight Secondary Ion Mass Spectroscopy and Scanning Probe Microscopy.

This work is structured in the following way:

Chapter 1 - This chapter covers the literature introduction into the topic of the Fe doped strontium titanate. Among other the production and the crystallographic structure of investigated samples are presented as well as the defect chemistry and the concept of extended defects. Additionally the resistive switching phenomena along with some examples is shortly discussed. In the end of the chapter the thesis objectives are presented.

Chapter 2 - This chapter is separated into two parts - first the primary characterization techniques are discussed, followed by short review of the secondary characterization techniques. Additionally a detailed discussion concerning the temperature dependent local conductivity atomic force microscopy measurements is given.

Chapter 3 - This chapter covers three topics - first the preliminary characterization of the single crystal STO samples is given, next the influence of the reducing condition is presented, and finally the influence of the oxidizing condition is investigated.

Chapter 4 - This chapter is focused on the reduction and oxidation reactions under the influence of the electric field. The electro-coloration phenomena is discussed and the results from the electrical and optical measurements are shown. Additionally the oxygen vacancy (and oxygen ions) migration is investigated.

Chapter 5 - This chapter, contrary to the previous chapters, is focused on the thin films characterization. Basic investigation of the structure and the electrical behavior is given, followed by a detailed dopant distribution analysis. Additionally some interesting results considering electric and magnetic results are presented.

Chapter 6 - This chapter is the final summary of the presented work along with a short outline of future work.

1.1 Background

Strontium titanate belongs to the group of materials with perovskite structure, a natural mineral from which this group took its name - $CaTiO_3$(16). Perovskites are large group of compounds with the general formula of ABX_3, where A and B are cations and X is oxygen(17). Due to their wide structural and stoichometric stability is commonly considered as a model material(18). Interesting enough, not until 1982 it was thought that the STO was purely artificial, when the International Mineralogical Association recognized it under the name of tausonite(19).

1.1.1 Single crystal preparation method

Currently the most popular method of growing good quality single crystals of STO is so called Verneuil process. This invented in 1902 by the French chemist Auguste Verneuil process is primarily used to produce the ruby and sapphire varieties of corundum, as well as the diamond simulants rutile. Despite some minor modifications Verneuil process remains nearly unchanged, and the majority of synthetic corundum and spinel gemstones are produced by it.

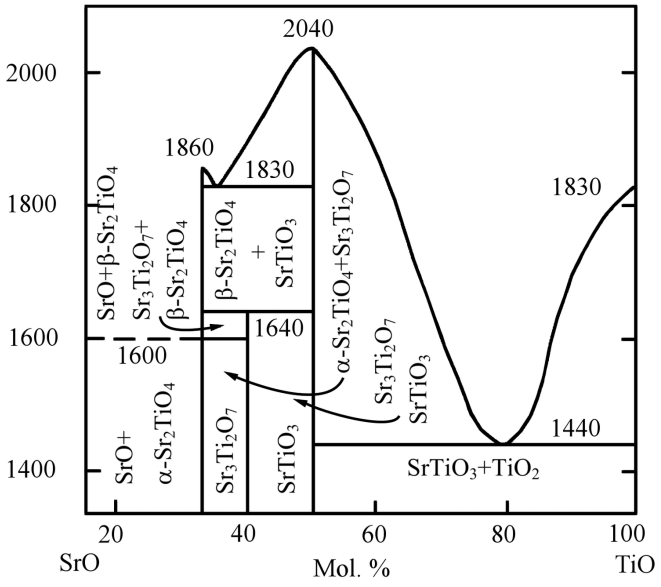

Figure 1.1: Phase diagram the SrO-TiO_2 system. - The phase diagram of $SrTiO_3$ crystal growth(20). The stoichiometry and the temperature range for the formation of pure STO phase is quite narrow.

The principle of the Verneuil process is rather simple, the starting material is first finely powdered and placed in the Verneuil furnace. The furnace has an opening at the bottom, through which the powder can be removed when the container is vibrated. While the material is released, gas oxygen is supplied into the furnace, and travels with the powder down a narrow tube. Second larger tube filled with hydrogen is closed around the narrow one. At the exit of the narrow tube the combustion occurs. The temperature of the flame reaches at least 2300 K. When the material falls through the high temperature region it melts into small droplets, which fall on top of the support placed below. The droplets form a sinter cone, which is liquid on the top. The support is slowly moved away from the flame, which result in crystallization of the colder parts of the cone. The top of the cone remains liquid, and as the new material is added in a form of droplets, the long cylindrical crystal (boule) is formed.

Unfortunately samples produced by this method contains relatively high concentration of defects, mostly dislocations. Other methods, which can give better quality (less defected) crystals are also known, however a higher preparation complexity and longer preparation times are needed. As an example, the time needed to form certain volume of STO crystal by the Vernouil method require 1 day, giving crystals with 10^6 dislocations per cm^2. In contrast, the time needed for the same volume of material using top-seeded solution growth is approximately 1 week with 10^2 dislocations per cm^2, while the flux growth method needs almost 2 months giving dislocation free (optically) crystals - Fig.1.2. Therefore, mostly due to the production costs, the Vernouil method is most popular and widely available. Nevertheless for many applications the quality of the $SrTiO_3$ crystals produced by the Verouil method is sufficiently good. What is important from the experimental point of view is that the Vernouil method provides excellent reproducibility. On the other hand, the Verouil method do not produce the STO crystals with perfect stoichiometry and the post production annealing in high temperature under oxidizing conditions is required. Even so, one has to keep in mind that the growth of good quality STO crystals is challenging task, as the ideal stoichiometry and the temperature range for a pure phase of STO is rather narrow (Fig.1.1).

In this work all investigated single crystals were grown by the Verneuil method. The nominal doping concentrations were equal to: 0.026 %, 0.06 %, 0.13 % and

0.45 % at of Fe. All samples were cut and polished at the manufacturer (CrysTec Germany) along the (100) orientation.

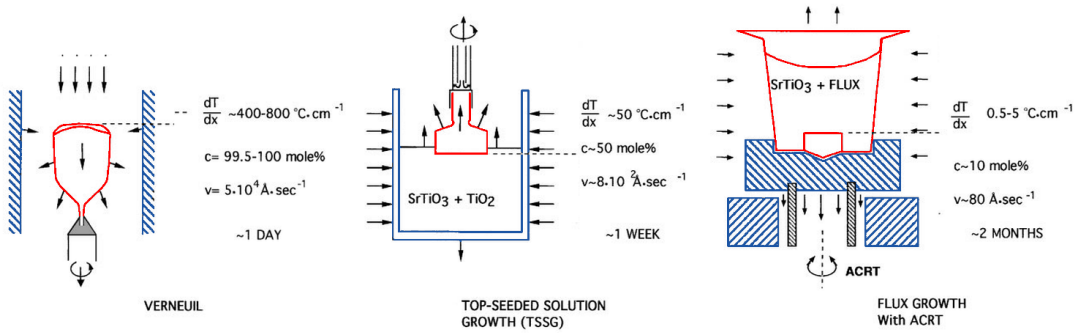

Figure 1.2: Comparison of $SrTiO_3$ single crystal growth methods. - Three typical methods for the single crystal STO growth. The dislocation densities are: Verneuil grown - $10^6/cm^2$, TSSG grown $10^2/cm^2$, and of flux/ACRT-grown - below optical detection resolution.

1.1.2 Crystallographic structure of STO

The $SrTiO_3$ as well as many ternary oxides crystallizes in the perovskite structure presented in the Fig.1.3. At room temperature it accommodates the cubic $pm\bar{3}m$ space group with the cell parameter equal to 0.39056 Å(21). The arrangement of the atoms in the basic cell are: Sr(000), Ti $(\frac{1}{2}\frac{1}{2}\frac{1}{2})$ and O $(0\frac{1}{2}\frac{1}{2}$, $\frac{1}{2}0\frac{1}{2}$ and $\frac{1}{2}\frac{1}{2}0)$. The perfect structure consist of 12 - coordinated A site (cuboctahedral coordination) and 8 - coordinated B site (octahedron coordination) giving rather dense structure, with the theoretical density equal to 5.12 g/cm^3. However, the non-stoichimetry, doping, different oxygen partial pressure or the influence of the temperature cause the BO_6 octahedra to rotate and/or tilt along [001] pseudocubic axis. This can lead to the distortion from the cubic into orthorhombic or a tetragonal structures. The amount of distortion can be quantified by the Goldschmidt tolerance factor t(22) defined by:

$$t = \frac{r_A + r_O}{\sqrt{2} bullet (r_B + r_O)} \tag{1.1}$$

, where r_i is the ionic radius of the ions and the oxygen sites. The ideal cubic perovskite has $t = 1$, which corresponds to $r_A = 1.44$ Å, $r_B = 0.605$ Åand $r_0 = 1.40$ Å. The factor t deviates from 1 depending on the ions in the structure.

In general, for $t < 1$ the BO_6 octahedra will rotate in order to accommodate for the 'empty' space lowering the symmetry, while for $t > 1$ the tetragonal and hexagonal variants of the perovskite structure is possible. In the case of STO (or Fe doped STO with small concentrations $> 0.5\,\%\ at$) the Goldschmidt factor is approximately 0.904, suggesting the existence of slight distortion. Moreover one can notice that in any planar direction (h, k, l) the STO structure always consist of two types of alternating atomic planes, as can be seen in Fig.1.4. For example in the [100] direction the STO structure consists of two sublattices, TiO_2 and SrO. This simple fact is crucial for many physical properties and explains why the STO is compared to TiO_2 system. At 105 K STO undergoes a structural phase transition into tetragonal P4mm system due to the opposite rotation of neighboring oxygen octahedrons. Typically lowering the symmetry allows ferroelectric transition, however the STO belongs to a quantum paraelectrics class, where quantum fluctuations of the atomic positions prevents formation of permanent polarization up to 0 K(23). The STO undergoes two more structural phase transitions: to orthorombic at 55 K(24) and to rhomboedral (25) below 10 K. Beside the structural phase transitions, the STO with sufficiently high electron concentration undergoes transition to a superconducting state at temperature close to 0.4 K(26). The high electron concentration can be reached either by doping, like in Nb doped STO(27), or by self-doping by reduction(28).

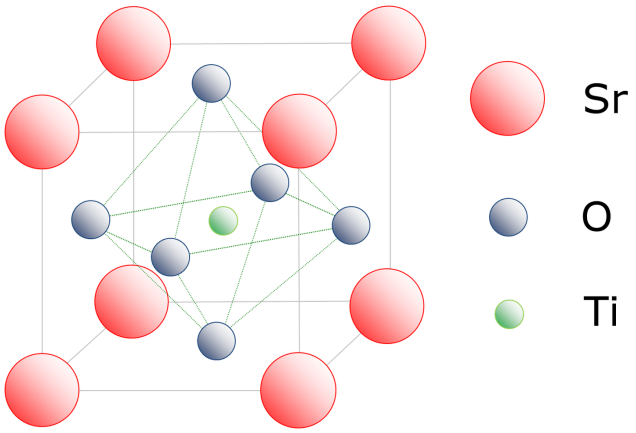

Figure 1.3: Structure of STO. - The unit cell of the cubic perovskite $SrTiO_3$.

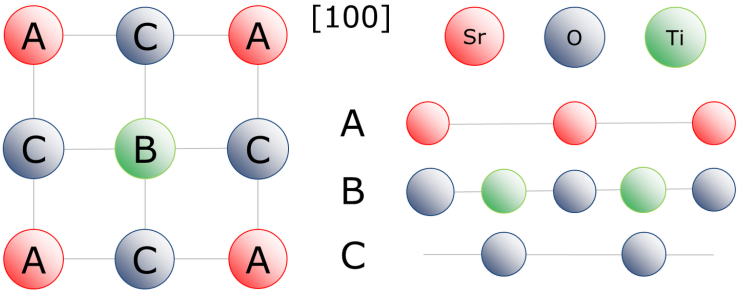

Figure 1.4: Atomic arrangement of STO. - Atomic arrangement for the [100] crystallographic direction. The individual atoms rows are marked by the letters A, B and C.

1.1.3 Defect chemistry of STO

From the thermodynamic point of view, all materials with configuration entropy at any temperature above absolute zero, must contain a finite number of point defects(29). The defects and their influence on the properties of the materials are governed by defect chemistry(30). The defect chemistry proven to be very reliable in many cases, especially in high temperature regime in STO(31, 32, 33). Nevertheless, the range where the defect chemistry can be applied is limited by:

- the defects concentration has to be very low,
- the defects are non-interacting and are distributed homogeneously,
- the movements of the defects is described by the random walk.

Those assumptions may not always be true. One example is the case of the TiO_{2-x} system, where the point defect chemistry is valid only up to x=0.001(34). Above that concentration, the extended defects are being formed (next subsection).

To summarize the defect chemistry of the undoped and acceptor doped $SrTiO_3$ the widely accepted Krger-Vink notation(35) is introduced here:

- only the deviation from the ideal crystal lattice are denoted,
- the main index is either the element symbol or 'V', which represent the vacancy,

- the subscript denotes the occupied site, which can be either an element symbol or 'I' meaning the interstitial site,
- the superscript shows the excess of charge compared to the net lattice charge; the dot symbol ($^{\bullet}$) stands for positive charge, prime symbol ($^{'}$) for negative and x (^{x}) for neutral,
- the concentrations are denoted by taking the components into square brackets [ ].

For example $h^{\bullet}$ is a hole, $e^{'}$ is a electron and $[V_O^{\bullet\bullet}]$ is doubly positive oxygen vacancy. It is worth to mention that in this work only the iron (acceptor) doped samples are investigated. Also even nominally undoped $SrTiO_3$ crystals turns out to be slightly acceptor doped due to impurities from the preparation methods. Therefore, the undoped and the acceptor doped cases will be presented together, while the donor doping case will be omitted. If it comes to structural defects in the perovskites (in the STO in particular), the densely packed crystal lattice favors only certain defects. Those defects are: vacancies in all three sublattices, electrons, holes, and substitutional impurities. It was shown that interstitials play no significant role(36, 37). The cation vacancies are typically treated as a source of small acceptor concentration, since their mobility is very low $<$ 1400K(38). On the other hand the oxygen vacancies are quite mobile even at room temperatures, especially if the extended defects are present in the investigated material(12). In general, many findings suggest that the oxygen vacancies are mostly doubly ionized, therefore neutral and single ionized oxygen vacancies are not taken into an account(32, 39). Moreover, the oxygen vacancies may form a superstructures and order preferentially with respect do local structure. An example of such ordering was reported in the $SrFeO_n$ ($2.5 < n < 3.0$) system, where FeO_5 formed square pyramids with iron on +3 and +4 oxidation states. Other good example of explicit vacancy ordering was found in Ca doped STO by the transmission electron microscopy investigations(40).

Following an excellent introduction into point defect chemistry(41) one can write appropriate defect reactions for the STO material. This section is divided into three approximate temperature regimes since no arbitrary temperature limit can be given for all possible materials: low temperature (T $<$ 500°C), intermediate temperature (500°C to 1000°C), and high temperature (T $<$ 1000°C). In each of those ranges a different exchange reaction is prevailing.

T < 500°C

According to the defect chemistry at low temperatures only the electronic ionization reactions are active. Therefore, only the the creation of electrons and holes by thermal excitation across the band gap can occur:

$$nil \rightleftharpoons e^{'} + h^{\bullet} \tag{1.2}$$

, where law of mass action gives:

$$n \cdot p = K_I(T) = N_C(T) \cdot N_V(T) \cdot e^{-(E_g^0 - \lambda T)/k_B T} \tag{1.3}$$

The n and p are the concentration of electrons and holes. K_I is thermally activated reaction constant, while N_C and N_V are the effective densities of states as a function of temperature and the bottom of conduction band and at the top of valence band respectively. The $E_g^0 - \lambda T$ is the temperature dependence of the band gap. Finally the k_B is Botlzmann constant.

500°C < T < 1000°C

At this temperature range the oxygen vacancies becomes mobile. Thus the oxygen exchange reaction dominates, which is strongly related to the oxygen partial pressure pO_2 by the relation:

$$O_O \rightleftharpoons \frac{1}{2}O_2 + V_O^{\bullet\bullet} + 2e^{'} \tag{1.4}$$

, where law of mass action gives:

$$[V_O^{\bullet\bullet}] \cdot n^2 \cdot (pO_2)^{1/2} = K_{red}(T) = K_{red}^0 \cdot e^{-(\Delta H_{red}/k_B T)} \tag{1.5}$$

The ΔH_{red} is reduction enthalpy.

Depending on the surrounding atmosphere, the oxygen can be incorporated into the lattice following the relation:

$$\frac{1}{2}O_2 + V_O^{\bullet\bullet} \rightleftharpoons O_O + 2h^{\bullet} \tag{1.6}$$

, where law of mass action gives:

$$\frac{p^2}{[V_O^{\bullet\bullet}] \cdot (pO_2^{1/2})} = K_{ox}(T) = K_{ox}^0 \cdot e^{-(\Delta H_{ox}/k_B T)} \tag{1.7}$$

The ΔH_{ox} is reduction ethalphy.

It can be shown that the $\Delta H_{red} + \Delta H_{ox} = 2 \cdot E_g$ at T=0K.

T > 1000°C

At high temperatures all elements are considered mobile and can be removed from the lattice. Therefore, all vacancies has to be taken into account by the relation:

$$nil \rightleftharpoons V_S^{''} r + V_T^{'''} i + 3V_O^{\bullet\bullet} \tag{1.8}$$

, where law of mass action gives:

$$[V_S^{''} r] + [V_T^{''''} i] + [V_O^{\bullet\bullet}]^3 = K_S(T) = K_S^0 \cdot e^{-(\Delta H_S / k_B T)} \tag{1.9}$$

The ΔH_S is the reaction entalphy.

The acceptor doping

Most preferably all dopants (and impurities) that are red-ox active should be taken into the calculations, however in many cases the exact concentration of impurities is not known. The character of the doping depends on the relation between the dopant and the host ion charge. If the charge of dopant (or impurity) is less than the host cation they act as acceptor, while in reverse case they act as donor. The STO structure can accommodate a large variety of elements, with two fundamental mechanism for the charge compensation: acceptors are compensated by formation of oxygen vacancies, while the donors are compensated by cation vacancies. The difference in those two mechanism is that the oxygen vacancies are relatively mobile, while the cation vacancies possess very low mobility. Due to this fact perovskites are frequently not equilibrated at moderate temperatures. Therefore, typically to outweigh the significance of impurities it is advisable to dope the STO intentionally. In this work iron was chosen as a dopant. The Fe is widely used acceptor and a typical intrinsic impurity in undoped STO. Additionally it is a common element and exhibits substantial differences in the visible optical spectra for its oxidation states.

From the simple comparison of the radii of the Fe as showed in Table.1.1, one can predict that the iron will substitute titanium with Fe^{3+} or Fe^{4+} oxidation states. Although the Fe^{4+} is rather unusual, its existence was found in many

Ion		Crystal Radius [Å]	Ionic Radius [Å]
Sr^{2+}		1.58	1.44
Ti^{4+}		0.75	0.61
Fe^{3+}	LS	0.69	0.55
	HS	0.79	0.65
Fe^{4+}		0.73	0.59

Table 1.1: Crystal and ionic radii of elements - The overview of Sr (coordination of XII), Ti and Fe (coordination of VI) atomic radii taken from the literature(49).

compounds, for example in barium ferrate(42) or strontium ferrate(43). Furthermore iron can also substitute Sr site with 2+ oxidation state forming $FeTiO_3$ compound(44). However, for small doping concentrations the iron preferentially substitutes Ti site with the mixture of Fe^{3+} / Fe^{4+} oxidation states(45, 46, 47, 48).

While the 4+ substitution will not change the charge in the system, 3+ substitution leads to $Fe^{3+/4+}$ red-ox reaction:

$$Fe_{Ti}^{x} \rightleftharpoons Fe_{Ti}^{'} + h^{\bullet} \tag{1.10}$$

, where law of mass action gives:

$$K_{Fe} = \frac{[Fe_{Ti}^{'}][h^{\bullet}]}{Fe_{Ti}^{x}} \tag{1.11}$$

Adding the conservation conditions, namely the iron mass balance and the charge neutrality one receives:

$$[Fe_{tot}] = [Fe_{Ti}^{'}] + [Fe_{Ti}^{x}] \tag{1.12}$$

and

$$2[V_{O}^{\bullet\bullet}] + [h^{\bullet}] = [Fe_{Ti}^{'}] + [e^{'}] \tag{1.13}$$

Thus, the incorporation of Fe^{3+} is compensated by the oxygen vacancies in a form of:

$$2[V_{O}^{\bullet\bullet}] \approx [Fe_{Ti}^{'}] \tag{1.14}$$

Conductivity in STO

The defect concentration in STO, as well as in many other perovskites, is strongly related to the electrical conductivity, therefore the point defect chemistry results can be measured experimentally. The following discussion will be limited to the intermediate regime of 500°C < T < 1000°C due to two reasons. First, it was shown that the oxygen vacancies are quite mobile even at low temperatures due to the existence of extended defects (details in next section). Second, the influence of the high temperature (T > 1000°C) can lead to the substantial structural changes (details in Chapter 2), which can not be accurately described by the point defect chemistry only.

Thus the total conductivity of the material consist of the electrons, holes and the oxygen vacancies contributions:

$$\sigma_{total} = 2e_0 \cdot \mu_{V_O^{\bullet\bullet}} \cdot [V_O^{\bullet\bullet}] + e_0 \cdot \mu_n \cdot n + e_0 \cdot \mu_p \cdot p \tag{1.15}$$

, where e is a unit of charge and the $\mu_{()}$ represents the respective mobility.

Additionally the movement of the oxygen vacancies is described by the Nernst-Einstein relation for the diffusion:

$$\mu(T) = \frac{z \cdot e_0}{k_B T} \cdot D_0 \cdot e^{-E_A/k_B T} \tag{1.16}$$

, where D_0 is the diffusion constant.

Experimentally the conductivity of the pure and doped STO samples were studied extensively(18). The results from one of the work for the Fe doped STO can be found in the Fig.1.5. After closer examination one can notice three distinctive regions where the total conductivity vs oxygen partial pressure exhibits different slopes. Based on the previously given equations of the point defect chemistry, one can write the electrical neutrality condition:

$$n + 2[V_S^{''} r] + 4[V_T^{''''} i] + [Fe_{Ti}^{'}] = p + 2[V_O^{\bullet\bullet}] \tag{1.17}$$

, which can be simplified for the three regions also presented in Fig.1.6:

- I: the extrinsic region is dominated by the loss of the oxygen to the surrounding atmosphere, which reduces the electrical neutrality condition to:

$$n \approx 2[V_O^{\bullet\bullet}] \tag{1.18}$$

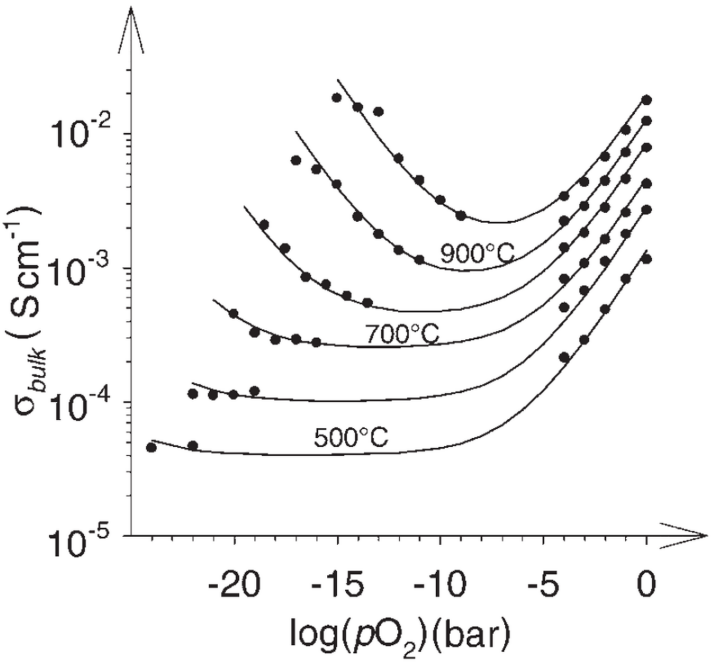

Figure 1.5: Conductivity versus oxygen partial pressure for the Fe doped STO sample. - The experimentally measured relation of the conductivity versus oxygen partial pressure for the 0.1 mol % Fe doped $SrTiO_3$ sample. The n- and p-regions are clearly visible. The data taken from the literature(18).

, where law of mass action gives:

$$n \approx (2K_{red}(T))^{1/3} \cdot (pO_2)^{-1/6} \tag{1.19}$$

giving the slope of $-1/6$ in the $\log(\sigma)$ - $\log(pO_2)$ plot.

- II: the n-type region where the oxygen vacancy concentration is constant and defined only by the acceptor (iron) concentration, which reduces the electrical neutrality condition to:

$$2[V_O^{\bullet\bullet}] \approx [Fe'_{Ti}] \tag{1.20}$$

, where law of mass action gives:

$$n \approx \left(\frac{2K_{red}(T)}{[Fe'_{Ti}]}\right)^{1/2} \cdot (pO_2)^{-1/4} \tag{1.21}$$

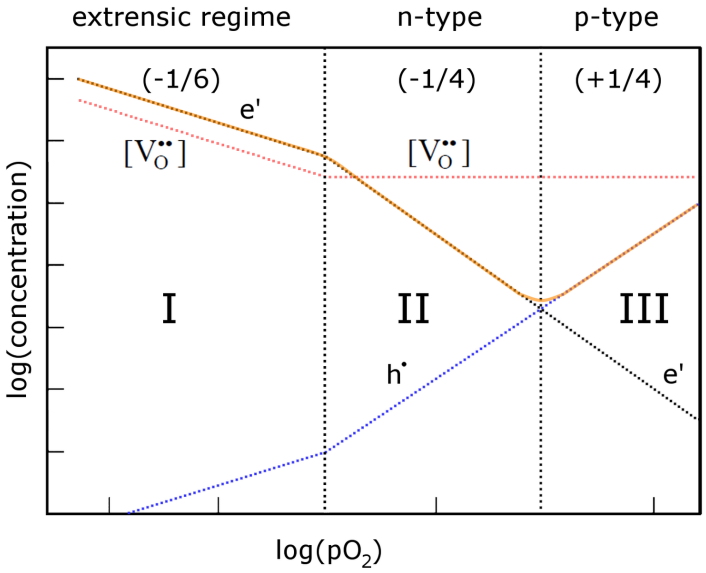

Figure 1.6: Schematic representation of the point defect concentration for acceptor doped STO. - The relation between the defect concentration and the oxygen partial pressure. The three distinctive regions are showed and discussed. The defect concentration connected with the dopant (iron) is constant and thus it is not shown.

giving the slope of $-1/4$ in the $\log(\sigma)$ - $\log(pO_2)$ plot.

- III: the p-type region where the oxygen partial pressure is sufficiently high to oxidize the material and to 'fill' the oxygen vacancies.

  Thus the electrical neutrality condition is similar to the n-type region, but the hole concentration exceeds the vacancy concentration:

$$2[V_O^{\bullet\bullet}] \approx [Fe'_{Ti}] \tag{1.22}$$

  , where law of mass action gives:

$$p \approx \left(\frac{K_{ox}(T) \cdot [Fe'_{Ti}]}{2}\right)^{1/2} \cdot (pO_2)^{+1/4} \tag{1.23}$$

  giving the slope of $+1/4$ in the $\log(\sigma)$ - $\log(pO_2)$ plot.

Even though the defect chemistry can give satisfactory explanation for the observed results, there are limitations (assumptions) given in the beginning of

the chapter, that has to be met. To point some of them: the assumption of low concentration or lack of interaction of point defects, are not always valid. Moreover the point defect chemistry can be used to a systems that are close to thermodynamic equilibrium, which is is not always the case.

1.1.4 Extended defects

Besides the point defects, real crystals consists defects of higher dimensions. Their classification is presented in the Fig.1.7. One has to keep in mind that such extended defects can, and in most cases are, influencing many properties of materials. The changes in local composition, stoichiometry or structure has essential influence on the electronic structure. The extended defects can be classified to one- (lines), two- (planar) or three- (complex) dimensional defects. What is interesting is the fact that the defects tend to organize from lower to higher dimensional defects with increasing defect concentration. Unfortunately, there are few oxides where this process was investigated thoroughly. One example is the TiO_2, which in many aspects, is very similar to the STO. It was shown, that the stoichiometry range where only the point defects exists (in this case oxygen vacancies) is extremely narrow, giving a value of $x < 0.0001(50)$. At higher concentrations the defects start to interact with each other forming the Wadsley defects and shear planes along certain crystallographic directions. With higher defect concentration the structure undergoes transformations to different crystallographic phases like $Ti_{16}O_{31}$ - $Ti_{10}O_{19}$ - Ti_4O_7 (so called Magneli phases Ti_nO_{2n-1}).

Line defects and dislocations

The two basic types of line defects are the linear clusters and dislocations. Due to small sizes, the detection of line defects is a challenging task. Therefore, only methods achieving atomic resolutions, such as TEM or SPM, are able to do so. An example of linear cluster defect can be found $Bi_{0.9}Ca_{0.1}FeO_{3-0.05}$ thin film(40), where separate chains of oxygen vacancies are visible.

The dislocations on the other hand are much more common, and are typically separated into three groups: the edge, screw or dislocation loop. From the atomic point of view the edge dislocation is an extra half of a crystallographic plane inserted into one point of a crystal as shown in Fig.1.9 (point B). On the other hand, the screw dislocation is the result of a shear stress, which ends in

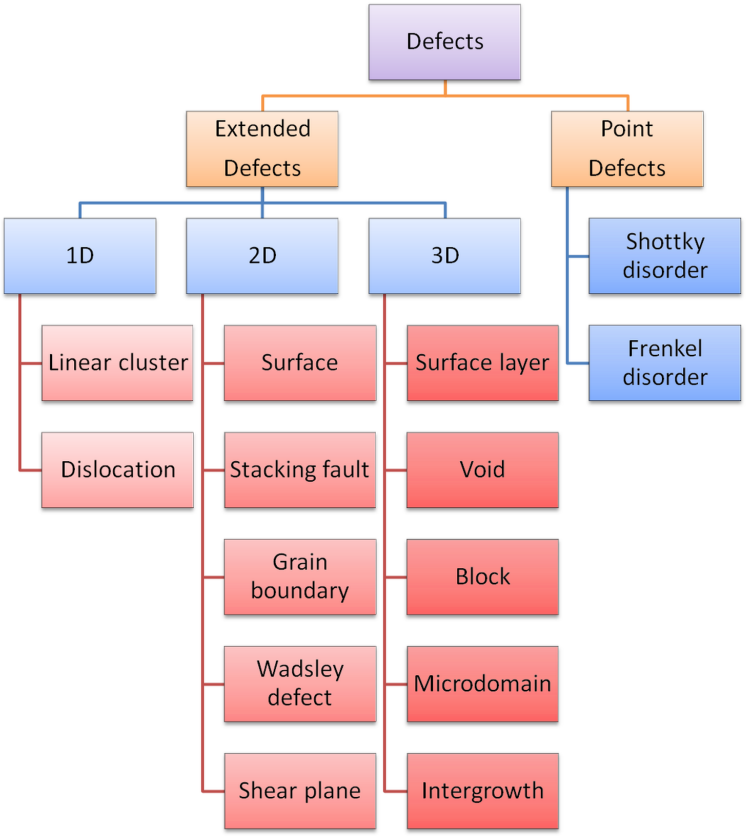

Figure 1.7: Classification of defects. - Classification of defects based on the topological criteria. The point defects are considered zero dimensional(51)

a distortion in a form of a shifted plane - Fig.1.9 (point A). The magnitude of the shift can can vary and is typically equal to one or more cell lengths. In the reality most of the dislocation are of mixed type, such as the one presented in Fig.1.9. The red arrows with the letter 'b' visible in the image are so called Burgers vectors(52). The Burgers vector is a vector that would be necessary to close the circuit formed of base vectors enclosing the axis of dislocation.

The line defects in STO are very important, both from the crystallographic and electronic structure point of view. They introduce very local changes in stoichiometry, which can heavily influence the properties of the material. For example even relatively small oxygen nonstoichiometry (deficiency) can induce the transition from insulator to metal(28). One can use the atomic resolution images from the Transmission Electron Microscopy (TEM) or High Resolution

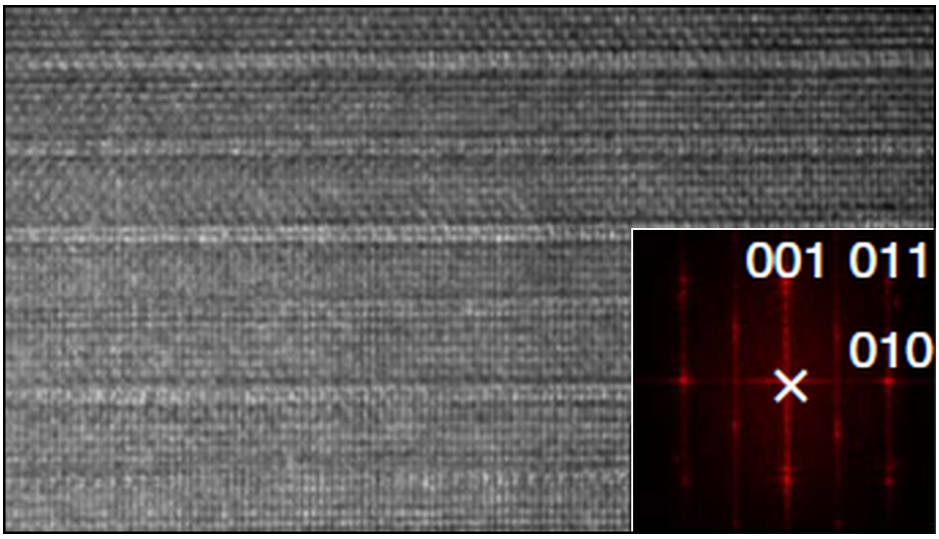

Figure 1.8: TEM characterization of the oxygen vacancy ordering. - Results shows the oxygen vacancy ordering in the Ca-doped $BiFeO_3$ perovskite compound(40).

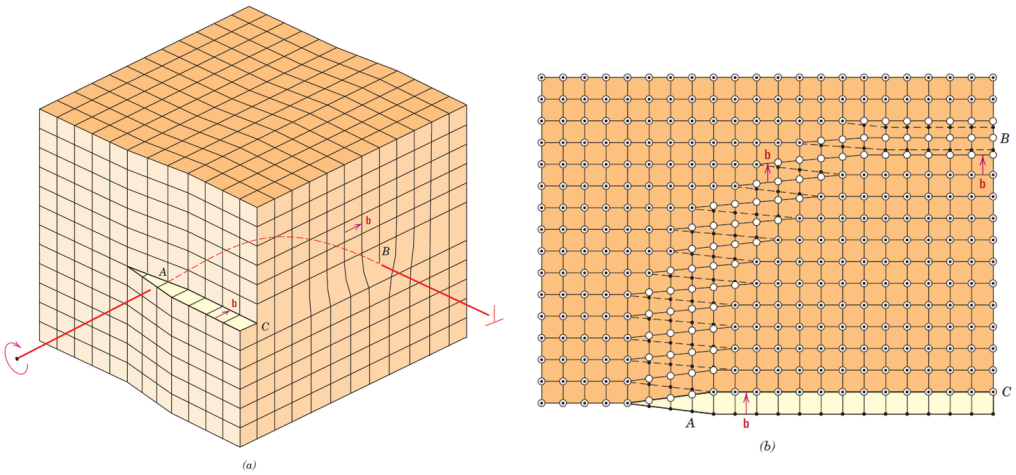

Figure 1.9: Schematic representation of edge and screw dislocations. - At the points A and B the dislocations has one type, screw and edge respectively. The region in between the dislocations is a mixture of those two types(53). Moreover, the open circles represent the atom positions above the slip plane, while the solid circles - atom positions below.

TEM (HRTEM) technique in order to get insight into local stoichiometry of the STO structure. In Fig.1.10 the core of edge dislocations in pure STO crystal is shown(54).

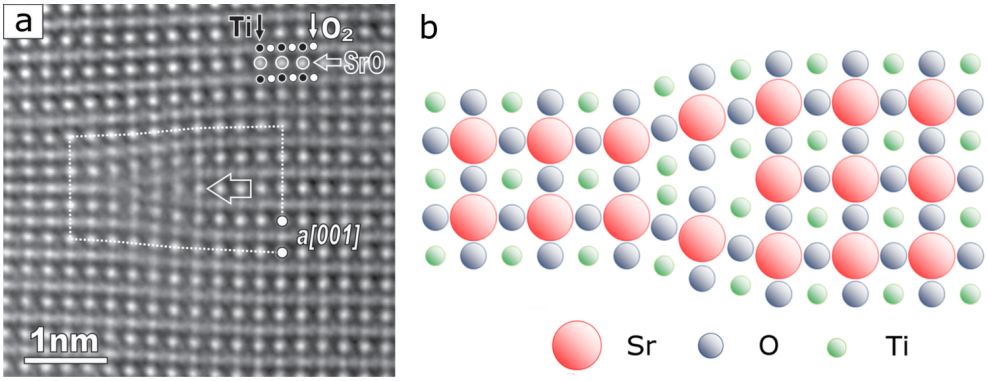

Figure 1.10: HRTEM image of edge dislocation in STO. - a) Image containing a dislocation core in [110] oriented $SrTiO_3$ taken from(54) and b) the schematic representation of a core of dislocation showing an increase in the titanium content in the center.

The TiO_2 and SrO rows are marked with circles. Arrow highlight the splitting of oxygen column. The Burgers circuit yields a Burgers vector of a[001]. The dislocation is formed when extra 'half plane' is inserted into one point in the crystal, in this example an extra TiO_2. There is also other possibility in the STO structure, namely the extra SrO 'half plane' inserted, which will yield an Sr enriched core. This results in a dramatic modification of the electronic structure in the core of dislocation. The change in the electrical behavior of such core can be investigated directly using the local-conductivity mode of the atomic force microscope (LC-AFM). To easily find dislocation exit on the surface, the chemical etching using HCl or $HF+NH_3$ can be used. The higher yield of the cationic exchange reaction on the exit of dislocations will lead to a selective etching, following the relation:

$$SrTiO_3 + HCl \rightarrow H_2TiO_3 + SrCl_2 \rightarrow H_2OTiO_2 \downarrow + SrCl_2 \downarrow \tag{1.24}$$

This leads, in the case of (100) oriented STO, to formation of characteristic inverted pyramids on the surface. Those pyramids can be easily inspected by optical or scanning microscopy, thus giving the possibility to simply count the density of dislocations on the surface. An example of can be found if Fig.1.11,

where two of such inverted pyramids are visible. Another example, shows LC-AFM measurement and a striking increase of the local conductivity in the core of etch pit - Fig.1.12 - obtained after additional thermal treatment in reducing atmosphere of pO_2=10^{-9} mbar, for 30 minutes at 1023 K(6). Such remarkable results can only be possible in the case of significant oxygen deficiency in the dislocation core.

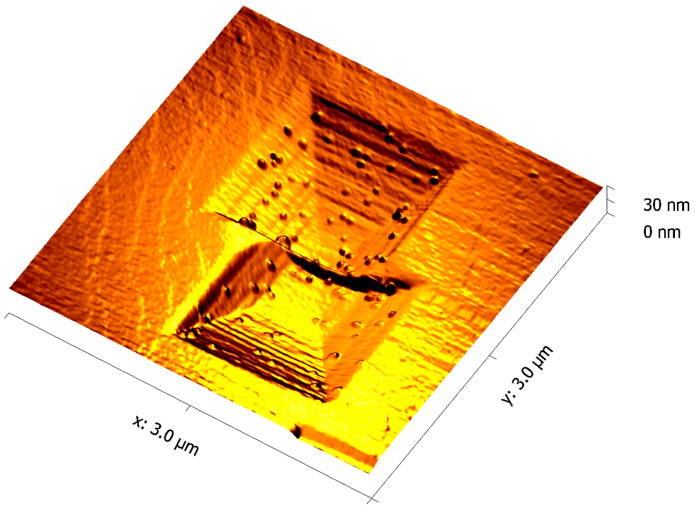

Figure 1.11: The double etch pit on the polished surface of 0.06 % **Fe doped STO.** - The etch pits obtained after short HCl treatment on the surface of 0.06 % Fe doped $SrTiO_3$ and measured using AFM.

The amount of oxygen necessary for the insulator-metal transition calculated from the Mott criterion(52) is approximately in the range of 10^{18} ions/cm^2, however the macroscopic investigation of oxygen removed during reduction gave values four order of magnitude lower. This leads to a conclusion that the thermal treatment removes the oxygen selectively and only small (nanometer sized) regions undergoes insulator-metal transition. This is represented by the fact, that only a small center of dislocation, approximately several nm in diameter, exhibits metallic conductivity. The selectivity of this process is additionally confirmed by other, related physical process - the pipe diffusion. Since the structure around dislocation is disturbed as compared to ideal crystal, the transport of atoms and ions can be enhanced. The pipe diffusion can be investigated by the penetration profiles using ^{18}O exchange profiles and subsequent SIMS investigation. According to Harrison(55) there are three distinctive regimes of preferential diffusion along dislocations - the A-regime which favors a 'bulk' diffusion, C-regime that favors

diffusion trough dislocations and B-regime, which is a mixture of the previous two. Since all of them have characteristic depth profiles, by the ^{18}O tracer depth profiling it can be distinguished what kind of diffusion is favorable in $SrTiO_3$ crystals. In order to do that one has solve the diffusion equation in a form:

$$\frac{\partial}{\partial t}c(x,t) = D\nabla^2 c(x,t) \tag{1.25}$$

The diffusion process in the volume can be given by the Gaussian complementary error function in a form:

$$c(x,t) = erfc\left(\frac{x}{2\sqrt{D_b T}}\right) \tag{1.26}$$

, where the $\sqrt{D_b t}$ is the diffusion depth defined as the square root from bulk diffusion constant D_b times time t. The complementary error function is defined as:

$$erfc(x) = \frac{2}{\sqrt{\pi}}\int_x^\infty e^{-u^2}du \tag{1.27}$$

Next, by following the work of Claire(56) one can obtain a relation:

$$D_d\delta = 0.66\sqrt{\frac{4D_b}{t}}\left[-\frac{\partial \log c}{\partial d^{6/5}}\right]^{-5/3} \tag{1.28}$$

, where the δ is the width of easy diffusion path and D_d is the dislocation diffusion constant. Thus by plotting the experimentally measured ^{18}O tracer diffusion profiles versus $d^{6/5}$ on should be able to receive linear fit for the special case of pipe diffusion. The experimental data(28) yielded not only the profiles very typical to the C-regime, but also characteristic to the diffusion along dislocation network. The idea of dislocation network is also supported by the LC-AFM measurements. In LC-AFM method the voltage is applied in between the conducting tip and the bottom electrode, which is the sample base. Therefore, if one detects current flowing, the electrically conducting path trough sample has to exist. If one takes into an account the fact, that the average thickness of a single crystal sample is approximately 0.5 mm, it is reasonable to assume that the complex network of dislocations exist, rather than one single long dislocation. Moreover, the dislocations are rather common in crystals with high growth ratio such as STO crystals, which is confirmed by the etch pits and TEM investigation, giving values of $10^9/cm^2$(57). Since the density of defects is higher close to the surface,

as compared to the crystal interior, by the factor of 1.5, thus an tree-like (higher density on surface, lower in the bulk) network of dislocation is most likely to exist.

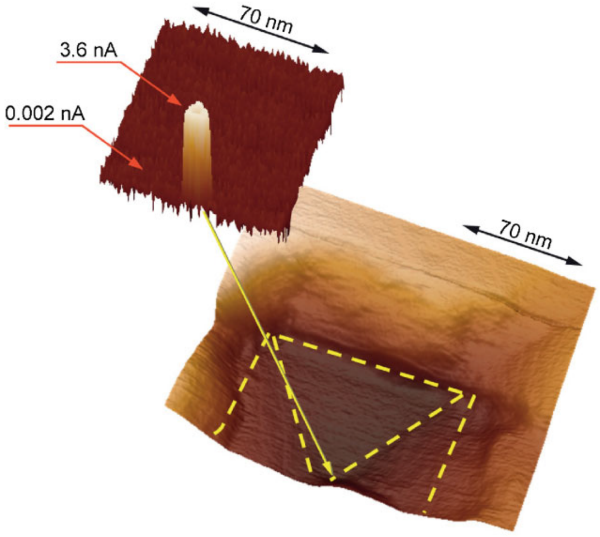

Figure 1.12: Dislocation core measured by LC-AFM in STO. - The enhanced local conductivity found in the core of the dislocation found in the $SrTiO_3$ crystal after chemical etching and annealing in high temperature (1023 K) at reducing atmosphere (pO_2=10^{-9})(6).

Stacking faults

Stacking faults are related to the sequence, at which the planes of the structure in the crystallographic lattice are aligned. They occur commonly in layer structured materials such as the ABO_3. The ABO_3 structure, or STO structure in particular, can be understood as a stack of alternating layers of AB and BO_2 crystallographic planes (in (100) direction), thus the perfectly ordered structure exhibits a $AOBO_2AOBO2$... sequence. Any distortion of this sequence, for example in a form of $AOBO_2BO_2AOBO_2$, is called a stacking fault. In the case of STO, typical stacking fault will be a double layers of SrO or TiO_2. This leads to a strong modification of the local electronic structure. Stacking faults are commonly linked with other defects such as dislocations, and do not extend over large distances.

Shear planes

Shear planes are formed when a part of the crystal is shifted relatively to the neighboring crystallographic planes. The boundary between the shifted part and the original crystal forms two dimensional defect. Shear planes in the STO structure are typically shifted by half of the unit cell, which lead to a change in the local stoichiometry and the modification of the electronic structure. Moreover a large density of shear planes can lead to formation of block structures with different stoichiometry - so called Wadsley defect. However, there is ongoing discussion if the Wadslay defects are the seeds of a completely different phase.

Grain boundaries

The grain boundaries are formed between different grains present within the polycrystalline solid. Those grains (crystallites) are typically randomly oriented, therefore the boundary between them can have different composition, both choreographically and stoichiometrically. In many cases the grain boundaries are amorphous or contain a large quantity of structural disorder, and therefore have different properties than the solid they are in.

Surface

Another type of an extended defect is the surface itself. It is a natural boundary between the interior (bulk) of the materials and its surrounding, and for that reason alone it is worth investigating. The surface atoms cannot satisfy their bonding requirements in the same way as bulk atoms. The coordination number of Sr and Ti drops, from twelve to eight and from six to five respectively. This leads to a broken bonds on the surface - so called dangling bonds. A high density of dangling bonds contributes to affinity to bond organic and non-organic gas molecules. Those adsorbates (atoms or molecules which are adsorbed on the surface) can be categorized according to the binding energy in the following way:

- physisorbates - the binding energy is dominated by the Van der Wals forces with the binding energy smaller than 0.3 eV,
- chemisorbates - the binding energy is higher than 0.3 eV and the transfer of electrons occurs (chemical bonding).

In many cases the surface of a solid material is unique, and even in comparison to the exact same material can have surprisingly different properties. The real

crystal surface consist a number of defects, such as kinks, steps, vacancies, dislocations, voids, stacking faults and adsorbed atoms or molecules - as presented in the Fig.1.13. In this work only the case of (100) STO surface was investigated, which according the the crystal structure presented in the previous section, can 'end' either by the TiO_2 or SrO layer. The specific 'ending' of the surface is called termination, and it has a great influence on various physical and chemical properties. Various observation confirmed by the literature shows that the under typical conditions, without any specific preparation, the as received STO crystals have a random mixture of both terminations. However one can specifically reach one or other termination, and this is crucial in the case of specific interfaces in the multilayer systems(58).

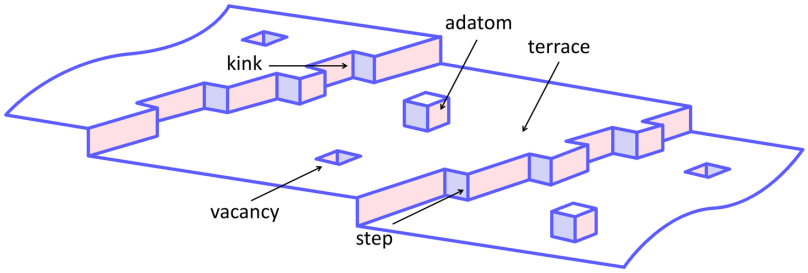

Figure 1.13: Surface specific defects. - The model surface with the most typical surface defects(59).

It is also worth to mention that from the electrostatic point of view both mentioned termination belong to the simplest case of a neutral (type I) surface. There are other types - type II, which is electrically charged but without dipole moment, and type III, which is polar surface(60). In the case of this work no specific termination was chosen. Besides the different terminations there are several phenomena characteristic to the surface: the reconstruction, relaxation and rumpling. The origin for each of the process lays in the minimization of the surface energy(61). The short description of each process is given below and the respective model image is presented in the Fig.1.14:

- relaxation - is a change in the distance in between the atomic layers close to the surface,
- rumpling - is the change of the position of different atomic species that occurs on the surface layer,

- reconstruction - is the change of the atomic structure of the surface, in many cases is influenced by the adsorbates and the history of the sample.

The quantitative values for the atom displacements and rumpling in single crystal STO can be fond in the literature, for example in an excellent work by Heifets and coworkers(62).

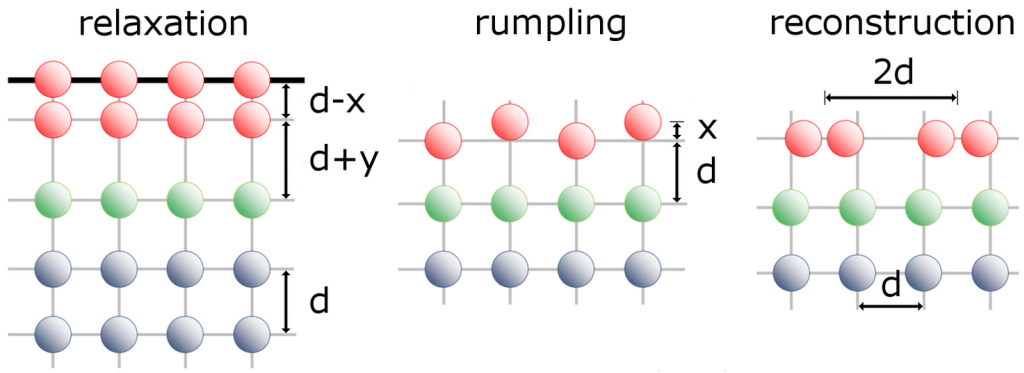

Figure 1.14: Surface distortion phenomena. - The model of three different lattice distortion mechanisms.

One has to also remember that many techniques are surface sensitive, thus the relation between the surface and bulk properties is quite important. Moreover, the surface is the first part of the material, thus should be the first to react on the external stimuli. Therefore the surface properties are often heavily dependent on the production and subsequent preparation of samples. However the external treatment does not affect the surface only, but also acts on the near surface region. Therefore, surface term in this work attributes not only to the top most layer, but also the 'surface layer' that can reach even for several μm into the bulk.

1.1.5 Electronic structure

Many, if not all of, interesting properties of STO can be traced back to its electronic structure. The true understanding of the electronic structure is an area of ongoing research, and in this section some of the most important results will be presented. But first, to qualitatively understand the STO electronic structure a very simple model, based only on the chemical bonding consideration, can be given. In this picture, most of the electronic structure properties can be related to the TiO_6^{-8} octahedron. In the O_h symmetry the Ti 3d state degeneracy is

partially lifted, giving two states: lower t_{2g} (d_{xy}, d_{yz} and d_{zx}) and higher e_g (d_{z^2} and $d_{x^2-y^2}$). Those two states are separated by 2.4 eV and hybridize with the oxygen O 2s and 2p states. In general the 3d states of titanium are unoccupied and forms conduction band, while the valence band is formed of 2s and 2p states of oxygen. The size of the gap, which is equal to 3.2 eV (at 0 K), is large enough to assign the stoichiometric STO as a band insulator. Borrowing the DV Xα cluster method from the literature(51) we can present the schematic of the molecular orbital energy diagram - Fig.1.15.

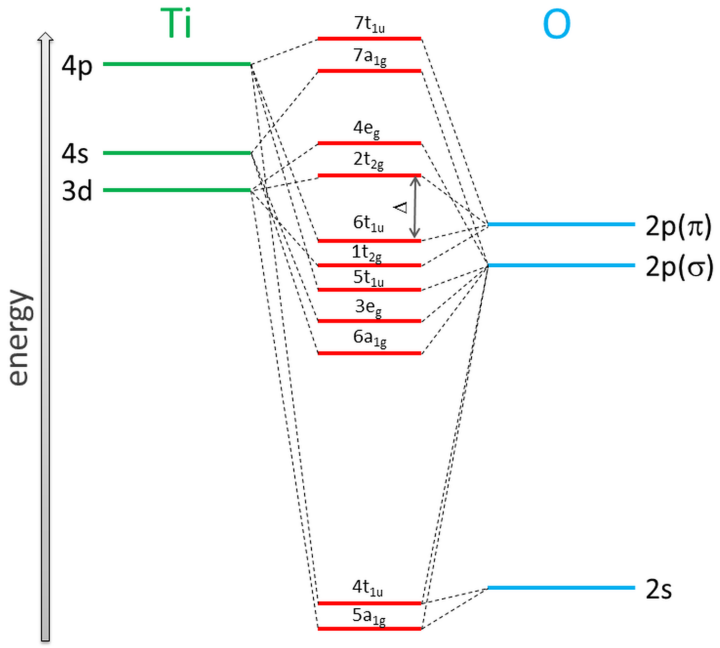

Figure 1.15: Energy levels of TiO_6 octahedral. - The molecular orbital energy diagram of an octahedrally coordinated TiO_6 cluster(51)

Nevertheless, to reliably describe the properties of the STO on has to focus on more sophisticated methods - the first-principle calculations. A large number of work related to the STO electronic structure calculations based on the density functional theory (DFT) can be found(62, 63, 64, 65). Unfortunately many DFT calculations have some difficulties in giving correct values for electronic properties, especially the band gap value. For example the DFT plus additional Couloumb interactions(66) has been successful in calculating the correct bands and gaps energy, but can only be used in correlated and localized electrons systems, such as 3d or 4f in transition and rare-earth oxides. Other approaches were

made, i.e. hybrid functionals like Heyd-Scuseria-Ernzerhof functional(67, 68), which introduce an arbitrary range separation of the exchange energy into a fraction of nonlocal Hartree-Fock exchange potential and either local spin density approximation (LSDA) or generalized gradient approximation (GGA) exchange potentials. The correct values can still be obtained, but the fraction of potentials has to be arbitrary adjusted(69). Other successful hybrid DFT calculations involves CRYSTAL code and the hybrid Hamiltonian in the LCAO basis. The correlation part was done using B3PW exchange correlation functional(70), which included the exchange part as the mixture of Fock 20% and Beckes 80% exchange and corelation part by Perdew and Wang.

One of the most fitting theoretical electronic structure calculations for the pure STO(71) are presented in Fig.1.16. The top image presents the results for the band structure calculations for selected Brillouin directions, while the bottom image show total and projected total density of states. One can notice that the primary contribution to the valence band comes form the oxygen p orbitals. The bottom of conduction bands, on the other hand, is formed primary of Ti 3d orbitals with very small contribution from O 2p orbitals. This mixing of Ti 3d and O 2p orbitals shows a weak covalency of the chemical bonds between Ti and O. The Sr contributes only to the conduction band in the higher energies and has no influence on the states close to the Fermi energy. While the stoichiometric STO is insulating, various defects can modify its electronic properties. Among others, the oxygen vacancies are playing crucial role, not only in STO but in many other transition metal oxides. Since each oxygen vacancy is a source of two electrons, the electron concentration can be adjusted by changing the oxygen vacancy concentration. It can be done either by the red-ox process or by applying electric field. The STO phase however, is very susceptible to the oxygen deficiency, and the phase stability is well below 0.1 % *at* for point defects(72) (even at elevated temperatures). Above 0.1 % *at* point defects starts to interact, which leads to formation of extended defects. What is most interesting, is the influence of such defects on the electronic structure. For example, in the case of oxygen vacancies even very small local oxygen nonstoichiometry in the range of 10^{14} oxygen ions/cm^3 is sufficient to induce an insulator-metal transition(28). Similar effect can be achieved by introducing dopants, both acceptors and donors.

Surface electronic structure

The surface can have different properties than the bulk of a material. The

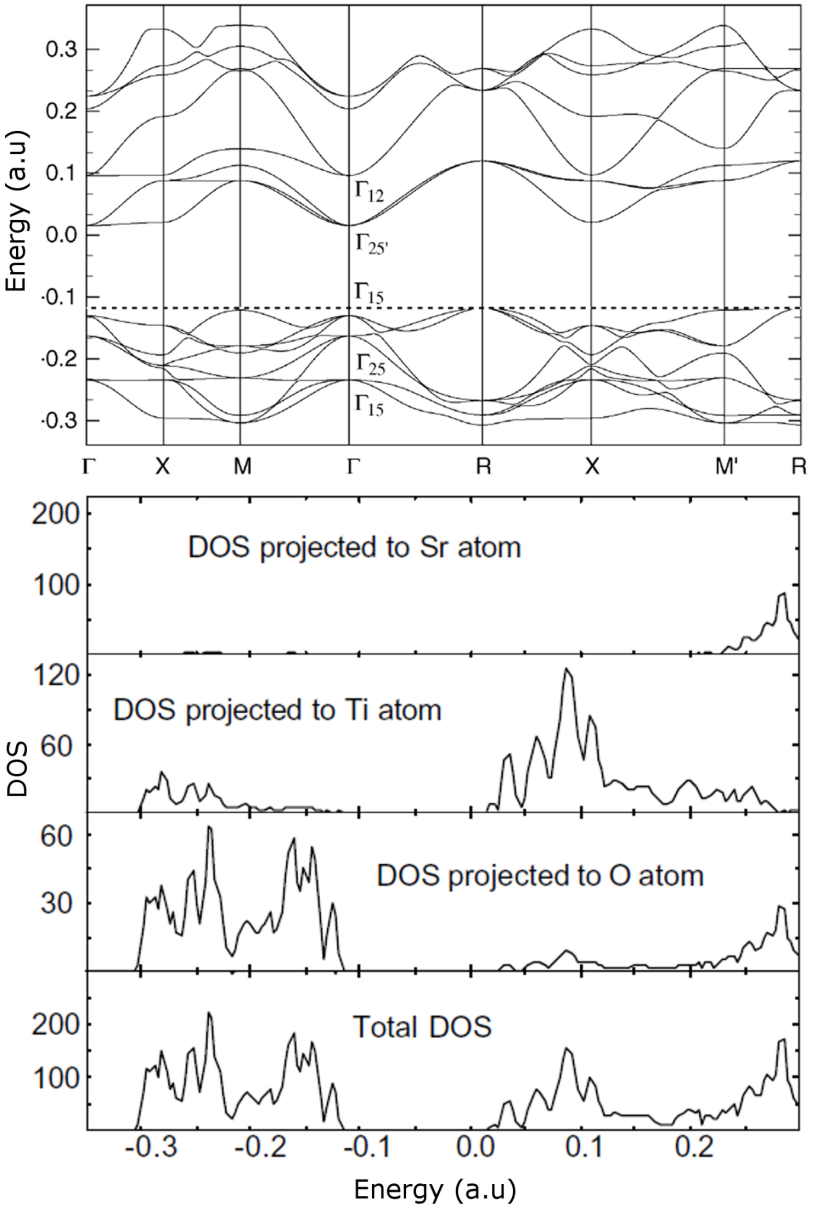

Figure 1.16: Electronic structure of pure STO. - The band structure for specific Brillouin zone directions (top), and the total and projected density of states (DOS) (bottom) for the STO perovskite(71).

breaking of a symmetry can have a substantial influence on many properties, including the electronic structure. One example of such modification is the appearance of the surface states in the band gap(73). In the case of the (100) STO surface, two basic terminations are possible, thus two electronic structures are observed. The results from the density functional theory with hybrid B3PW exchange-correlation functional and electron correlation corrections calculated for the differently terminated STO slabs (7 layers each)(74) are presented in the Fig.1.17.

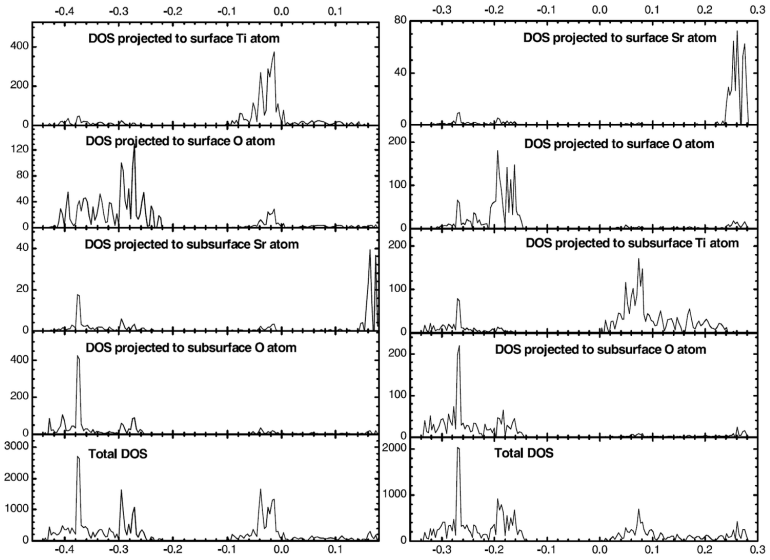

Figure 1.17: DOS for TiO_2 and SrO - terminated surfaces. - The calculated density of states (DOS) for $SrTiO_3$ two terminations in the (100) direction: the TiO_2 termination (left) and SrO termination (right)(74)

The calculations shows band gap reduction for the terminations, especially in the case of TiO_2. There is also an increase of the Ti-O bond covalency close to the surface, which will be discussed further in this work. Moreover the DOS fine structure differ from the structure of the bulk, which can be explained by the differences in the atoms position on the surface (relaxation and reconstruction effects).

Influence of the oxygen vacancies

The oxygen vacancies have a substantial influence on the electrical behavior of STO(75). It is remarkable that the reduction of STO transforms transparent and

insulating single crystals into very dark colored conducting one. The numerical investigations of the oxygen vacancy in STO shows small changes in the bands shape and large changes in the band position - the titanium band is shifted to higher energies. In the other words, the 3d states of Ti ions becomes delocalized, leading to the I-M transition. This effect is more pronounced in the vicinity of the extended defects, such as the columns or rows of oxygen vacancies. The extended defects were directly observed both in pure(76) and doped(40) STO. The electronic structure of an extended defect can be simulated with the use of *ab-initio* calculations. The result for the stoichiometric and reduced STO defect is presented in the Fig.1.18. The image shows the influence of the red-ox process on the extended defect electronic structure of the dislocation core. The calculations shows the insulator-metal transition from the stoichiometric (no oxygen vacancy) and reduced (oxygen vacancy present) cases(6). Since the oxygen concentration can be controlled by external oxygen pressure as well as by the external electric field, the electronic structure along extended defects can be selectively modified. This type of enhancement was experimentally measured with the use of LC-AFM, and will be discussed in the following section.

Influence of the iron doping

The doping typically serves an important role in the semiconductor industry. This interest covers a variety of properties (electronic, magnetic and electric) and various doping. In particular the Fe-doped STO attracted attention recently(77, 78) and naturally, the electronic structure was also investigated(79, 80).

The similar ionic size of Fe and Ti suggest that the iron will most likely substitute on the titanium site. One can find in the literature, that the solid solution of $SrFe_xTi_{1-x}O_3$ exists. Complete substitution of the titanium by iron leads to a $SrFeO_3$ compound, which crystallizes in the same structure as STO, but with different electrical properties as it shows metallic conductivity(81). It was found, that the metallic behavior most likely originates from the existence of $3d^5\underline{L}$ states, in contrast to expected $3d^4$ states. The $3d^5\underline{L}$ states largely contributes into ground states leading to the presence of itinerant electrons. There is also possibility to iron substituting the Sr sites, leading to the $TiFeO_3$ compound. It crystallizes in the trigonal R3 system and exhibits semiconducting behavior.

Results from the first principle calculations, using hybrid DFT theory with the use of B3PW exchange-correlation functional, are presented in the Fig.1.19.

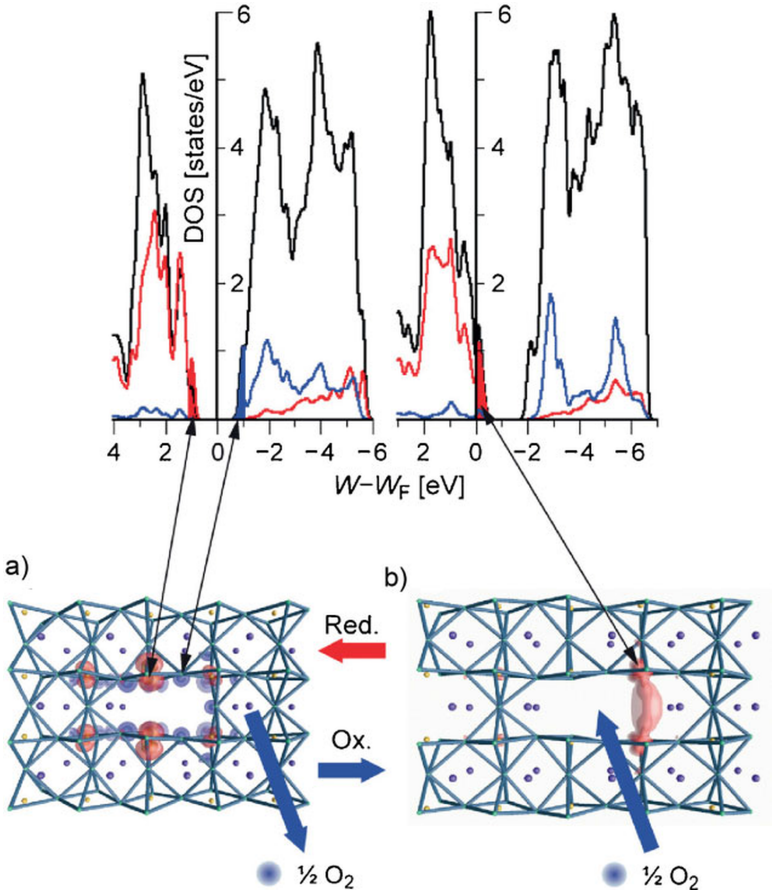

Figure 1.18: Electronic structure of an extended defect in $SrTiO_3$. - Numeric calculation of electronic structure in the case of stoichiometric a) and reduced b) for $SrTiO_3$ single crystal taken from(6).

The band structure and projected density of states for two iron concentrations of 6.25% (left) and 50% (right) are shown(82). Similarly to the case of pure STO, the top of the valence band is mainly formed by O 2p orbitals, while and the bottom of conduction band is formed of Ti 3d states. Additionally, there is a noticeable contribution of iron 3d states in the region close to Fermi energy, originating from the sharp bands of d_{yz} and d_{zx}. As one could expect, this contribution increases with the iron concentration, leading to I-M transition. Experimentally, the decrease of the resistivity with increasing Fe concentration should be observed. Indeed, the formation of additional states in the band gap measured by electron structure sensitive methods such as XPS was already confirmed on the example of thin films(83). What is more, small Jahn-Teller distortion appears, which

was also confirmed experimentally(78). The Jahn-Teller distortion decrease with higher iron concentrations, what can be explained by the changes in the electronic structure (insulating to metallic).

1.2 Resistive Switching

1.2.1 The new type of data memory

The future of the information technology strongly depends on the new ideas and concepts. Those ideas can grow and, in perfect conditions, lead into specific applications. Typically, the computer technology improvement is illustrated by two markers - the microprocessor speed and the size of the computer memory. The former is connected with the number of transistors that can be placed on the micro chip surface, and according to the Moore law, this number should double every eighteen months. Similar law, called the Kryder law, claims that the memory density also has to double every eighteen months. Thus, until the year 2020 the standard 2,5 cal hard drive should have approximately 14 TB capacity. Unfortunately the standard storage technologies are predicted to reach physical limits of miniaturization in the near future. The two most common storage technologies are: the magnetic (HDD) and electrostatic (FLASH) ones. Their most crucial technological limitations are connected with the physical limits and are listed below:

- Magnetic storage memories - the limit of the storage cell size is connected with the superparamagnetic phenomenon. For every magnetic material, there is certain minimum size, below which the thermal energy becomes comparable with the anisotropy energy. This leads to a situation, when the direction of magnetization of memory cell starts to fluctuate. Consequently, it is no longer possible to store information, since there information about initial direction of magnetization is lost.

- Electrostatic storage memories - there are several reasons limiting the memory size, for example the current technology transistor size, which is a below 20 nm. Below that, the leakage currents connected with the tunneling phenomenon start to play significant role. What is more, with the transistor size decrease, the amount of charge needed for writing and reading decreases, which lead to problem with handling such small charges or with the issue of the interference resulting in the unintentional writing of neighboring cells.

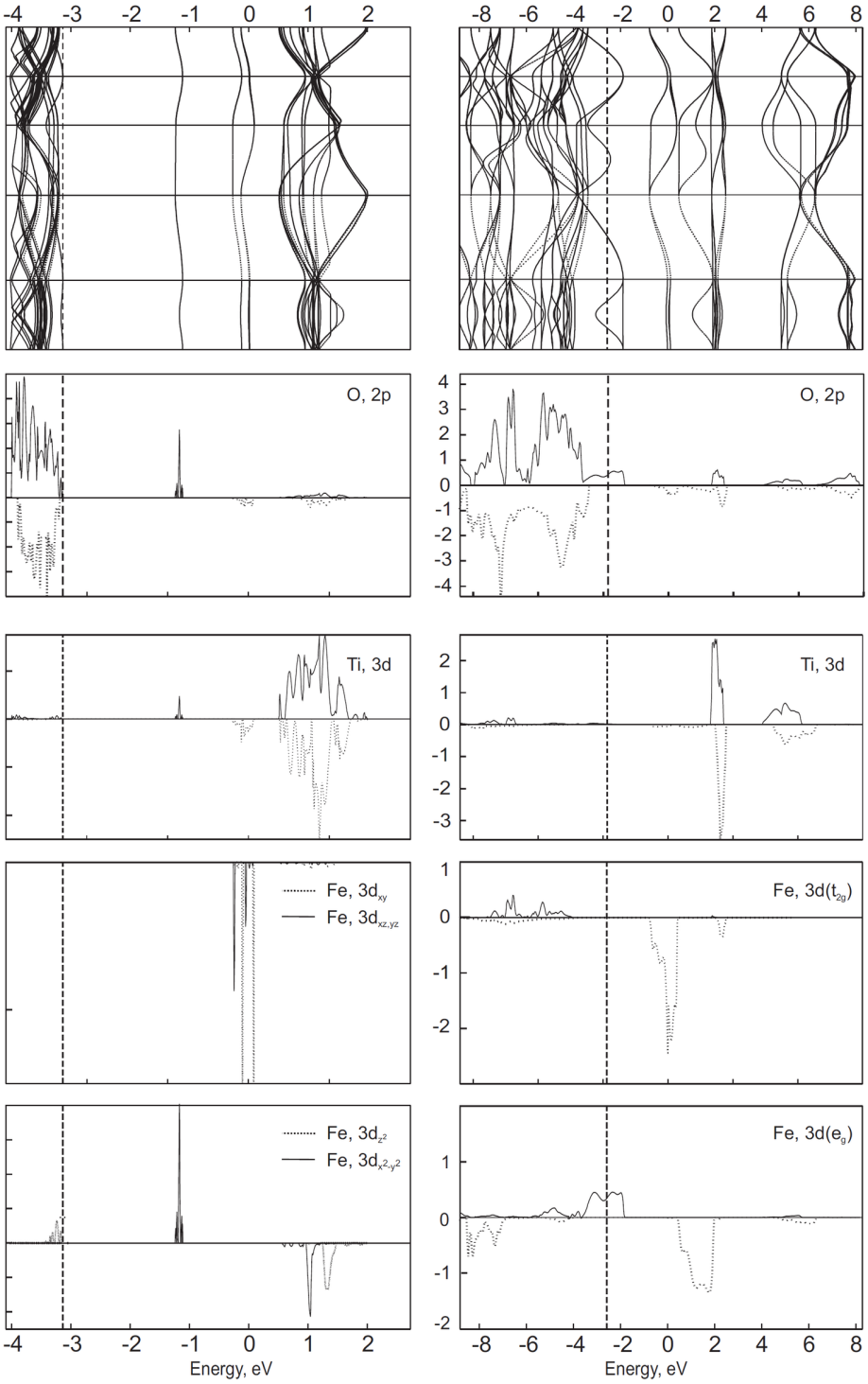

Figure 1.19: Electronic structure of Fe doped STO. - Numeric calculation of the band structure and the projected density of states in the case of two Fe doping concentrations: the 6.25 % (left) and 50.0 % (right)(82).

Since the memory market is enormous (around 74 billion dollars in 2010), there is constant race, both for the improvement standard and the invention of a new types of computer memory. An ideal replacement of the standard non-volatile data memory technology should posses certain advantages in order to be profitable: it should posses high-density, fast write and read speed, low power consumption, high endurance and retention times and finally, low cost(84). Recently a several new concepts of the memory emerged, the Ferroelectric FeRAM(85) and Magnetoresistive MRAM(86), among other. First is based on the ferroelectric effect in metal-ferroelectric-metal capacitors. The writing is realized by utilizing the direction of spontaneous polarization by external electric field. In turn the destructive readout is realized by the displacement current. Second idea is build around the behavior of the tunneling junctions in the presence of magnetic field. The electrical resistivity of such junction depends on the magnetization of two layers, that are separated by the insulating material. By changing the respective magnetization of the layers, one can change the electrical behavior of the junction and the memory function can be realized. The readout is carried out by the electrical measurements. Regrettably, both of this solutions suffers from similar to the standard memory types problems.

To overcome these difficulties, the memories based on the electrically switchable resistance has been proposed. The term of the RS governs all physical phenomena, that can lead to the change of the resistivity between two, or more, distinguishable resistivity levels, under external electric field. The memory based on the RS were called the Resistive Switching Random Access Memory. The writing is realized by applying appropriate voltage pulses, and the reading process uses sufficiently small voltages to prevent accidental writing. The process to transfer the material from high resistance state (OFF) into low resistance state (ON) is called 'set', while the opposite process is called 'reset'. Typically, the concept of RS based device is realized as a capacitor-like structure, where the RS materials is sandwiched between two electrodes. The simplicity of the RRAM construction in comparison to other memory realization is beneficial for achieving high storage densities.

It is worth to mention, that the RS memory cell is connected to the fourth basic circuit element - the memristors(87). This concept emerged from the symmetry consideration between the resistor, inductor, and capacitor first proposed

in 1971. One can form a relations between the voltage v, current i, charge q and the flux ϕ - Fig.1.20.

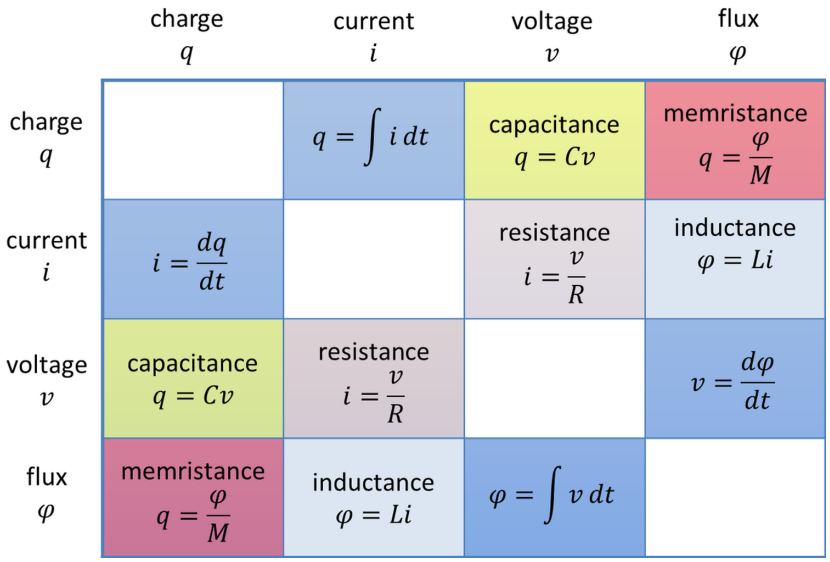

Figure 1.20: Fourth basic circuit element - the memristor. - Basic relations between the voltage, current, charge and flux including all four circuit elements(87). The flux ϕ is described as time integral of voltage v and is connected with the charge q described as time integral of current i. The resistance is naturally the v/i ratio, thus depends on the charged that passed through the memristor.

Thus, the memristance is defined as:

$$v(t) = M(q(t))i(t) \tag{1.29}$$

where

$$M(q) = d\phi(q)/dq \tag{1.30}$$

One can notice, that the memristor can be described as nonlinear resistor with a memory. Thus, the memristor behaves just like standard resistor at a given time, however its resistance depends on its current or voltage history.

1.2.2 Various mechanisms of RS phenomena

The physics behind the RS phenomena is not universal in all cases, and there are several different mechanisms for a material to change its resistivity in a non-volatile way. Although, the RS is driven by the electrical field, the working

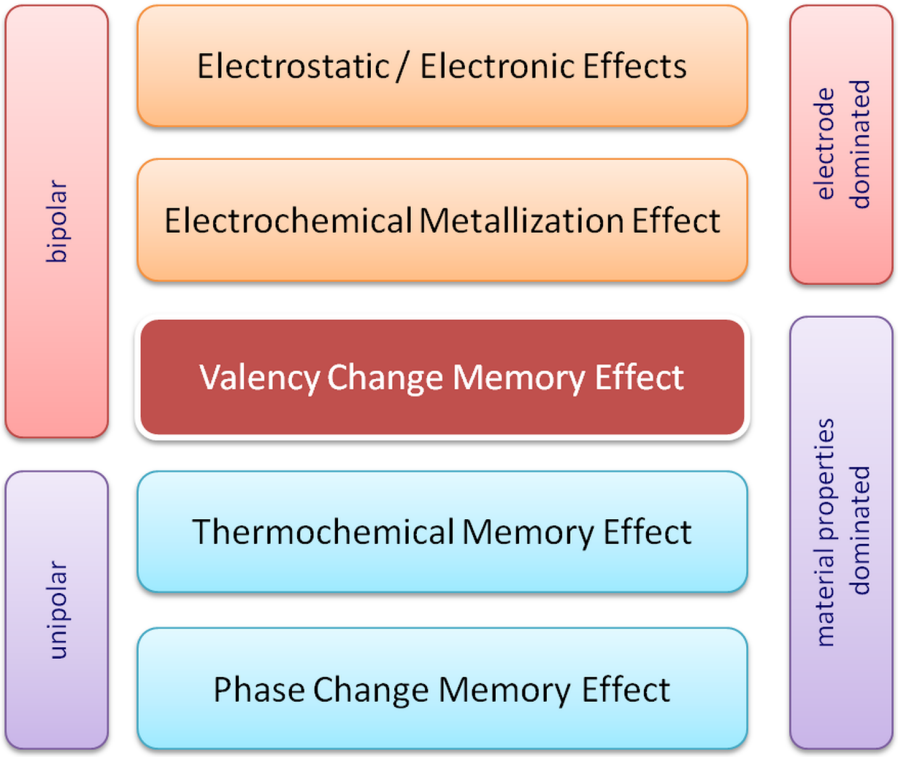

Figure 1.21: Summary for the RS mechanisms. - Classification of most common RS driving mechanisms. The three classes in the center are especially interesting, since those are related with the red-ox chemical effects.

principles can be quite different. In the Fig.1.21 most of RS mechanisms are summarized. This part is concerned only with the three classes in the center of the Fig.1.21, since they are closely correlated to the red-ox in nano scale. In particular the valence change process will be discussed in more detail, as it is considered the main mechanism STO. Moreover, one has to mention that there are two distinctive types of RS as related to the I-V curves - the unipolar and bipolar switching presented in Fig.1.22. The origin of each behavior depends solely on the underlying switching mechanism, thus the short explanation of each mechanism will be given.

The electrochemical metallization

This effect is based on the drift of a highly mobile cations from electrochemically active electrode, trough ion conducting layer. One example of such process can be found in the Ag/Ag-Ge-Se/Pt system, where the active electrode is made of

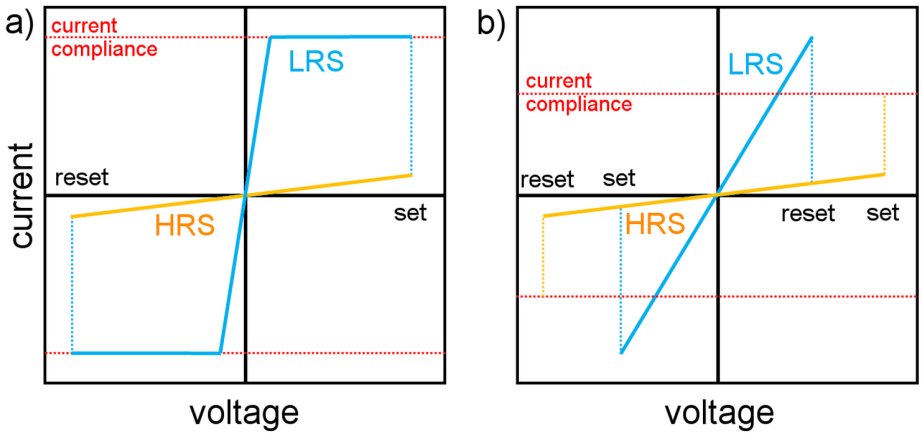

Figure 1.22: Two basic types to of the RS phenomena. - The two types of RS phenomena: a) bipolar switching - there is difference in the polarity, the SET voltage is one polarity of the voltage while the RESET operation requires the the opposite polarity and b) unipolar switching - there is no difference in the polarity, the SET voltage is always higher than the RESET.

Ag, the second one from the Pt and the solid Ge-Se electrolyte in between. The schematic of its memory cell is presented in Fig.1.23 (left) along with the RS model (right)(6, 88). The origin of the RS behavior is the following: at start the material is in OFF state and no Ag is present in the electrolite. Along with the increasing voltage, the SET process starts. With sufficiently high bias, the anode material (Ag) dissolves into the electrolyte, and starts to migrate under electric field to deposit on the cathode. The electrocrystallization process occurs, leading to a formation of metal filaments growing in the preferential direction of the active electrode. In the end, the filaments are long enough to initiate an galvanic contact, which results in dramatic decrease of the resistivity. The material is in the permanent ON state unless an voltage is applied with the opposite direction. If that is the case, the electrochemical dissolution occurs and the material goes into initial OFF state.

The valence change memory effect

This mechanism is most prominent in transition metal oxides and is connected with a migration of anions and corresponding change in the valency. The movement of the oxygen, more often described by by movement of oxygen vacancy, and the red-ox reaction in small scales is crucial for the RS. It is important to

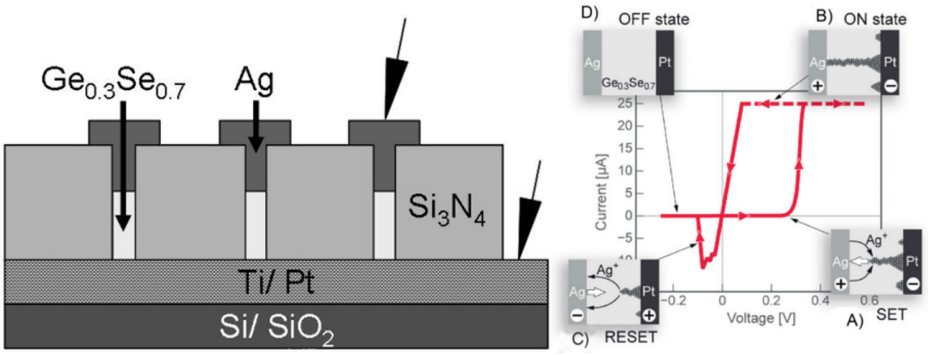

Figure 1.23: Electrochemical metallization memory cell structure. - Schematic of the Ag/Ag-Ge-Se/Pt cell structure (left) and typical current-voltage characteristic (right). Some of the working principle is explained, and the different stages of the switching procedure are shown.

mention that the extended defects plays crucial role for the switching mechanism. We will discuss it in more detail on the example of STO.

The thermochemical memory effect

In this case, the change of the material stoichiometry leads to permanent changes in the resistivity. This is triggered by the local increase of the temperature, due to Joule heating by the electric current. One example of such material is the NiO(10). It was shown, that the RS is caused by the filamentary thermal breakdown of the oxide, leading to formation of well conducting path. One can find an LC-AFM measurements showing the surface of NiO film in the ON and OFF state, along with the model of conducting filaments(89) - Fig.1.24. Additionally the typical macroscopic I-V switching curve(90) can be seen in the same figure. Since the NiO is an unipolar resistive switching material, there is only one polarization presented. The RS in NiO occurs due to changes in the stoichiometry caused by the oxygen migration. In the transition metal oxides the oxygen ions tend to drift out of high temperature regions, because the lower valency state is energetically more favorable at higher temperatures. Consequently, local red-ox process takes place, leading even to structural modification. Moderately high temperatures however, results in a formation of small metallic filaments as seen in Fig.1.24 (left). But one has to remember that during the SET process the current compliance has to be active, to prevent thermal breakdown of the whole cell. On the other hand, during the RESET process, the current compli-

ance is deactivated and the previously formed conductive filaments are thermally destroyed.

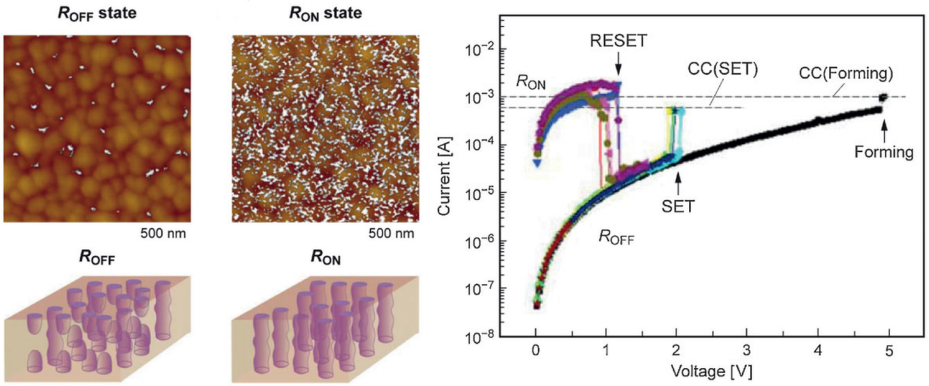

Figure 1.24: Thermochemical memory cell structure. - Schematic of the NiO thin film cell structure is presented; on the left the LC-AFM results for both OFF and ON states(89) and typical switching I-V characteristics(90).

1.2.3 Resistive switching in strontium titanate

In recent years a large attention has been focused on the RS materials connected to the Valency Change Mechanism. In particular, the transition metal oxides gathered a lot of interest, which was related to the oxygen and oxygen defects(6). It was concluded that the defects are crucial to the explanation the RS behavior, and especially the anion defects (oxygen defects), as their concentration is responsible for the valence state of the transition metal cations. This, in many cases, was directly connected to the electronic conductivity and the stable I-M transition.

In this work the focus is put on the doped STO, both in the single crystal and thin film forms. As mentioned earlier, the STO is frequently studied material, has a simple crystal structure(91) and there is extensive literature on its various properties(39, 92, 93, 94, 95, 96). For this reason, this material is regarded as a model material. The current understanding of the switching mechanism in STO is connected with the red-ox process, that is induced by anion migration. The general features, the point and extended defects and their influence on the electronic structure, were already explained in previous sections. On the other hand,

the microscopic explanation of the RS behavior is still a matter of ongoing discussion. According to the literature two major models are proposed: the filamentary and the interface models(11) - Fig.1.25. The filamentary model is based on the concept of conducting filament in the non-conducting matrix, like the fast diffusion paths(12). In this model, the RS behavior originates as a result of a rapture and reformation of conducting filaments under external stimuli. The filamentary switching require electroformation process - the soft electrical breakdown of the material. In some cases the distinctive electroformation step is not necessary, due to the fact that it occurs in the first switching curve and therefore, is not even noticeable. The second model focuses on interface between the RS material and the electrode, frequently pointing to formation of the Schottky barrier at the interface. Consequently, it is the electron trapping that is the explanation of the RS behavior(97, 98).

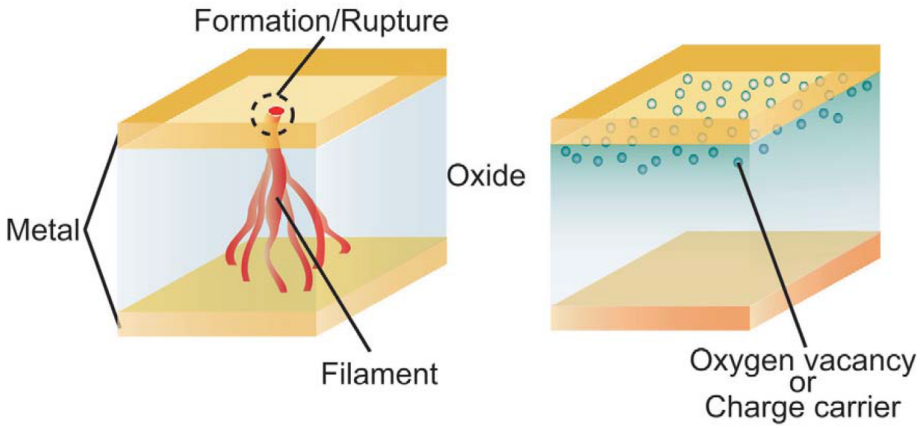

Figure 1.25: Microscopic models for the RS behavior. - Two models proposed for the RS: filamentary conducting (left) and an interface-type (right)(11).

The author of this work strongly believes, that the correct model is in fact the filamentary one, as strong experimental data exist to confirm this scenario both in single crystals(12) and in thin films(99). The second model emerged primarily from the macroscopic investigations, and thus omitted many substantial experimental investigations.

One example of the fact, the basic understanding can be heavily influenced by the nanoscale experimental results, is work done on the TiO_2 crystals. The

microscopic investigations clearly showed not only the existence of the conducting filaments, but also that the filaments are in fact different crystallographic phases(100). Consequently, the understanding of the RS in this material changed from a standard macroscopic approach of $TiO_{2-\delta}$ valency change in the, otherwise homogeneous TiO_2, to a new one, where the RS is explained as the modification of the local chemical composition and formation of new phases(101). Thus, the microscopic investigations, especially by the LC-AFM or TEM techniques, can offer unique information in the nano scale, that can be used to improve or change existing models.

Electroformation

As it was shown in previous section, in many cases the electroformation step in the STO is a necessary for the RS behavior to occur. Thus, the investigations the effect of an applied electric field to a STO sample has to be made. The standard experimental condition for electrical measurements requires attaching an electric contacts, which means that, in fact it is the metal-insulator-metal system that is investigated.

When the voltage is applied to STO sample, the oxygen vacancies starts to migrate. Positively charged oxygen vacancies ($V_O^{\bullet\bullet}$) are attracted to the cathode, while anodic region becomes vacancy depleted(33). In ideal case, the anode block all ionic current, thus the vacancy concentration reaches equilibrium with time. However, in the more realistic case, the anode material does not block the ionic current completely, leading to the oxygen exchange with surrounding atmosphere. The interface between the reduced (high conducting) and oxidized (low conducting) regions is mobile and often called a 'virtual electrode'. One of the earliest examples of the oxygen vacancy migration and the formation of oxygen depleted paths can be found in the spectroscopic study of Cr doped STO(102). In their work a cell formed o 0.2% *at* Cr-doped STO single crystals after electroformation was investigated by the X-ray absorption near-edge spectroscopy (XANES). The Cr pre-edge intensity was used as a marker of the oxygen vacancy concentration - Fig.1.26. Both the oxygen vacancy concentration (left) and Cr valency state (right) could be observed. The results show both previously mentioned effects - the formation of conducting channel reaching from the cathode into the anode, and the increase of the oxygen vacancies represented by the Cr on lower oxidation state in the cathodic region.

In many oxides, during the electroformation experiment, ions do not migrate homogeneously through the crystal, but instead migrate by fast diffusion paths

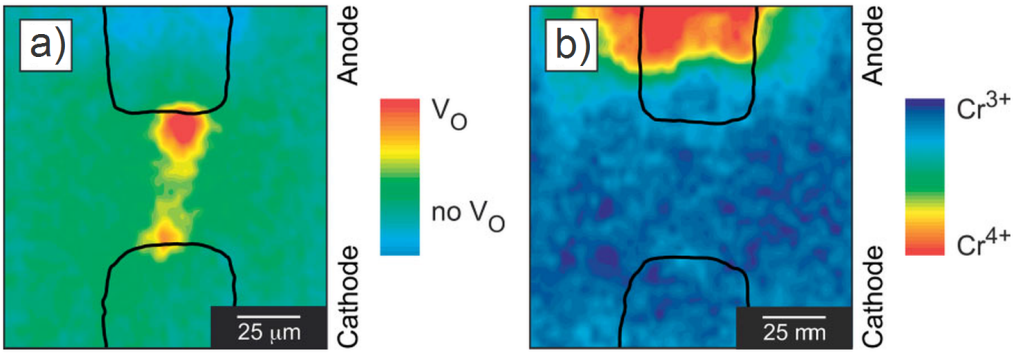

Figure 1.26: Oxygen vacancy concentration and Cr oxidation state maps for Cr-doped STO. - The results of the XANES investigation of Cr K-edge (6004.3 eV) measured on Cr-doped $SrTiO_3$ single-crystal memory cell after electroformation procedure. The false color maps shows analyzed data of: the vacancy concentration distribution (left) and the Cr ions valency state (right) take from(102).

formed of extended defects network. This network can be investigated optically, e.g. in STO crystal after electroformation, one can recognize network formed of differently colored streaks positioned along the crystallographic directions(12). What is more, in iron doped STO, the oxygen vacancy concentration can be observed directly, since different oxidation state of the iron has very distinctive color. Thus, the color front emerges during electroformation experiments, which separates the oxygen rich and poor regions. This border is typically rugged, suggesting that there are regions, where oxygen vacancy migration is faster than the surrounding material - Fig.1.27. The electroformation ends with the virtual cathode reaching the anode region. At that point the electric breakthrough occurs. Even so, the electrical connection is very localized, and can be easily destroyed by applying voltage with the reverse polarity. This is the starting point for the RS behavior, since the weak electrical connection can be established (or destroyed) by the appropriate voltage.

The electroformation process for the Fe-doped STO will be investigated experimentally in the Chapter 4.

RS mechanism

After the electroformation process, the resistivity of the investigated system

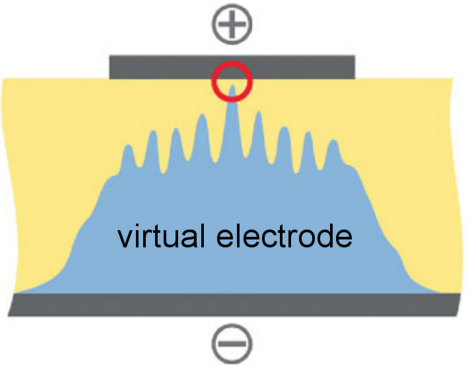

Figure 1.27: Model of the virtual electrode. - The graphical presentation of a 'virtual cathode' formed after the electroformation process in STO.

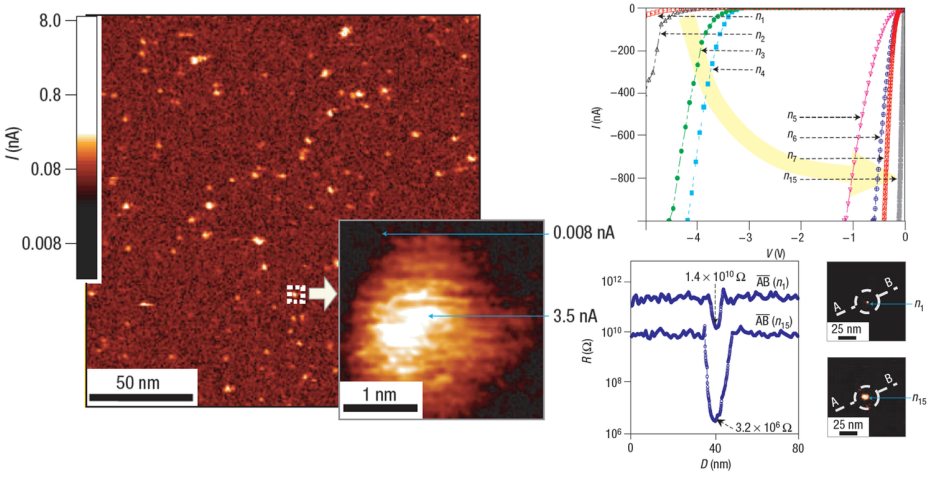

Figure 1.28: Local current map of individual dislocations in undoped STO. - The LC-AFM investigations after thermal reduction and re-oxidation under ambient conditions. Left image shows spots with the sizes of 1-2 nm withing insulating matrix, right bottom - line scan through selected conducting spot and its evolution after negative voltage, right top - I-V characteristics under the voltage sweeps from 5 to 0 V(12).

can be controlled by simply applying the external voltage. The negative voltage pulse will attract the oxygen vacancies toward top electrode lowering the conductivity of the system, while the positive pulse will have the opposite effect. Using the technique with sufficient spatial resolution - LC-AFM(103), it is possible to show, that the RS is limited to very small regions and even a single extended defects (dislocations) can be switched(12). The results from the such experiment performed on reduced and subsequently re-oxidized single crystal STO revealed very localized spots with enhanced conductivity - Fig.1.28 a). Here the electroformation step is shown - one of the conducting spots was chosen and voltage sweeps from -5 to 0 V were applied. As a result, the system transformed from nonlinear (insulating/semiconducting) (from n_1 to n_7) to a metallic behavior (n_{15}). Therefore, after this procedure, the investigated point exhibited stable bipolar switching with characteristic I-V curves showed in Fig.1.29. The microscopic explanation of the phenomena is very similar to the description of the electroformation process given in previous paragraph. The oxygen is pushed along dislocation with the positive voltage and attracted with the negative. However, one has to keep in mind about two aspects: first, that sufficiently high oxygen deficiency along the dislocation must be induced by the electroformation, and second, that the sink and source of oxygen must exist in a form of network of dislocations. One can imagine that the external voltage can act as an electrochemical switch, and the RS phenomena is in fact, related to the region very close to the surface.

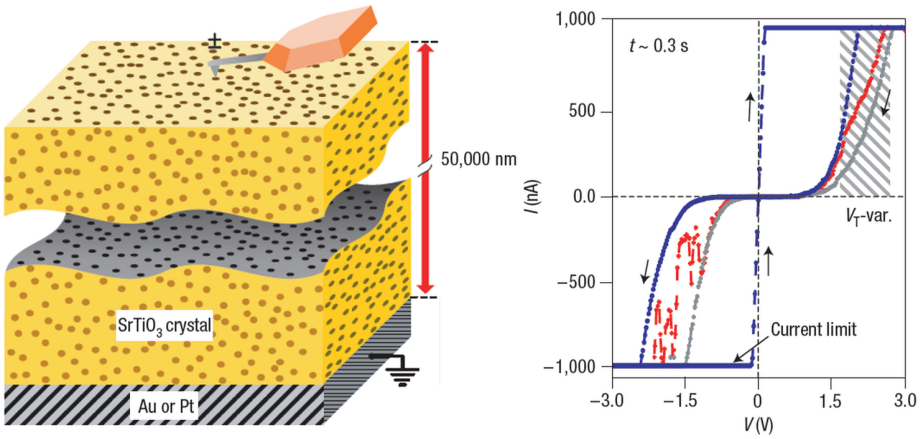

Figure 1.29: Resistance switching of a single dislocation. - a) an illustration of the experimental setup for RS in individual dislocation using LC-AFM and b) the current-voltage characteristics showing bistable resisting switching(12).

1.3 Thesis objectives

The main objective of this thesis is to investigate the behavior of Fe doped STO single crystals and thin films under the electrical and thermal stimuli.

The single crystals are best suited for the basic investigations, thus the crystal structure, dopant distribution, electrical behavior and the RS phenomena are thoroughly analyzed. Many comparisons to the undoped STO are made in order to characterize the Fe doping influence. The results from many different techniques, especially in nanoscale, are shown.

Additionally a chapter devoted to the characterization of Fe doped STO thin films is given. Thin films are more likely suited for the applications, however they are influenced from the substrate side and consequently, have less defined structure. Nevertheless, similar problems such as the structure, dopant distribution and the electrical behavior (RS) are investigated.

I strongly believe that the results shown in this work will broaden the current knowledge on the STO material, and hopefully, will point to interesting experiments in the future.

2

Experimental methods

Currently, due to the large number of experimental techniques and their applications, all scientific work require at least brief discussion about the experimental methods. It becomes even more important when dealing with some specific modification of known techniques. Therefore this chapter is devoted to the brief description and characterization of the involved methods. In order to give clear explanation this chapter is divided into two major parts. First, the explanation of so called 'primary techniques' consisting of the core methods essential to this work will be given. Second, the 'secondary techniques' that were used selectively will be shortly discussed.

The diagram of the experimental techniques can be found in the Fig.2.1.

2.1 Primary characterization techniques

Most of the results presented in this work comes from three basic techniques: the X-ray Phototelectron Spectroscopy, Atomic Force Microscopy and the electrical measurements. The electrical measurements can be further separated into macroscopic by the modified Valdes method, and the microscopic by the Local-Conductivity Atomic Force Microscopy. Sadly, not all of details can be presented here and more information can be found in the included references.

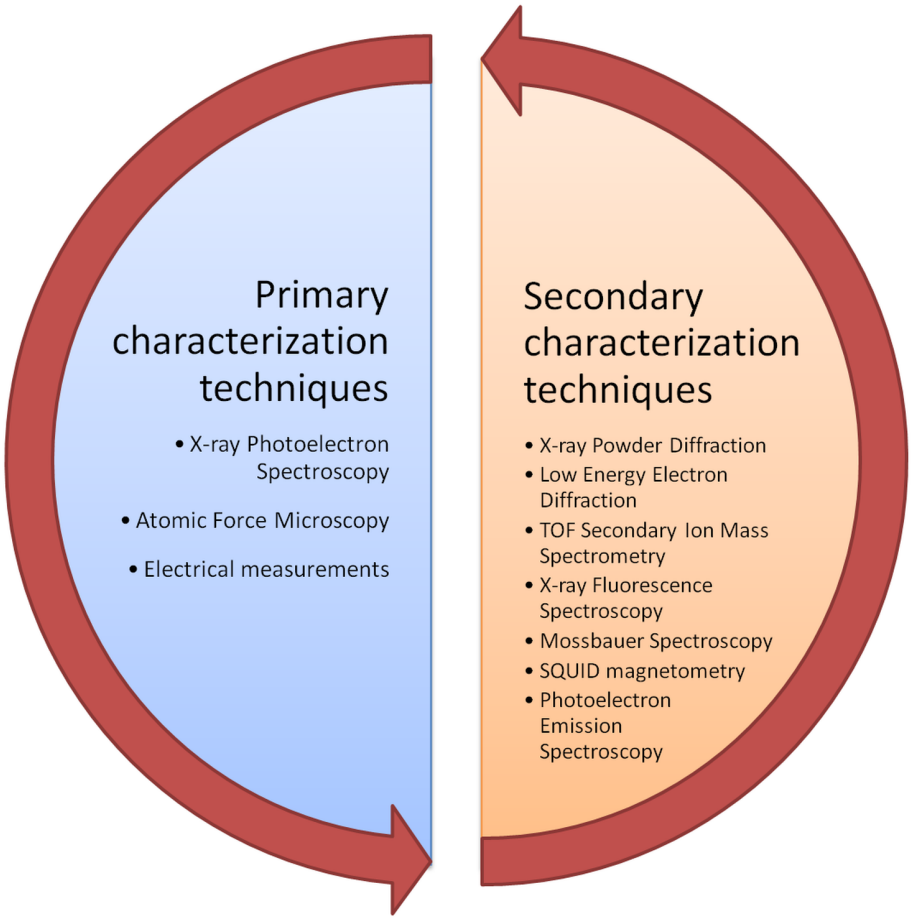

Figure 2.1: Experimental methods. - The diagram of all experimental techniques used in this work.

2.1.1 X-ray Photoelectron Spectroscopy

The X-ray photoelectron spectroscopy (XPS), also called electron spectroscopy for chemical analysis (ESCA), is one of the most widely used techniques for the surface characterization. Their popularity stems primarily from their versatility and the ability to provide a range of information(104).

Standard XPS can provide the qualitative and quantitative information listed below:

- Chemical identification of almost all (except H and He) elements, the minimum concentration limit approximately equal to 0.1 % *at.*

- Elemental environment, such as the oxidation state and covalency of bonds. The XPS spectra can be also used as a finger print of the specific materials, thus allowing also material identification.
- Depth profiles, both in the destructive mode using external sputtering gun, or non-destructive up to 10 nm into the sample surface by angular-dependent XPS studies (or photoelectrons with differing escape depths).
- Lateral surface composition with the spatial resolutions of 2 μm for laboratory instruments. Recent development using sychrotron-based instruments allowed to achieve 15 nm resolution or less.

More sophisticated variations of XPS are capable of providing more detailed information about the chemistry, electronic structure, and morphology of the investigated surfaces.

2.1.1.1 Basic principle

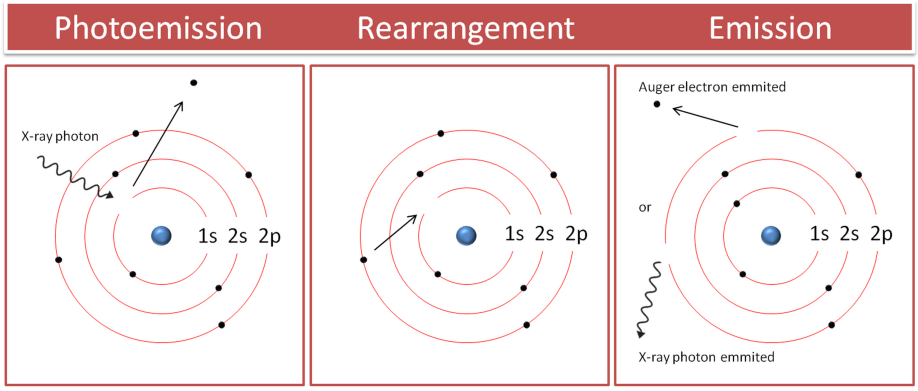

Figure 2.2: XPS basic principle. - Schematic diagram for the photoemission process.

The XPS method requires for the surface of the material to be irradiated with the X-ray photons. Depending on the type of material and the energy of incoming radiation, there is a variety of interactions that can occur. In some cases the photons can pass through without and effect, otherwise the interaction will lead to:

- scattering without energy loss (Thomson scattering),

- scattering with energy loss (Compton scattering),
- absorption of the photon accompanied by the ejection of the electron.

The Thomson scattering, stems from the interaction of the incoming radiation with the electric field of atoms or molecules. Interaction leads to change in the direction of the radiation, which can be used to determine the atomic order, both in large and small scales. The Compton scattering on the other hand, occurs when the energy of the incoming photons is altered, which can be used in determination of the electronic structure. Finally, the absorption of the photon and emission of the electron (photoemission process) can occur. The photoemission process is governed by the set of rules. First, there is no photoemission regardless of the intensity of the photons unless the energy of the photon is greater or equal than the threshold energy (binding energy for the electron), which is characteristic for each element. Once the threshold energy is exceeded, the amount of photoelectrons is proportional to the intensity of the radiation. When the energy of the photons is higher than binding energy, the excess energy is transferred to the emitted electrons, according the Einstein equation:

$$E_B = h\nu - E_k \tag{2.1}$$

, where E_B is the binding energy of the electron in the atom, $h\nu$ is the energy of the X-ray photon, and E_k is the kinetic energy of the photoelectron that can be measured. Consequently, one can obtain the binding energy of the electrons, which in turn is characteristic to the atom itself, as well as the local environment. The photoelectron emission process is schematically illustrated in the Fig.2.2. The electrons originating from atoms that are close enough the surface (10 nm), can escape from the material and be measured by the appropriate detector. Therefore, the XPS technique is surface sensitive.

2.1.1.2 Experimental setup

When the sample surface is irradiated by the X-ray radiation with sufficiently high energy, the core-level photoelectrons are emitted. However, the electrons leaving the material can be absorbed in ambient conditions, therefore the XPS experiments are conducted under the ultra high vacuum (UHV). Apart from that, some of the core XPS components, such as X-ray gun, also require low pressures to function properly. For most applications a base vacuum of 10^{-10} Torr is reasonable. The other requirements for successful XPS measurements are connected

with the state of the investigated surface, especially in the lack of contaminants is important.

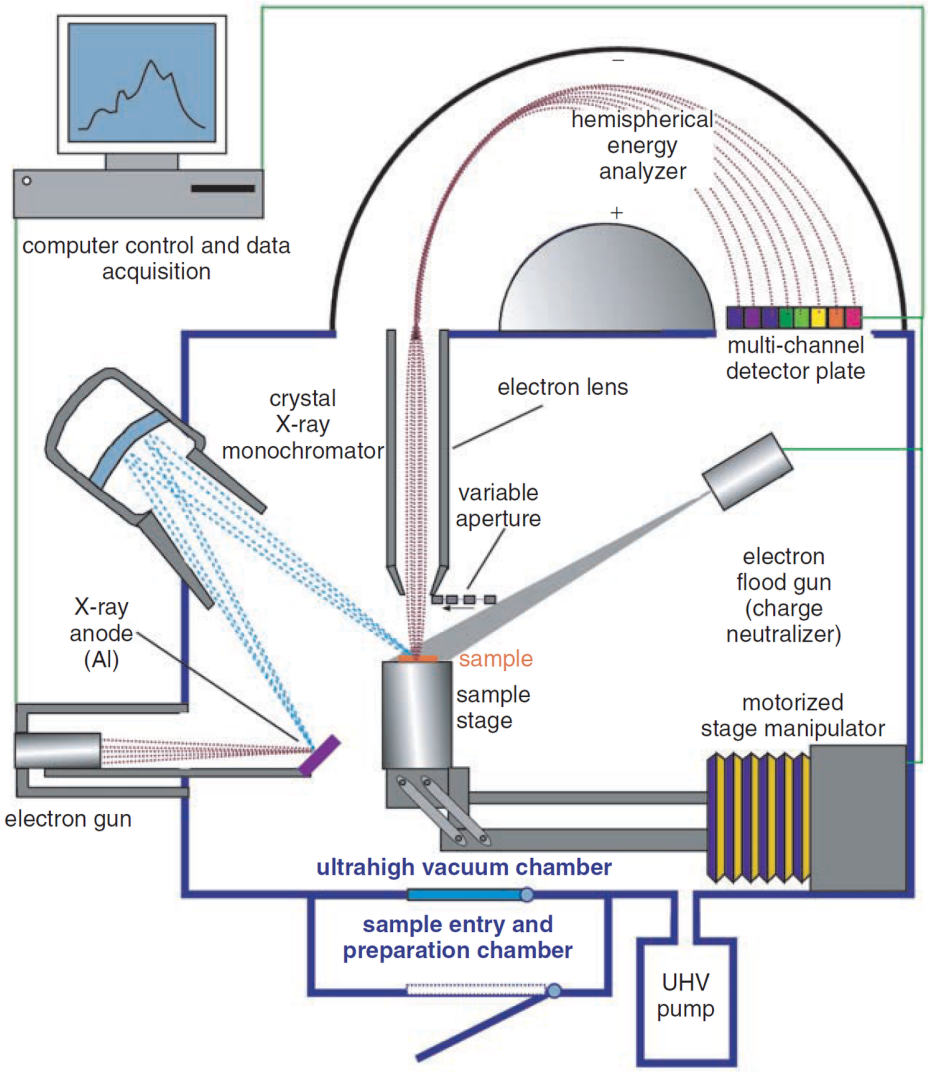

Figure 2.3: XPS experimental setup. - The schematics of modern XPS spectrometer, equipped with monochromatized X-ray source(105).

The typical experimental setup can be found in the Fig.2.3. Beside the X-ray gun (typically with the monochromator), the XPS setup require electron flood gun (which is used for the neutralization of the electron deficient surfaces), an electronic focusing system to gather the photoelectrons and the detector. Most

popular detectors are based on the hemispherical analyzer that is capable of energetic separation; the electrons are first separated according to energy (E_k) and then counted. The E_B values are calculated and typically expressed in electron volts (1 eV = 1.6×10^{-19} J).

2.1.1.3 Data handling

The spectra obtained in the XPS experiment are gathered and analyzed according to two basic regions of interest.

Core levels

Typical core level spectra contains well defined, and relatively sharp, peaks that can be attributed to the various elements that are present in the surface of the investigated material. The area under these peaks is related to the quantity of the respective elements, allowing for the qualitative and quantitative elemental analysis. Additionally, the spectra provides information about the oxidation states, molecular functional groups, etc. There are a number of instrumental and physical factors that has to be included into the calculation in order to achieve quantitative results. Besides the single peaks, the spin-orbit interaction leads to the lifting of the degeneracy and formation of doublets in the p, d or f orbitals. Moreover, more complex peak splittings can be observed, mostly in the transtion metal and rare earth ions (multiplet splitting in p and d orbitals). More details can be found in the literature(106). Also, other features should be taken into account when analyzing the XPS spectra: X-ray satellite peaks (only when non-monochromatized X-ray source is used), shake-up satellites and shake-off satellites, photon induced Auger lines, inelastic scattering background and plasmon loss peaks (in metals). The typical relative error for the XPS analysis is in the order of ± 10 %.

Valence band

In contrast to the core level electrons, the valence band (VB) electrons are directly involved in chemical bond formation and molecular interactions. Therefore, the VB peaks stem from the local environment, which is typically not known. The precise analysis of the VB is possible, however require advanced computer simulation, which is relatively difficult. Instead, qualitative analysis is usually performed. The property that is routinely easily extracted is the band gap value. What is more, for the bonding energies close to 0 eV, the spectra intensity can be

directly related to the density of states, which allows to investigate the electronic structure close to the Fermi level.

2.1.1.4 Summary

Today, the XPS technique is widely available and very practical. The provided versatility and ability to provide a handful of information makes it ideal tool for the scientists around the world. There is an extensive literature in the XPS topic, both in technique and in material characterization. XPS used with the combination of the techniques, such as AFM or LEED, is irreplaceable in understanding many physical and chemical properties of a novel materials.

XPS studies in this work were performed using two different spectrometers: PHI 5600 and 5700 from Physical Electronics, both with monochromatized Al Ka radiation.

2.1.2 Atomic Force Microscopy

The Atomic Force Microscopy (AFM) belongs to a large family of the Scanning Probe Microscopes (SPM)(107). The basic idea behind all SPM is identical: the interaction of the probe with the investigated material, in combination with the scanning motion, can be used to create the 3D image of investigated surface. Those interactions are used to control the feedback system and a piezo-drive, which allows both the scanning motion and the reconstruction of the measured surface properties. Currently there is a number of different SPM techniques that implements various probe-sample interactions, with the two canonical ones: Scanning Tunneling Microscopy and Atomic Force Microscopy(105).

Scanning Tunneling Microscopy (STM)

In the Scanning Tunneling Microscopy (STM), the quantum tunneling current flowing between the conducting tip and the surface is measured. This current is used to drive the feedback loop, which typically maintains constant tip-sample distance. Since the tunneling current depends on the tip position, applied voltage, and the local density of states, the electronic structure of the investigated sample can be measured with atomic resolution. For the relatively uniform electronic properties and the tip-sample distances above 10 Å, the STM can be effectively used to measure the sample topography.

Atomic Force Microscopy (AFM)

The AFM technique has also a variety of modifications, just to mention several of them:

Lateral force microscopy (LFM) LFM measures the lateral deflections of the cantilever that comes from the friction between the tip and the surface. The friction investigation is very useful for imaging inhomogeneity and mechanical properties of the materials.

Force modulation microscopy (FMM) FMM is modification that allows for the characterization of a sample mechanical properties. In this mode the tip is scanned in contact with the sample as for constant-force mode, but in addition, a periodic signal is applied to the tip. This results in the modulation of the amplitude of the cantilever which depends on the elastic properties of the sample.

Electrostatic Force Microscopy (EFM) EFM modes uses additional voltage that is applies between the tip and the sample. The measurement is done in two pass method, first the topography of the surface is acquired, and then tip-sample distance is increased and the movement of the tip mimic the topography. Thus, any additional tip-sample force that not comes from the topography, can be detected. The EFM mode is primarily used to study the spatial variation of surface charge carrier density.

Magnetic force microscopy (MFM) MFM variation is based on the same idea as the EFM mode, yet the magnetic instead of electric interaction is measured. The MFM require a tip coated with a ferromagnetic thin film, thus using the two pass method is necessary.

2.1.2.1 Basic principle

The AFM, first developed by Binnig(108) by combining previously developed STM with the stylus profilometer, uses the detection of the forces between the probe (tip) and the surface. As the forces vary, the reconstruction of the 3D topography of the surface can be made. In this sense the working principle is very similar to old fashioned record-player, where the sharp stylus probed the topography of the rotating record. However, to accurately detect very small forces acting on the probe, and to achieve atomic resolutions, a specially designed probes

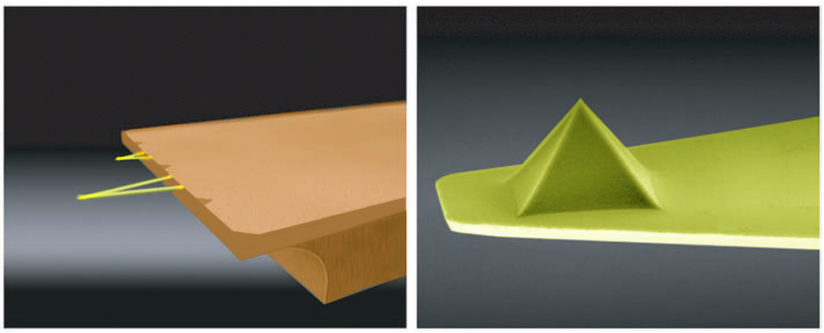

Figure 2.4: Typical probes used with the AFM. - Images of a triangular silicon nitride contact-mode AFM probe (left) and the SEM image of the tip apex for the same probe (right) are presented. Tips manufactured by the NanoWorld AG.

Force	Range (nm)
Electrostatic (Coulomb)	100
van der Waals	10
Covalent or chemical bonding	0.2
Contact	0.1

Table 2.1: Interaction forces in AFM - along with their average ranges of interaction taken from(110).

are required. The typical AFM probe is designed in the following way: the base of the probe is connected to the elastic cantilever, that is placed almost parallel to the surface, which ends with very sharp tip - Fig.2.4. The sharpness and the shape of the tip has a big impact on the quality of the obtained data, thus the sharper the tip, the better is the final resolution. Currently, most manufactures offers tips with the 20 nm curvature, which is sufficient for standard applications (Fig.2.4). However a much sharper tips, with the curvature below 5 nm or 1 nm, are also readily available. Even the carbon nanotube-functionalized tips have been prepared, offering very small tip radii. Thanks to the small dimensions of the tip, standard AFM setup can sense extremely small forces - in the range of 10^{-9} 10^{-6} N, or (in special cases) as low as $3{\cdot}10^{-13}$ N(109). The force experienced by the tip in AFM comes from atomic interactions and have different physical backgrounds. These forces and their ranges are outlined in Table2.1.

A simplified tip-sample calculations can be given using two major contribu-

tions, the attractive van der Waals potential and the repulsive atomic potential. It was shown experimentally, that the repulsive forces grows rapidly while shortening the interatomic distances. On the other hand, for the distances on the order of 3 Åthe repulsive force drops to zero. Such phenomenological potential can be expressed by the following equation, which is called LennardJones potential:

$$w(r) = 4w_0\left[\left(\frac{\sigma}{r}\right)^{12} - \left(\frac{\sigma}{r}\right)^{6}\right] \tag{2.2}$$

or equivalent force, which can be seen in the Fig.2.5:

$$F(r) = -24w_0\left[\frac{\sigma^6}{r^7} - 2\frac{\sigma^{12}}{r^{13}}\right]\hat{r} \tag{2.3}$$

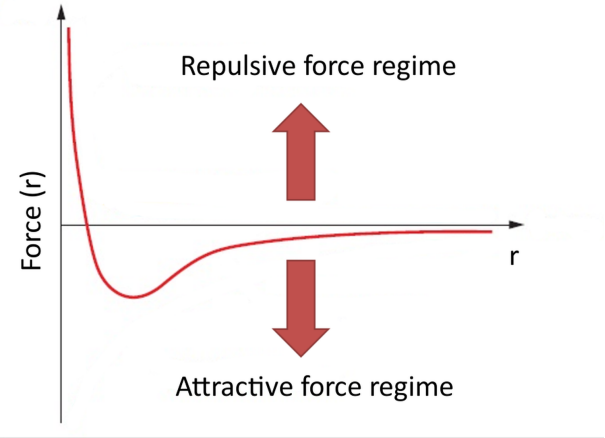

Figure 2.5: Force calculated using Lennard-Jones potential. - Force versus distance calculated for the Lennard-Jones pair potential. Two regions of attractive and repulsive force are clearly visible.

There are two distinctive regions separated by the sign of the force, marked as the repulsive and attractive force regimes - Fig.2.5. This picture is naturally just an approximation, since it was originally developed for a simplified case of two molecules. Nevertheless, this relation can be used to formulate equations for macroscopic bodies, by taking the potential and integrating it over geometry of interest. The approximation for the spherical end of the tip (radius R, density ρ_1), separated by certain distance (z) from the flat surface with density (ρ_2) (Fig.2.6) gives the following equation:

$$F(z) = \frac{\pi^2\rho_1\rho_2 CR}{6}\frac{1}{z^2} \tag{2.4}$$

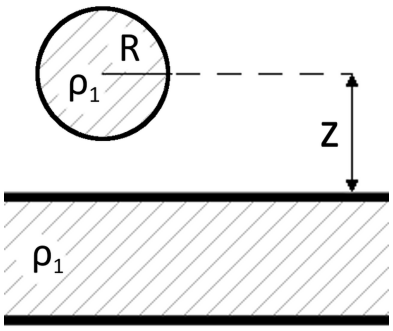

Figure 2.6: Schematics of the tip-sample geometry. - The geometry used with the van der Waals potential for the macroscopic interaction calculation.

Finally, the simplified picture shows that for the small separations (contact) there is mostly the repulsive interaction while for large separations (non-contact) there is mainly attraction. This result is reflected in the existence of the typical AFM working modes:

- contact mode - the tip is in direct physical contact, the feedback loop maintains the constant force,
- tapping mode - the tip is driven to oscillation close to one of its resonant frequency by the piezoelectric drive, since tip oscillates in the vicinity of the surface there is brief 'contact' in each cycle,
- non-contact mode - very similar to tapping mode, the tip is driven to its resonant (or close to it) frequency but there is no contact (repulsive interaction).

Most of the AFM measurements done in this work were performed in the contact mode, the reason for this will be explained along with the description of the LC-AFM technique.

2.1.2.2 Experimental setup

The typical construction of an AFM is presented in the Fig.2.7. The system consist of three major parts:

1. AFM probe (tip) mounted on the piezo-drive for the tip oscillation,

2. piezotube scanner (PZT) - allows to perform the x-y scanning, and z- movement with subatomic precision,

3. force detection system.

The measurement of the force acting on the cantilever is detected and feed to the feedback system. The feedback system is connected with the piezo-tube and keeps the force constant, by changing the z tube position. Thanks to it, the tip-surface distance is maintained (only in the ideal case, since the feedback loop has finite reaction time) and then, from the z position the topography of the surface can be reconstructed. Besides the implementation if the Fig.2.7, there are several other realizations of the AFM setup. For example the piezo scanner can connected the cantilever, instead of the sample, or the piezo tube can be completely removed in favor of the three 'legs' system (Johnny Walker Beetle^{TM}). Moreover the detection system can be realized by different techniques, just to mention some of them:

- tunneling - the detection system for deflection is like the STM, it uses a second tip to monitor the deflection of the cantilever, this method is no longer used today, since it has a variety of limitations (tunneling current is very susceptible to the surface contamination for example), however this is the first method ever used in the AFM system,

- capacitance - the capacitance between cantilever and a reference is measured, which is a linear function of the separation,

- optical interferometry - the interference of the light focused on the tip is measured, allowing to detect the tip-surface separation,

- laser beam deflection - the most commonly used method, where the laser light is reflected from the cantilever into section detector, it has the largest working distance and is insensitive to distance changes.

The laser beam deflection system by the optical lever is the most common approach. The idea implements fundamental parts: the laser diode, a mirror and a split-diode photodetector. The force acting on a tip is measured by the deflection of the cantilever, which is in turn, measured by the laser beam and a photodetector. The detector itself is divided into four sections named A, B, C and D. This allows to measure not only the normal tip deflection (normal force), but also an lateral one (lateral force).

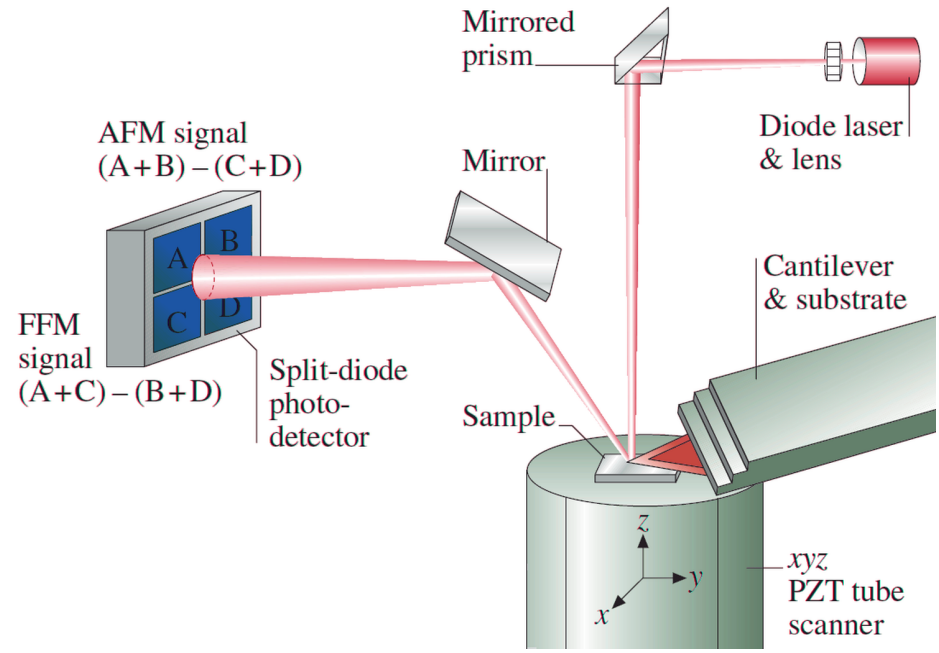

Figure 2.7: AFM experimental setup. - The schematic representation of the AFM setup with the optical lever deflection detection method implemented(111).

The signal for a normal deflection is equal to:

$$F_n = (A + B) - (C + D) \tag{2.5}$$

, while the lateral deflection is:

$$F_l = (A + C) - (B + D) \tag{2.6}$$

To avoid the influence of the noise, the signal measured by the diode is always normalized to the total signal.

The AFM is based upon force measurement, thus there is no need for sample to be electrically conductive. Therefore, samples that are impossible to measure using the scanning tunneling microscope can be routinely investigated, which is perhaps the most important advantage over the STM. In the same time, the AFM resolution comparable to that of an STM. Additionally, the measurement of forces between atoms and molecules can tell us much about their structures and the nature of their interactions.

AFM setup gives the also the possibility to perform experiments under ambient and liquid conditions, however in this work all measurements were done under UHV conditions (10^{-9}-10^{-10} Torr) in order to maintain clean surface. If the thermal treatment was applied it was mentioned along with the results.

2.1.2.3 Summary

Definitively, the AFM technique improved the understanding of various physical and chemical properties of many materials. The AFM is relatively easy to perform, and has little limitations, as compared to other ultra high resolution techniques, such as STM or TEM. Many new improvements, as well as new working modes, are constantly implemented, which widens the experimental possibilities and future applications.

AFM studies in this work were performed using several AFM setups: Jeol JSPM-4610A, Omicron STM/AFM VT-50/500 and smaller Jeol VTJSPM-5200. All of them were equipped with the tips from various manufacturers - Nanosensors, Budget Sensors, Mikromash.

2.2 Electrical Measurements

2.2.1 Modified Valdes method

The electrical resistivity is one of the most important parameters in the materials showing RS behavior. In the STO it is also directly correlated to the density of the oxygen vacancies. The technique used in this work, is based on the well known Valdes method(112). In this method, four electrodes are attached into the flat surface of the investigated material. The electrodes are placed in one line, with equal distances between the electrodes. Current is passed through the outer pair of electrodes and the floating potential is measured across the inner pair. However, in many oxides, the resistivity is not homogeneous across the sample and typical macroscopic measurement gives the averaged information from whole sample. Moreover, the contact between the electrodes and the surface becomes important, as the properties of the material are susceptible type and the method of contact attachment(113). Additionally, the effects connected with the current flow, such as heating and the transfer of matter (ions or vacancies), can substantially change the behavior of the electrodes. Thus a modification of the standard

method is required.

The measurement of the electrical conductivity at different parts of the sample is specially interesting in the case of electroformation or electrocoloration experiments. Thus, a modified Valdes method was proposed, which is schematically shown in the Fig.2.8. The electric potential is measured between each electrode with the help of two electrometers and a amperometer. This gives the opportunity to calculate the potential drop for the most interesting regions of the sample. The regions are:

- the bulk - the measurements is done for the whole sample; the voltage is applied between the outer electrodes and the current is controlled by the current source,
- the electrodes - the measurement is done for the regions close to the outer electrodes, which is very convenient for the anode and cathode analysis,
- the interior - the measurement between the inner electrodes is performed.

This allows for the characterization of the electrical behavior (for example $R(T)$ and RS curves) for the electrodes and the interior of the sample at any point of the experiment. The macroscopic electrical measurements are crucial for the RS materials characterization. Nevertheless, obtained information is always averaged over macroscopic distances. One interested in more local electrical behavior has to turn into microscopic investigations.

The electrical measurements in this work were performed using two Keithley 6524 electrometers, programmable current source Keithley 224 and the Lake Shore 340 temperature controller.

2.2.2 Local conductivity Atomic Force Microscopy

True understanding of the RS phenomenon(12) demands deep insight into local conductivity on the nanoscale. This task can be accomplished only with the help of conducting tip and atomic force microscopy, which together constitute the Local-Conductivity AFM (LC-AFM) technique - Fig.2.9. In this method, the conducting AFM tip is brought into contact with the surface while voltage is applied. By measuring the current flow, both the topography and the local conductivity of

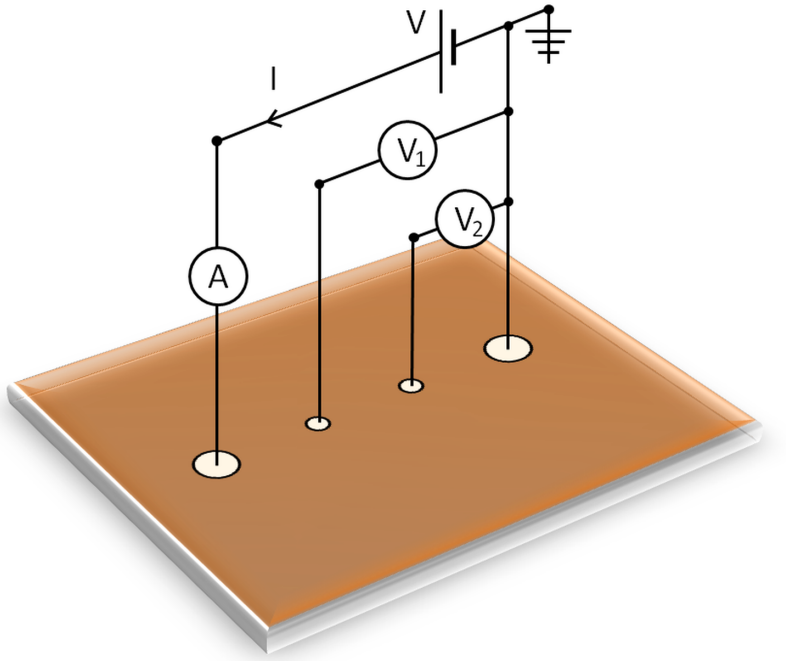

Figure 2.8: Modified Valdes method. - Schematic of modified Valdes method allowing to separate the contribution to the electrical resistivity coming from the electrode region and the interior of the sample.

the surface can be simultaneously obtained. Current value from femto- to micro-amperes have to be measured, which imposes special requirements on the AFM equipment. Since the tip apex is very small (tip apex curvature for the commercially available conducting tips is less than 20 nm), the contact with the surface is no bigger than several tens of nm^2, depending on the force applied. However, the current flow is more localized, which leads to a significantly higher resolution for the local conductivity than the topography. She small contact can lead however, to difficulties; for example even relatively small current will produce high current density in the tip apex. High current density can damage the conducting coating of the tip. Additionally, from the same reason, one has to be very careful with the data interpretation - the current flow is 'bottle necked' into small area of the tip-sample contact. Thus, the tip-sample interface is even more important and the contamination of the surface plays a crucial role(114). Additionally the LC-AFM method utilize two point method, meaning that resistivity of the whole setup (electrical connection, tip-sample force, resistivity of the electronics) is taken into an account. To summarize, the data from the local conductivity can

not be interpreted in the same way as the macroscopic electrical measurement.

Therefore the following section is focused on the thermal stability of tips that were typically used in all experiments involving LC-AFM. It is important to mention, that this part is heavily based on the one of the author articles - The thermal stability of Pt/Ir coated AFM tips for resistive switching measurements(115).

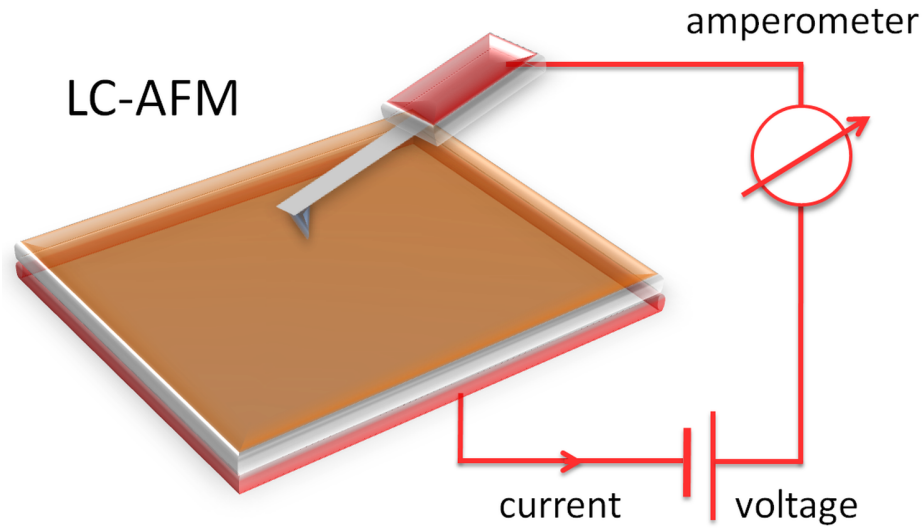

Figure 2.9: LC-AFM experimental setup. - Schematic presentation of LC-AFM technique.

Experimental

As an experiment samples, the silicon tips (PPP-CONTPt, Nanosensors), coated by sputter deposition with a 25 nm thick double layer of chromium and Pt/Ir, with an initial 20 nm tip radius were used. Some of the tips were left without any thermal treatment (reference) and the rest were annealed at various temperatures for 0.5 h: under oxidizing (500 - 700°C air)and reducing (300 - 700°C vacuum 10^{-6} Torr) conditions. The heating and cooling rate was equal to several °C/s on average. The areas of investigation were always on the same side of the probe as the cantilever and the tip. The coating was assumed to be uniform at every point of the probe. The equivalent resistivity per scanning area ($R_{\square}$) was calculated using current maps and statistic functions. The size of the electric tip-sample contact was estimated to be 10 nm $\times$ 10 nm. The data values from several areas (5 or more) in each sample were then averaged.

Thermal stability of Pt-coated conducting AFM tips

The LC-AFM is not the only technique requiring conducting tips, more recently established AFM techniques also make use of such tips, for example: piezoresponse AFM (PMF)(116), scanning Kelvin probe AFM (SKPM)(117) or scanning capacitance microscopy (SCM)(118). Conducting tips are commercially available in a variety of forms ranging from solid metal to, most commonly, silicon with conductive coatings. Since solid metal tips are not very popular due to their low mechanical stability(119) the most popular Pt/Ir coated silicon tips were used in this work. One can ask what is the stability of such tips under various conditions and high temperature. Much work has been done on the mechanical characterization of such tips(120, 121), but there is nearly no information about the behavior of the coating at elevated temperatures. I was especially interested in the topic since the investigation of the local conductivity of nanometer-size filaments or measuring the activation energy requires measurements under both oxidizing and reducing conditions at elevated temperatures thus changes in the properties of the typical conducting tips has huge influence on the obtained results. In order to measure the influence of the various conditions on the conducting tips the following techniques were used: X-ray photoelectron spectroscopy, scanning electron microscopy, transmission electron microscopy and local-conductivity atomic force microscopy. The chemical composition as well as the topography and morphology of the most popular Pt/Ir coated silicon tips were investigated. The influence of thermal treatment on the tip apex was also imaged and the changes in the electrical behavior of the tip coating were observed. Applied temperatures ranges were: 500 - 700°C for oxidizing conditions (air) and 300 - 700°C for reducing conditions (vacuum 10^{-6} Torr), the annealing time was set to 0.5 h. Results yielded the formation of Pt_2Si and SiO_2 on the tip surface. The Pt tends to agglomerate into particles over time, depending on the temperature and conditions. The tip apex radius increases while the electrical conductivity decreases with the temperature. In conclusion, even the lowest applied temperature leads to changes in the tip properties, while these changes are much more pronounced under oxidizing conditions.

Results followed by discussion Fig.2.10 shows the SEM images of Pt/Ir coated silicon cantilevers treated at various temperatures under oxidizing conditions. Fig.2.10 (a) corresponds to an untreated reference tip while Figs.2.10 (b)-(d) correspond to cantilevers annealed at 500, 600 and 700°C for 0.5 h under oxidizing (air) conditions. A comparison between the untreated (reference) tip

and the tips annealed in air shows that the topography and morphology of Pt/Ir coating changes. While for the reference sample the coating is homogeneous and smooth, for higher temperatures hills becomes visible. Similar results (not presented) can be found for cantilevers annealed in vacuum, although the changes are much smaller. TEM measurements were performed in order to look closely into the influence of heat treatment on the tip apex. In Fig.2.11 the reference tip (a) and the tips annealed at 700°C in vacuum (b) and in air (c) are compared.

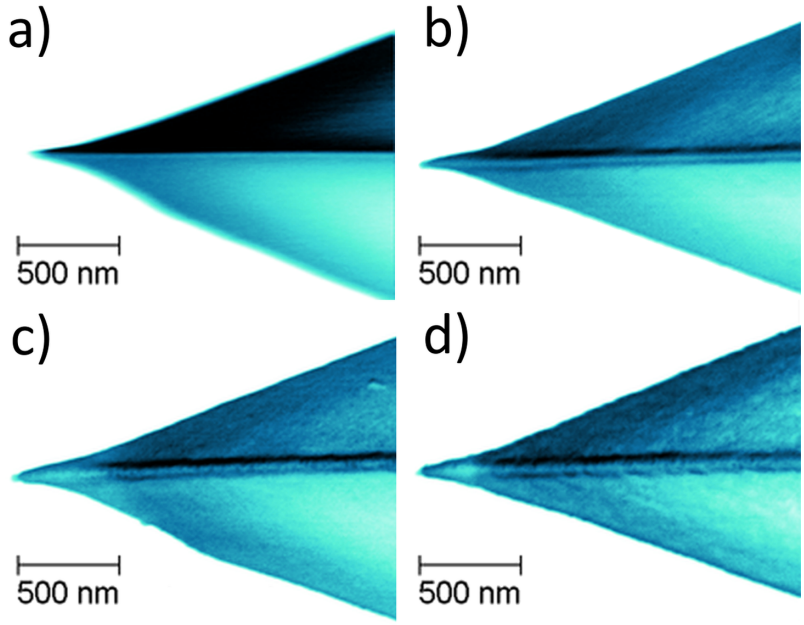

Figure 2.10: SEM images - SEM images of Pt/Ir tips (a) without thermal treatment (b) annealed at 500°C (c) annealed at 600°C (d) annealed at 700°C in air.

The tip apex radius for the reference tip is around 20 nm, the same value as given by the manufacturer and reported from SEM measurements(122). The polycrystalline character of the coating is visible as a grainy structure on the surface of the tip. Much more interesting is the image of the tip annealed at 700°C, which shows the bulk of single-crystalline silicon covered in the center by a thin layer of silicon oxide. On top of this layer several round dark particles can be found with various diameters ranging from several nanometers up to 30 nm. These particles are composed of Pt and a small fraction of Pt_2Si as will be shown in the XPS measurements. The Pt atoms tend to decrease the surface free

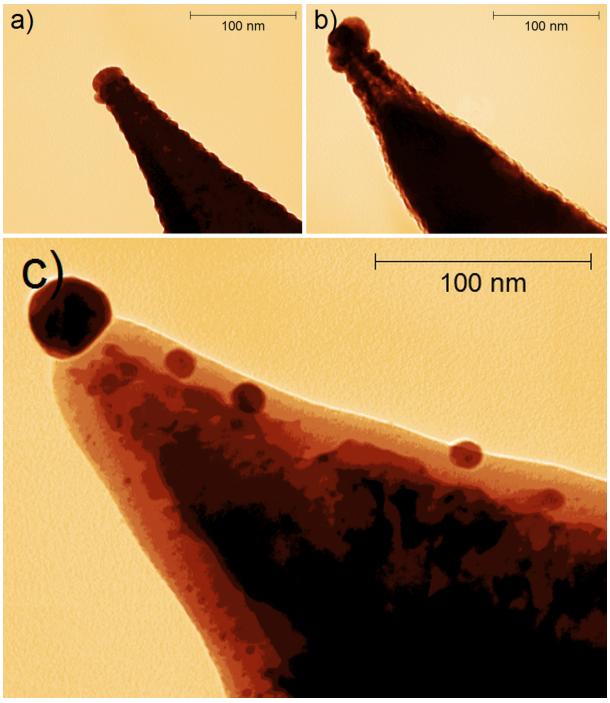

Figure 2.11: TEM images - TEM images of Pt/Ir tips (a) without thermal treatment (b) annealed at 700°C under reducing conditions (c) annealed at 700°C under oxidizing conditions.

energy. Thus migration occurs on the surface and the islands are mainly formed due to the Ostwald ripening process. This behavior will have a huge impact on the electrical properties of the annealed tips, as will be shown from the LC-AFM measurements.

The chemical composition of the tip surface was investigated using XPS presented in Fig.2.12 and the peak binding energies are summarized in Table.2.2. In particular, the $Pt\,4f$ and $Si\,2s$ level photoemission spectra were analyzed. The $Pt\,4f$ lines exhibits a spin-orbit doublet formed of asymmetric $Doniach-\hat{S}unjić$ lines for all measured samples. This is a clear indication of a metallic state and a lack of $Pt-O$ bonds(123). It is known that the formation of platinum silicides starts from the relatively low temperature of 200°C(124) thus we expect the formation of Pt_2Si or $PtSi$. The binding energy values for Pt, Pt_2Si and $PtSi$ are 71.3, 72.5 and 73.0 eV respectively(125). Thus for the reference tip the surface consists of platinum in a metallic state. For the tip annealed in air, the $Pt\,4f$ peak is at 71.29 eV suggesting a small fraction of Pt_2Si besides Pt in the metallic state. For the tip annealed in vacuum, we find that the surface mostly

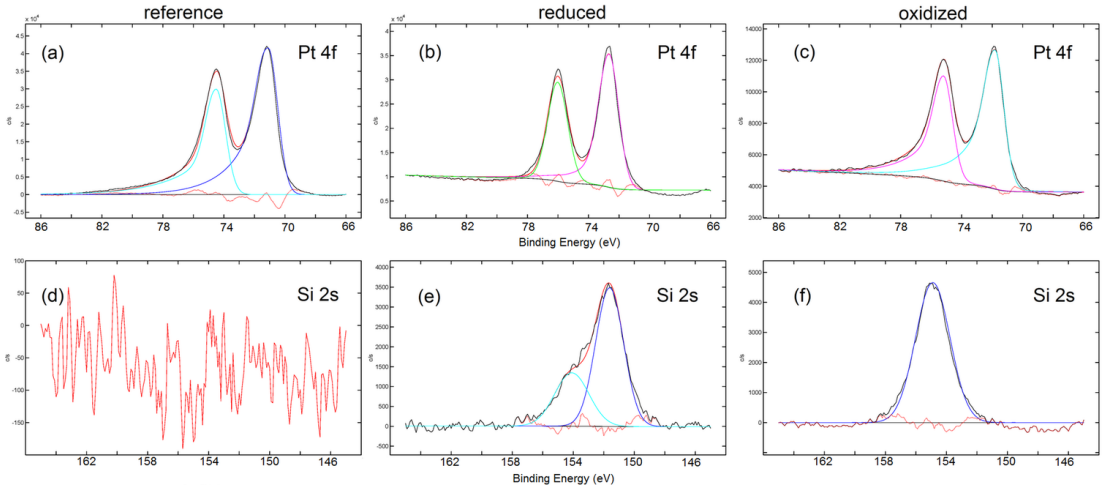

Figure 2.12: XPS investigation of tips annealed under oxidizing and reducing atmosphere - XPS spectra of Pt/Ir coating (a), (d) without thermal treatment (b), (e) annealed at 700°C under reducing conditions (c), (f) annealed at 700°C under oxidizing conditions.

consists of Pt_2Si and possibly a small fraction of $PtSi$. The data from $Si\ 2s$ peaks shows, as we would expect, that for the reference tip there is no silicon on the surface. The binding energy values for Si and SiO_2 are 151.2 and 155.0 eV, respectively(126). The result shows that the thermally treated tips are covered with SiO_2 regardless of the annealing conditions applied. Hence for the tip annealed in vacuum the SiO_2 component is only the fraction of surface silicon. The rest of the silicon comes from Pt_2Si, which corresponds well to the results from $Pt4f$ spectra. Similar results were obtained by other authors(127, 128, 129).

The topography images of the same set of cantilevers are presented in Fig.2.13 (a)-(d). Averaged values of RMS and island sizes for several 1×1 μm scanning areas per sample are presented in Table.2.3. There is an increase in the coating roughness starting from the lowest annealing temperature for all conditions. In air at 500°C film stays fairly flat and homogeneous. As the annealing temperature was increased to 600°C the islands and holes became larger, thus platinum started to agglomerate forming partially connected patterns. After annealing at 700°C the sizes of island was further increased and they become more circular in shape. The RMS jumps to almost 5 nm, the AGS to 56 nm and the AGH to 17.5 nm, moreover the films break up and become discontinuous. The same effect was clearly visible in the TEM image.

Sample	Pt 4f [eV]	Si 2s [eV]	volume [%]
Reference	71.15	-	100
Air 700°C	71.29	154.38	100
Vacuum 700°C	72.63	151.6	72.25
		154.1	27.75

Table 2.2: Binding energies of Pt 4f and Si 2s lines - taken for 3 samples: reference, annealed at 700°C under reducing conditions and annealed at 700°C under oxidizing conditions. The uncertainties are: binding energy = 0.03 eV, volume = 10%.

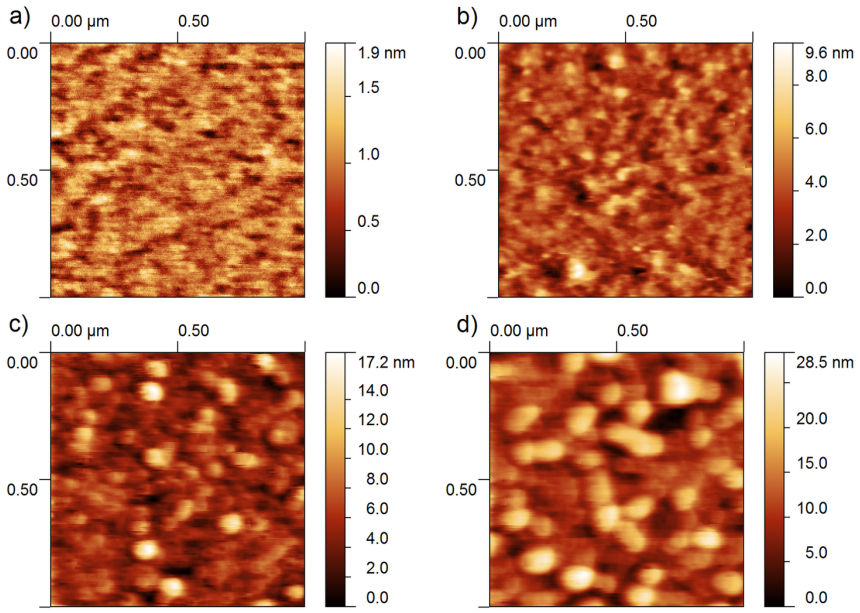

Figure 2.13: AFM topography - Topography AFM images of Pt/Ir tips (a) without thermal treatment (b) annealed at 500°C (c) annealed at 600°C (d) annealed at 700°C in air.

Sample	RMS (nm)	AGS (nm)	AGH (nm)	$R_{\square}$ (Ω)
Reference	0.30	7.9	1.6	6.61±1.26
Air 500°C	1.24	19.6	4.4	71.94±5.35
Air 600°C	2.38	28.4	9.0	452.25±14.72
Air 700°C	4.92	56.0	17.5	> 10000
Vacuum 300°C	0.39	9.8	2.2	58.12±6.94
Vacuum 400°C	0.51	10.9	2.5	78.67±6.35
Vacuum 500°C	0.67	14.8	3.4	84.58±8.22
Vacuum 600°C	0.79	16.3	3.8	92.76±7.44
Vacuum 700°C	0.89	18.4	4.3	108.55±9.13

Table 2.3: The statistical information for the various tips annealed under oxidizing and reducing conditions - the root mean square (RMS), average grain size (AGS), average grain height (AGH) and the $R_{\square}$ for all samples. The uncertainties are RMS=0.1 nm, AGS=1.2 nm, AGH=1.3 nm.

Current maps of tips annealed in air presented in Fig.2.14 mimic the behavior of the topography. For the reference sample Fig.2.14 (a) the polycrystalline character of the platinum coating is clearly visible, and many conducting spots with an average size of 8 nm can be found. With increasing annealing temperature the size of the conducting spots increases whereas the average current per scanning area decreases up to 700°C Fig.2.14 (d) where there is no current flow. The source of the rapid current decrease is twofold. First, as observed in the topography, platinum islands become discontinuous thus breaking the current paths. The connection between the ground electrode and the biased electrode (the scanning tip) is destroyed, thus there is no current flow. Second, the diffusion of Si and formation of SiO_2 on the surface already shown in XPS measurements leads to a continuous decrease in conductivity.

Island formation and growth is much slower for the vacuum-annealed tips. The topography undergoes small changes and the coating remains continuous up to the highest measured temperature. The topography images of the vacuum annealed cantilevers are presented in Fig.2.15 (a) and (c). The roughness and island size increase steadily with the annealing temperature up to 0.82 nm RMS, 18.4 nm AGS and 4.3 nm AGH for 700°C. These values are significantly lower than for the air-annealed cantilevers. This suggests that oxygen plays an important

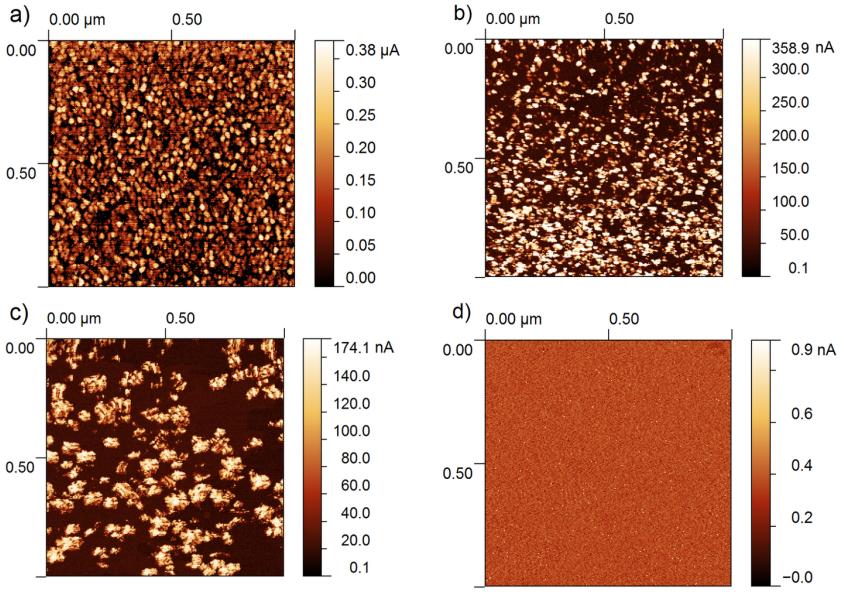

Figure 2.14: AFM local conductivity - Local conductivity AFM images of Pt/Ir tips (a) without thermal treatment (b) annealed at 500°C (c) annealed at 600°C (d) annealed at 700°C in air.

role in the formation of island structures and Pt surface mobility is thus enhanced. TEM measurements by other authors also confirm that annealing in oxygen and air leads to significantly larger Pt particles(130, 131).

The local conductivity maps presented in Fig.2.15 (b) and (d) show that the polycrystalline character of the reference sample is conserved. Large numbers of conducting grains can be found after annealing at both 300°C and 700°C in vacuum. The resistivity increases with the annealing temperature, as presented in Table.2.3. This is connected with the island formation and the variation in thickness and stoichiometry of the coating. Additionally, it is related to the formation of Pt_2Si, which has a higher resistivity value (30 $\mu\Omega$·cm (124)) compared with pure Pt (0.59 $\mu\Omega\cdot$ cm (132)). Moreover, the formation of surface SiO_2 is increasing the resistivity of the tips.

Conclusions

The observations shows that even the lowest applied temperature results in changes in the tip properties. The platinum coating tends to agglomerate and Pt_2Si and SiO_2 is formed on the tip surface. The changes are much more pronounced under oxidizing conditions, hence it can be concluded, that the maximum

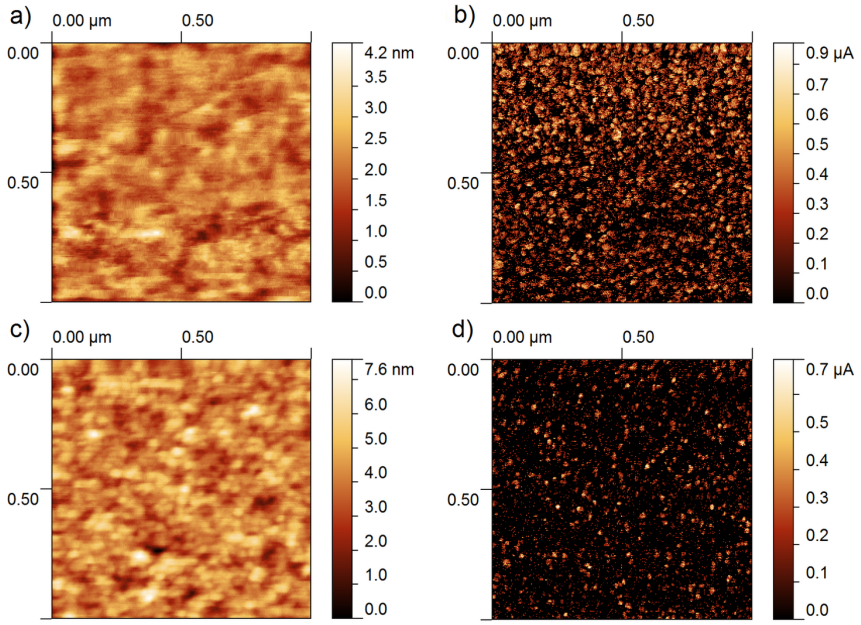

Figure 2.15: AFM performed in vacuum - Topography and local conductivity AFM images of Pt/Ir tip annealed at (a) - (b) 300°C and (c) - (d) 700°C in vacuum.

applicable temperature is close to 500°C. Above that temperature the conductivity of the tip drops significantly. Also the roughness of the coating increases sixfold, compared with the untreated tip leading to an increase of the tip apex. In the case of reducing atmospheres, heat treatment is not so crucial, so that it is fairly safe to use temperatures above 500°C.

However, the annealing time was only set to 0.5 h and I did not performed annealing-time dependency. One could suspect that in the case of normal measurements this time could be much longer. Additionally the effect of current flow can heat up the sample tip, thus leading to similar effect. One idea to ovoid errors from the tip modification is to start the experiment from the maximum applicable temperature or pre-anneal the tip for extensive time before the experiment.

2.3 Secondary characterization techniques

Those techniques provide very useful information but are not the core techniques of this work. The discussion in this section is therefore, limited only to basic description. The reader however can find more extensive descriptions in the provided references.

2.3.1 X-ray Powder Diffraction

Very brief explanation the X-ray diffraction technique will be given here. Much more detailed description can be found in many text books, for example in(133, 134). It is well known that the electromagnetic wave (such as X-ray) can interact with the matter in various ways, for example: emission of fluorescent X-rays, emission of electrons (photoelectrons) or scattering. The scattering can occurs with, or without energy loss. In the first case, X-rays transfer some of the energy to the electrons and the wavelength of scattered X-rays is changed. This is so called inelastic scattering (Compton Scattering). In the second case also called an elastic scattering, the energy of the incident X-ray remains unchanged and only the momentum is transferred in the scattering process. This process is called Thomson Scattering and is a basis of the diffraction experiments. Electromagnetic wave can be scattered in different directions, depending on atomic structure and chemical composition, thus the intensity of diffracted X-ray is strongly modulated. When the atoms are arranged in periodic manner (crystals), the resulting intensity will exhibit sharp interference peaks. Those peaks allow us to find the distribution of atoms in the crystal. For a given set of lattice planes the equation for the position of the peak can be written as:

$$n\lambda = 2d_{hkl}sin(\Theta) \tag{2.7}$$

, where n is an integer, λ is the wavelength of the X-ray radiation, the Θ is the diffraction angle and d_{hkl} is the lattice constant for a given crystal plane with hkl Miller indexes. This equation is known as the Bragg's law and is fundamental to interpretation of the x-ray diffraction data. We can see the set of different lattice lanes and the Braggs law in the Fig.2.16.

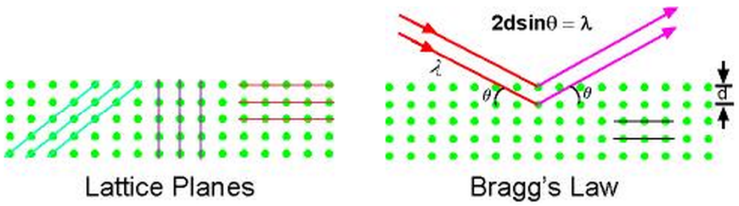

Figure 2.16: Bragg's law. - Different sets of lattice planes (left) and a Bragg's Law.

The set of peaks allows the symmetry of the structure to be determined and the lattice parameters to be calculated. If the symmetry is not known, the Space-Group, i.e. the location of each atom within the elemental cell can be determined using 4-circle X-ray diffractometer with monocrystalline sample.

XRD studies in this work were performed using Empyrean diffractometer from Panalytical in a standard $\theta - 2\theta$ geometry.

2.3.2 Low Energy Electron Diffraction

Contrary to the XRD method, the Low Energy Electron Diffraction is a surface sensitive diffraction technique. The electrons with low energy (around 150 eV) has very shortest mean free path and wavelength of 1 Å, thus are ideal for the investigation of the crystal surfaces. An excellent detailed description of the LEED can be found in various text books(135). Nowadays the LEED is one of the most widely used techniques for surface structure determination. Besides that, it is perfect for the surface state determination, since only clean and ordered surfaces can produce a clear LEED pattern with bright, sharp spots. Moreover the spots, or to be more precise the positions of the spots in the LEED pattern, may be used to find the symmetry of the surface and the unit cell length. Unfortunately, due to multiple scattering of the electrons, this determination is not as straightforward as in X-ray diffraction.

The typical experimental setup for a LEED is realized in the back-scattering geometry - Fig.2.17. The electrons with the variable energy are produced by the electron gun positioned perpendicular to the sample. The electrons are backscattered from the sample into grids, that surrounds the electron gun. There are two types of electrons that reach the grid, first the elastically scattered electrons forming the LEED pattern, and second inelastically scattered electrons, which forms the background. The inelastic electrons may make up to 99 % of the total flux and has to be eliminated by the set of grids. Next, elastically scattered electrons are accelerated to the fluorescent screen by high positive potential (several kV). This provides enough energy for the electrons to excite the fluorescent screen and the diffraction pattern can be recorded by the camera.

LEED studies in this work were obtained using LEED OCI LPS 300-D system in the UHV chamber (base pressure of 10^{-10} Torr).

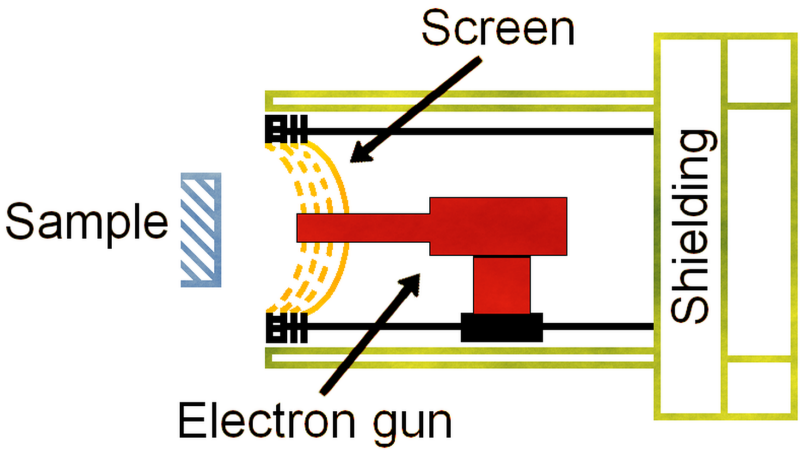

Figure 2.17: Schematic diagram of the LEED system. - The schematics for the LEED technique, the camera is installed on the right side.

2.3.3 Time Of Flight Secondary Ions Mass Spectrometry

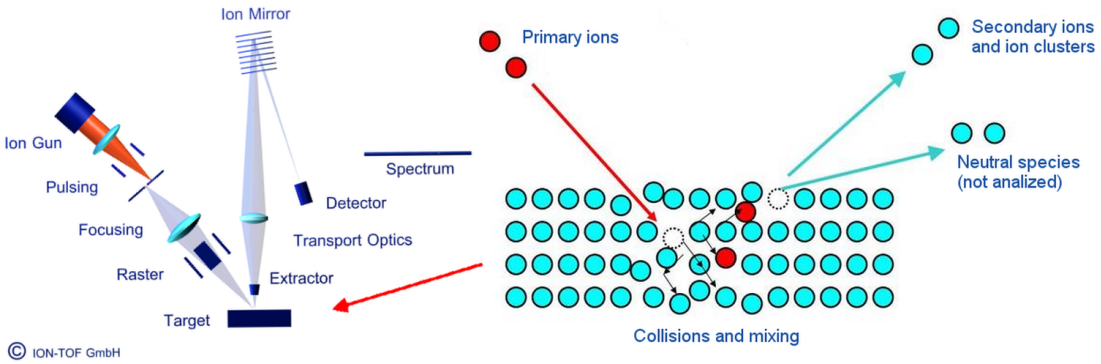

Figure 2.18: TOF-SIMS experimental setup. - The model of a TOF-SIMS spectrometer (left) and the scheme of the surface ion bombardment(right).

Time Of Flight Secondary Ion Mass Spectrometry (TOF-SIMS) is based on the investigation of ionized particles, that are emitted when a solid surface is bombarded by energetic particles. The detailed description of the process and technical implementations can be found in the literature(105). For the primary particles: electrons, photons or ions can be chosen, with the ions or clusters of ions as a most common. When a high energy (between 10 and 40 keV) beam of ions bombards a surface, the particle energy is transferred to the atoms of the solid. Various collisions occurs in the material (Fig.2.18 (right)) and a large number of

'secondary' particles such as: electrons, atoms or molecules or atomic and cluster ions are released. The TOF-SIMS spectrometry is primarily focused on ionized particles. The measurements concept is based on the the mass detector, when the 'packages' of secondary ions are first accelerated to a given potential (several keV) in order to ensure that all ions has approximately same kinetic energy, then they are allowed to move through a field free space before reaching the detector. The time of flight for each particle depends on the: the mass-to-charge ratio m/z, the acceleration potential V and the lenght of flight path L according to the equation:

$$t = L\Big(\frac{m}{2zV}\Big)^{\frac{1}{2}} \tag{2.8}$$

The flight times are electronically measured and ion mass can be calculated. Thus one receive a mass spectrum, that can be further studied. The schematic for a ION-TOF TOF-SIMS can be found Fig.2.18. It is also worth to mention that over 95% of the secondary particles originate from the top two layers of the investigated surface, thus the TOF-SIMS is considered surface-sensitive. Additionally, most of the TOF-SIMS setups are equipped with ion sputter guns. This allows to remove substantial portions of the material from the top allowing to perform deep profiles. Moreover the ion beam can be focused into relatively small spots, which in combination with the scanning motion gives the possibility to map investigated surface. In combination with the deep profiles a 3D measurements are also possible.

To summarize the TOF-SIMS can give a chemical information about the solid surface with sub-nano depth resolution, parts per billion sensitivity and lateral resolution below 100 nm. It should be noted however that the quantification is still very difficult and for most application only the qualitative data is possible to obtain.

TOF-SIMS studies in this work were performed using SIMS-5 spectrometer from IonTOF. Bi+ ion beam was used for analysis, while Cs+ was applied for depth profiling.

2.3.4 X-ray Fluorescence Spectroscopy

X-ray Fluorescence Spectroscopy (XRF) is a nondestructive method for the chemical analysis. The element analysis is obtained by the detection of the X-ray fluorescence radiation caused by the irradiation with intense X-ray beam. The detailed description can be found in the literature(136). The process of fluorescence is schematically presented on the left side in Fig.2.19. The emitted radiation can be analyzed either by energy or wavelengths sensitive detectors. The quantification is obtained by the measurement of the fluorescent X-ray intensity in comparison to provided or internal standards. The XRF is bulk sensitive method with the probing depth depending on the investigated element (several mm to μm depth). The range of elements that can be detected depends on the spectrometer itself, in this work the elements from beryllium to uranium were accessible. With the use of modern XRF spectrometers it is also possible to perform surface mapping, with resolution of several hundreds μm.

XRF studies in this work were performed using ZSX Primus II form Rigaku.

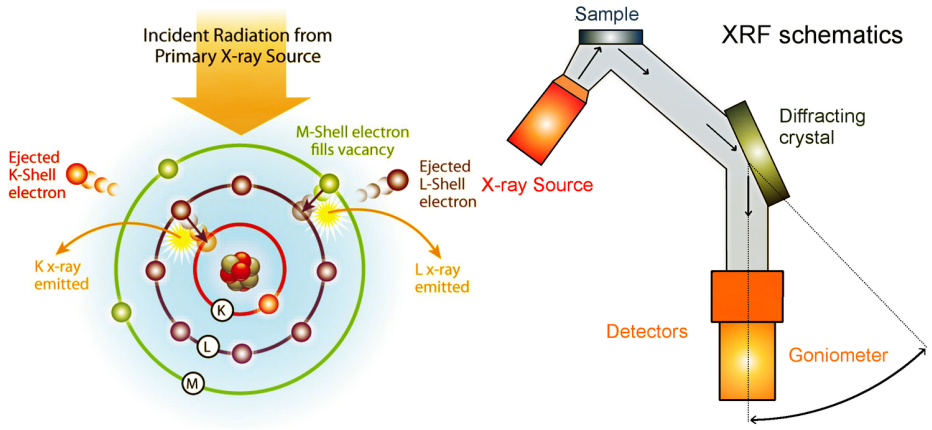

Figure 2.19: XRF experimental setup. - The basic working principle (left) and the schematics for the typical XRF system (right) are presented. The diffraction crystals are used for the wavelength detection, and are designed to cover a specific range of elements.

2.3.5 Magnetic measurements

The Superconducting Quantum Interference Device (SQUID) is typically used to characterize the magnetic properties of the materials. The short introduction

introduction will be given, but one interested in the topic can find many references in the literature(137). In general, the response of a material to a magnetic field can be quantified by the magnetic susceptibility χ, which is defined as a:

$$\chi = \frac{M}{H_a} \tag{2.9}$$

The χ is defined a an response of the magnetization M of the material to the applied magnetic field H_a. Depending on the reaction of the material to the magnetic field, one can try to differentiate all the materials into basic category:

- vacuum: $\chi = 0$,
- diamagnetic: χ small and negative,
- paramagnetic: χ small and positive,
- ferromagnetic: χ large and positive.

The schematic for a SQUID magnetometer working principle is shown in Fig.2.20. The heart of the instrument is the ring of superconducting material with one or more Josephson junctions usually in the form of thin parallel insulating layers. If the constant bias voltage is maintained in the ring, the electron-pair wave coherence results in the oscillations of the measured current. The oscillations are proportional to the change of the phase at the two junctions, which depends on the magnetic flux. Therefore measurement of the oscillations allows us to calculate the flux change in the ring.

Magnetic studies in this work were performed using QD-MPMS-XL-7AC SQUID Magnetometr from Quantum Design.

2.3.6 Mössbauer Spectroscopy

The Mössbauer Spectroscopy (MS) originates from the Mössbauer effect discovered in 1958. This effect stems from the emission of gamma radiation from a radioactive nuclei after its decays from the excited state. This radiation can in turn excite other nuclei of the same isotope giving rise to nuclear resonant absorption. However, due to recoil during gamma ray emission, some of the energy is lost. This leads to a energy shift and the absorption and emission energy distributions do not longer overlaps. Then, it is no longer possible to observe the

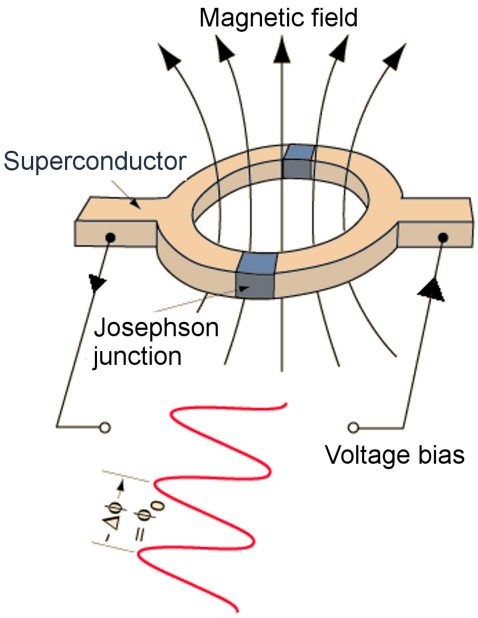

Figure 2.20: SQUID working principle. - Example of the superconducting ring with two Josephson junctions.

absorption in the sample material. Nonetheless, when the recoil energy is lower than the lowest lattice vibrational energy, that energy cannot be absorbed and consequently, there is no recoil. This effect is restricted to certain isotopes with low energy excited states. There are over 40 elements, where the Mössbauer effect was found, but the most common isotope used for the MS experiments is ^{57}Fe. Over 90 % of the available literature is focused on it. Detailed description of the technique can be found in many text books(138).

The MS is also known due to its excellent energy resolution, which originates from the energy distribution of the gamma radiation. This energy distribution is extremely small - in the order of 10^{-9} eV. Thus, in order to perform spectroscopic measurements, some energy distributions has to be introduced. In the MS experiments the radioactive source is accelerated to and from the sample inducting constantly, which shifts the emission frequency to lower and higher frequencies thanks to the Doppler effect. The schematic experimental setup for the MS is presented in Fig.2.21. In general, the MS absorption spectrum provides information about the coordination and the oxidation states of the element in question, due to the possibility to detect extremely small changes of the energy resulting

from interactions between the nucleus and its surrounding.

MS studies in this work were performed using home-build MS CEMS system.

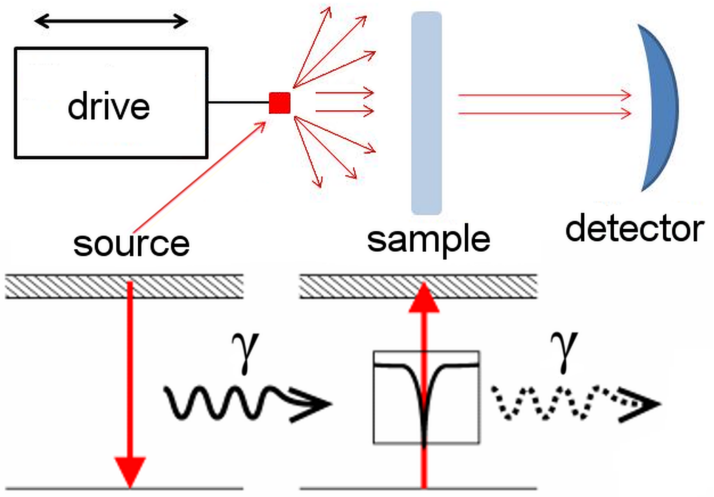

Figure 2.21: MS experimental setup. - The schematic of the MS technique. It is important to remember, that both the sample and the source, consists of the same isotope material.

2.3.7 Photoelectron Emission Microscopy

The Photoelectron Emission Microscopy (PEEM) is an technique implementing photoelectrons produced from the surface irradiated by X-ray radiation. It can be described as an combination of a SEM imaging capabilities with the XPS energy sensitivity. The schematic of a synchrotron based PEEM is shown in the Fig.2.22. XPEEM was initially developed using laboratory sources, such as Hg arc lamp, but lately the improvement and accessibility of the synchrotron radiation allowed for wider XPEEM implementation. There are few books on the topic, nevertheless some excellent reviews can be found(139).

The contrast visible in the XPEEM imaging depends on several physical phenomena and has to be recognized as such, in order to properly analyze the obtained data. First of all, there is topographical contrast that comes from the fact that the electron optics focal point is set for certain height and any deviation from it results in an decreased intensity. Moreover the distortion of the extraction field at topographical features can play an important role. Second,

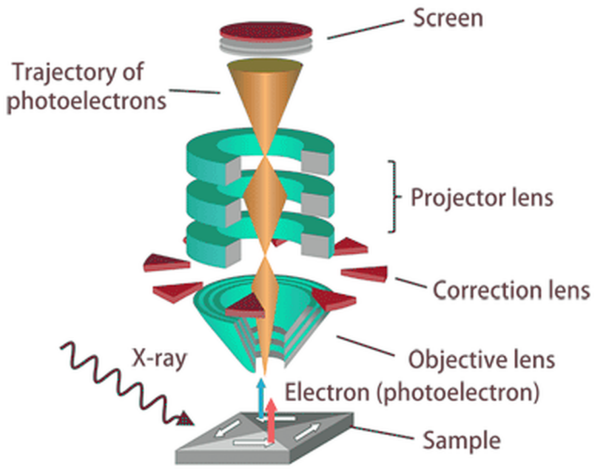

Figure 2.22: XPEEM experimental setup. - The schematic of the XPEEM technique. The XPEEM in its construction is similar to the electron microscopy, with typical resolution below 20 nm.

there is element specific contrast, which is obtained by tuning the X-ray energy to characteristic absorption edges. Third, the variation of a work function of the surface contributes heavily to visible contrast. Last, due to the magnetic interaction with the incoming X-ray beam, the imaging of the magnetic moments is possible, which is realized in the linear and circular magnetic dichroism effects for near edge resonances.

The most important features of the XPEEM are:

- high spatial resolution - routinely better than 100 nm, but better than 20 nm for specific application,
- quantitative chemical analysis - beside the elemental detection the XPEEM is sensitive for the chemical state,
- magnetic sensitivity with the use of X-ray Magnetic Circular Dichroism (XMCD) technique.

XPEEM studies in this work were performed using XPEEM (PEEMIII) from Elmitec on the PolLux beamline at Swiss Light Source (SLS) synchrotron.

2.4 Summary

The experimental part require a short summary. Nearly all of the experiments and the data analysis were done by the author personally, however there are some important exceptions that has to be addressed. The list of collaborations that were made during the creation of this work is given below:

- TOF-SIMS - dr K. Balin,
- XRD - K. Bilewska
- SEM and TEM - J. Friedrich
- XPS - dr J. Kubacki, prof. J. Szade
- LEEM - prof. J. Szade
- AFM - Ch. Rodenbücher
- XPEEM - dr M. lzak, dr D. Wilgocka-lzak and T. Giela
- MS - prof. J. Korecki
- PLD - Ch. Lenser

Once again, I would like to thank all involved in the creation of this thesis, especially prof. Szot, who contributed greatly to this work.

3

Reduction and oxidation of the crystals

The RS phenomenon creates new opportunities in the field of memory technology.(140). It allows to directly tune the electrical properties of a material, from the insulating to metallic (or semiconducting) by electrical or chemical gradients. Since the resulting changes in the resistivity are stable with time, the switching require relatively short time and are localized to very small regions of several nm, it was proposed to use RS materials as high density non-volatile memories(6).

Recent investigations showed that, both the binary and ternary transition metal oxides are most promising for RS applications. Among other, two oxides are considered a model materials: the binary titanium oxide - TiO_2(101) and ternary strontium titanate - $SrTiO_3$(12). The analysis of the nature of the RS phenomenon is being made on their basis. Moreover, from the application point of view, the effects of various doping are being actively investigated. Especially in the case of the STO, the influence of he Nb, La, Cr or Fe is under ongoing research. Additionally, a lot of interest is put into thin films of STO, and Fe doped STO thin films among other(15, 141). However, it is difficult to use thin films for the fundamental research, since one can not easily separate the substrate influence, which is an inseparable part of thin film. For example, the epitaxial STO films requires substrate (bottom electrode) with metallic conductivity and very similar (or identical) crystallographic structure like La or Nb doped STO. Such substrates however, should not change their properties and act only a sink or source of electronic charge. Unfortunately, a different behavior - the RS - was

found(14, 142).

Thus, the idea to investigate the Fe doped STO single crystal simplifies the 'boundary conditions' for the interpretation of the origin of RS, especially with the respect to the I-M transition. The complexity of the interaction found in the samples exposed to electrical and chemical gradients (or combination of both) *per se* requires usage of interdisciplinary techniques like physicochemistry of surface layer and detailed macroscopic characterization. Only such complex studies allows to present the complementary description of RS in macro- and nanoscales, and how it is related to the model of undoped STO that is present in the literature(28, 143). This chapter consist of:

1. Preliminary STO characterization.
2. Single crystals after reduction.
3. Single crystals after oxidation.

The stability of chemical composition, electronic structure and electric transport properties are investigated by a number of techniques: XRD, XRF, XPS, TOF-SIMS and AFM. The samples used in this work were single crystals of Verneuil grown STO with several nominal concentrations of iron and defined orientation were obtained from various manufacturers (primarily from CrysTec). It is also important to mention that this part is heavily based on the article, to be published by the author titled: "Inhomogeneity and segregation effect in Fe doped $SrTiO_3$ single crystals".

3.1 Preliminary STO characterization

The XRD of as-received crystals showed no additional phases apart from cubic $Pm\bar{3}m$ phase characteristic for STO structure. The cell parameter was found to be 0.3904 Åat room temperature and was not dependent on the Fe doping concentration(144). The chemical analysis by means of XRF revealed that the main contribution of impurities stems from Ni and Cu for all crystals with several dozen ppm, with other impurities well below a few ppm. The samples with the nominal concentration of 0.13 % *at* Fe were yellow, while the 0.45 % *at* Fe one exhibited a dark brown color. Further optical inspection showed however a non-uniform coloration for the untreated samples, example of such crystal can be

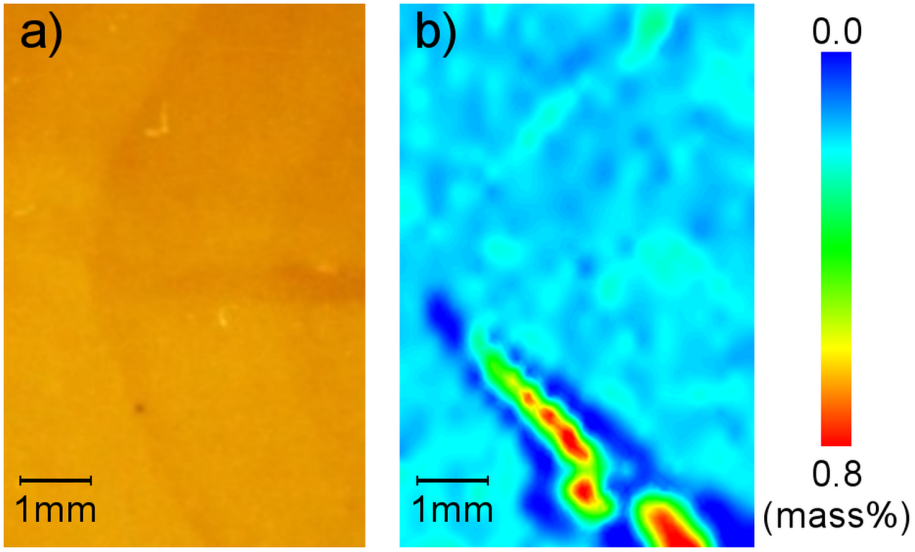

Figure 3.1: Fe doped STO sample image - Image of the $SrTiO_3$ single crystal doped with 0.13 % Fe from a) the optical microscopy and b) XRF technique in the mapping mode showing the Fe concentration map.

seen in Fig.3.1 a) for the 0.13 % Fe doped STO crystal. The visible differences in the color in the optical image originates from either: a non-uniform distribution of iron or different valency state of iron ions. In order to determine the homogeneity of iron distribution the XRF measurements in the mapping mode was performed. The results are visible in the Fig.3.1 b). The Fe concentration varies by almost an order of magnitude through the distance of tens of microns. The spatial resolution of the XRF mapping is about 0.2 mm.

Although it was found that the distribution of iron is far from homogeneous, the agreement between the differently colored regions and the iron concentration is only partial. Therefore, some of the changes in color of the untreated sample have to come from different valency state of iron ions. In principle darker color corresponds to higher oxidation state, which was confirmed by other authors(45, 46). Moreover, the color of the crystals depends strongly on the thermal or electrical history, for example in a form of electro-coloration, which will be discussed in more detail in the next chapter. The XPS experiments was also performed to measure the iron concentration and, what is more important, the iron valence state. The influence of the Fe doping on the valence band and in-

gap states was investigated as well. For the samples with small Fe concentration analysis of the Fe 2p line and atomic composition calculation was hardly possible and the analysis had to be concentrated on the sample with the higher Fe content (0.45 % at).

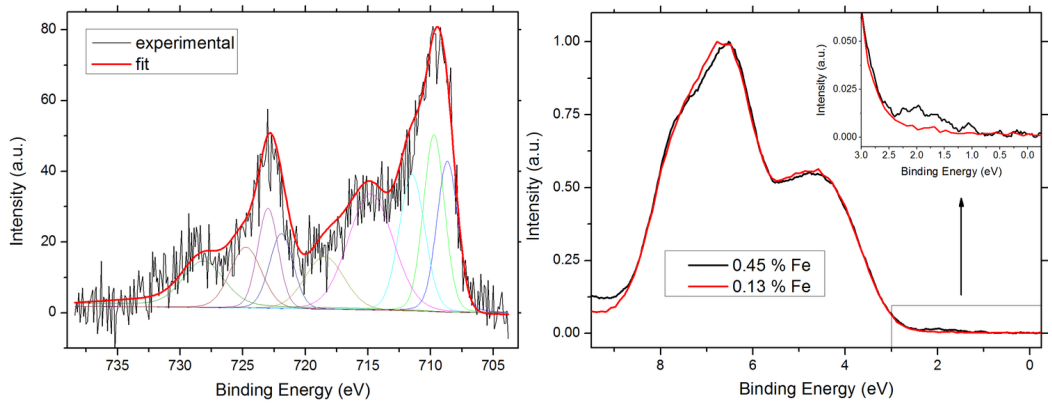

Figure 3.2: Fe doped STO sample XPS measurement - The XPS result of STO crystal doped with 0.45 % Fe a) Fe 2p multiplet together with the result of fitting and b) the valence band photoemission spectra compared to the lower doping level of 0.13 % Fe.

After the initial UHV annealing step at 300°C in order to remove the surface contamination, the calculated Fe/Ti ratio was close to 0.03. Better result was obtained after the cleaving in UHV, giving the ratio of 0.04, what is very close to the nominal value. The analysis of the Fe 2p level photoemission from the 0.45 % Fe crystal presented in Fig.3.2 allows to estimate the iron valency. By comparison to existing XPS data on Fe containing oxides (the Fe doped epitaxial STO films(83)), the fitted lines are assigned to a mixture of trivalent and divalent iron ions. One could expect a tetravalent state for an ion centering the octahedron, however the comparison with the $SrFeO_3$ where Fe is nominally fourvalent(145) shows substantial differences(43). Nevertheless, the $SrFeO_3$ shows also metallic conductivity and Fe electronic configuration cannot be treated in a ionic way for that compound. The Fig.3.2 b) shows a comparison between the valence band spectra obtained for the crystals doped with 0.13 and 0.45% Fe. The results shows low photoelectron intensity in the region of the energy gap and the sample with higher iron concentration exhibits an increased intensity in the region between 1 and 2.5 eV. The effect may be related to higher Fe content and its contribution

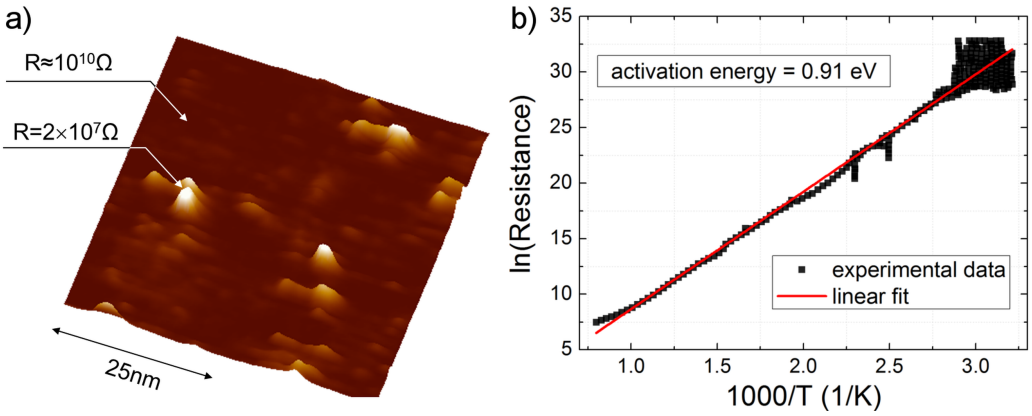

Figure 3.3: Fe doped STO sample electrical behavior - The image from the a) local conductivity at elevated temperature (250°C) under vacuum (10^{-5} mbar) and b) the Arrhenius plot calculated from the macroscopic resistance measurements of untreated STO doped with 0.13 % Fe under slightly reduced oxygen partial pressure (p_{O_2} = 100 mbar).

to the in-gap states as it was found in the Fe doped STO films(83). The Ti 2p multiplets and the Sr 3d doublet exhibited the same general structure as for an undoped STO crystal. There was no sign of reduced Ti state. The AFM topography for untreated samples exhibits atomic steps, mostly with the 3.9 Åvalue equal to the unit cell of the STO(146). In the Fig.3.3 a) one can find a typical local current map for the 0.13 % Fe doped sample obtained from the local conductivity (LC-AFM) measurements at slightly elevated temperatures. Typically, the bright spots have several orders of magnitude lower resistance than surrounding matrix and are limited to several nanometers in diameter. As it was already shown(12) well conducting regions are related to filaments formed along extended defects, which act as easy diffusion paths for the oxygen. The local stoichiometry of such extended defect is strongly modified which enables higher conductivity. A similar behavior was found in many different crystals doped with Fe. The macroscopic electrical investigation of the untreated sample shows semiconducting behavior, as can be seen from the temperature dependent measurement in Fig.3.3 b) with the activation energy calculated from the Arrhenius plot to be equal to 0.91 eV. This value is slightly lower in comparison with 1.0 eV reported for the undoped STO crystal(12).

3.2 Annealing under reducing conditions

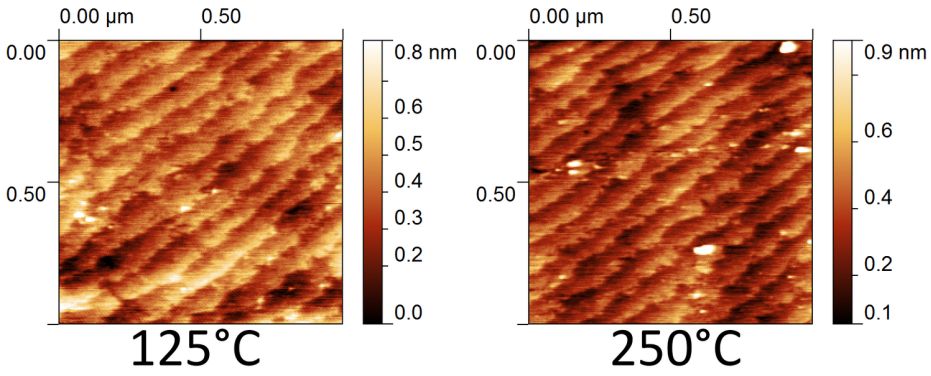

Figure 3.4: AFM measurement during reduction of the Fe doped STO sample at 125 and 250°C - The evolution of topography for the STO doped with 0.13 % after thermal treatment ranging from 125°C to 1000°C under ultra high vacuum conditions (10^{-10} mbar).

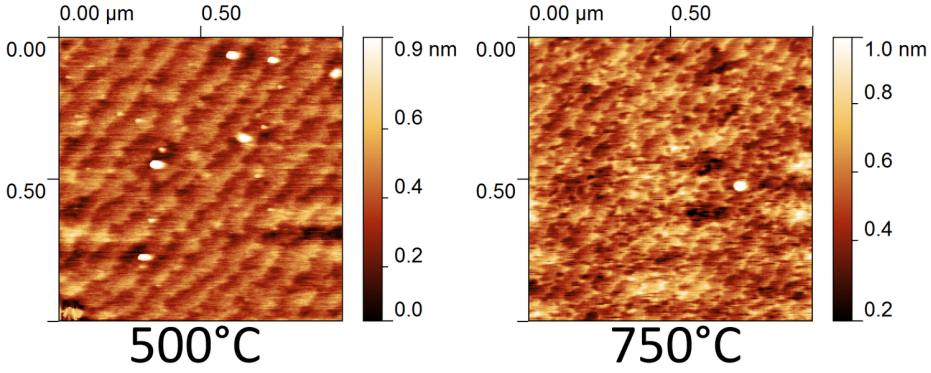

Figure 3.5: AFM measurement during reduction of the Fe doped STO sample at 500 and 750°C - The evolution of topography for the STO doped with 0.13 % after thermal treatment ranging from 125°C to 1000°C under ultra high vacuum conditions (10^{-10} mbar).

The reduction procedure consist of short annealing under UHV condition (10^{-9} mbar) for several temperatures starting from 125°C to 1000°C. The AFM measurements were done *in-situ* in a way, that sample was first heated up to the desired temperature for a 15 minutes and then measured (at the room temperature). The evolution of the topography with the annealing temperature for one of

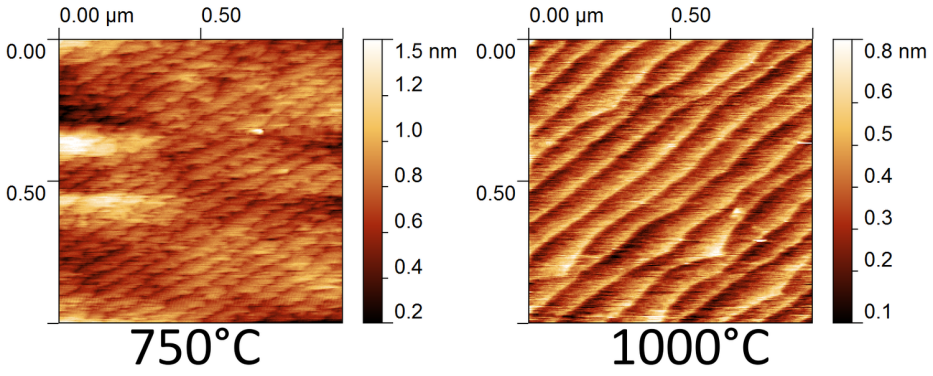

Figure 3.6: AFM measurement during reduction of the Fe doped STO sample at 750 and 1000°C - The evolution of topography for the STO doped with 0.13 % after thermal treatment ranging from 125°C to 1000°C under ultra high vacuum conditions (10^{-10} mbar).

the samples (with 0.13 % Fe) can be found in Fig.3.4, 3.5 and 3.6. One can notice that there is very little change in the terrace step height or width. This type of behavior is characteristic to a very short reduction with rapid cooling. At around 750°C - Fig.3.5 the edges of the terraces become rugged, which is connected with the surface removal of physi and chemisorbates such as carbohydrates, what was evident from the effusion experiments. After relatively short time (less than half an hour) - Fig.3.6 the steps becomes smooth, to finish as homogeneous terraces with the step height close to 3.9 Åat 1000°C. The electrical behavior of the samples after reduction at 1000°C also changes, as seen in local current map shown in Fig.3.7 a). The resistance drops by several orders of magnitude to 10^8 Ω for bright spots and 10^{12} Ω for dark spots. Besides the resistance change, one can notice an interesting conducting patterns along (100) crystallographic direction. The average distance between the conducting rows is close to 40 nm. This is unique behavior for the STO doped with Fe and was not observed previously for undoped strontium titanate crystals, which strongly suggests that conducting patterns are related to the iron doping.

The electrical conductivity in macroscale (measured by standard 2-point method under vacuum) shows a metallic like behavior after heating up to 1100°C and subsequent cooling below 700°C. This effect can be explained by taking into account the theoretical values for oxygen vacancy formation energy, which according to the *ab-initio* calculations are E_{bulk}=8.74 eV and $E_{surface}$=6.22 eV(74). The

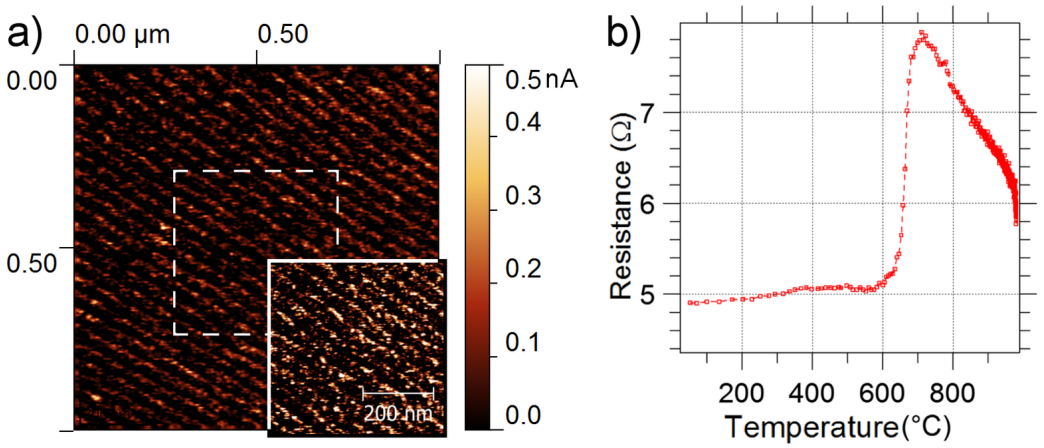

Figure 3.7: Fe doped and reduced STO sample electrical behavior - a) The current map from conductive AFM experiment (50mV of applied voltage) at elevated temperature (250°C) and under vacuum (10^{-5} mbar) of reduced sample of STO doped with 0.13 % Fe, b) the insulator-metal transition taken from the macroscopic measurements of the resistance vs temperature for of the reduced sample of STO doped with 0.13 % iron upon cooling from 1100°C.

difference in the oxygen defect formation energy is more than 2 eV, thus it is energetically favorable for the oxygen to migrate from the surface into the bulk. The surrounding atmosphere is oxygen-deficient, therefore the surface is further reduced leading to I-M transition. This observation is in a good agreement with the titanium oxidation state observed in XPS measurements performed in several cooling cycles. The changes in both topography and in electrical behavior are even more pronounced for higher iron concentrations and longer reduction times. Further investigation of the reduction process extended for a longer period of time (24 h and 1100°C) showed, that not only the electrical properties were changing, but even the crystallographic structure evolved.

For example, the XRD data for higher doped (0.45 % Fe) after extended reduction is presented in Fig.3.8. It is worth to mention that the results were obtained in the standard $\theta - 2\theta$ geometry on the single crystal sample. Apart from the STO crystal structure several titanium oxides phases(147) were found, such as Ti_2O, Ti_2O_3 and Ti_3O_5. The same effect is also clearly visible from the XPS study as a formation of Ti^{3+} and Ti^{2+} states during thermal modification at reducing atmosphere ($p_{O_2} \sim 10^{-11}$ mbar) *in-situ* - Fig.3.9. On the other hand broadening of the components of Sr 3d multiplet can be ascribed to formation of SrO on the surface - Fig.3.10. At the same time Sr/Ti ratio during heating and

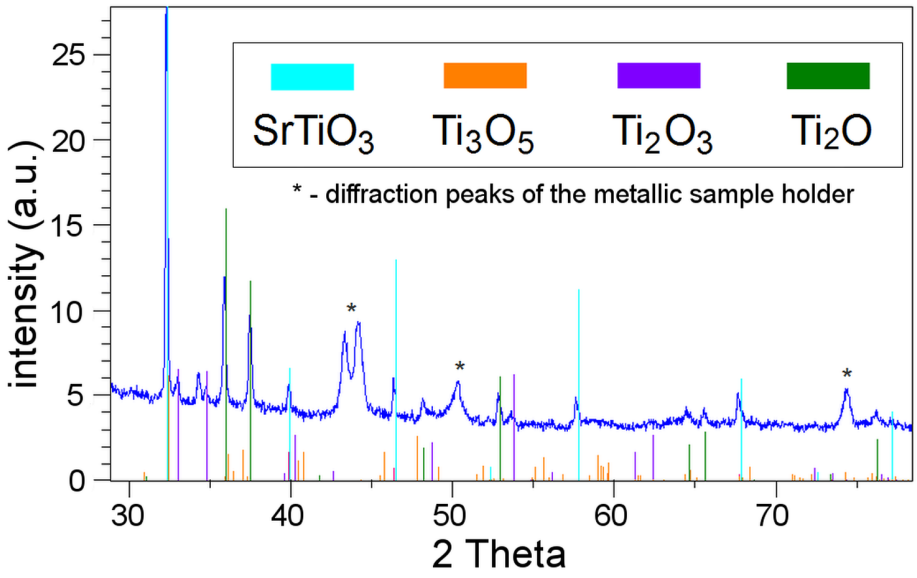

Figure 3.8: Fe doped and reduced STO sample XRD measurement - The XRD results of heavily reduced 0.45 %Fe doped STO sample. The additional phases beside the STO phase are clearly visible.

cooling cycles change considerably as shown in Fig.3.11 a). Even the temperatures as low as 500°C are sufficient to modify the top surface of the sample and result in different Sr/Ti ratios. Moreover the intensity of the Fe 2p multiplet, and thus the concentration of iron on the sample surface, gradually decreases with annealing as seen in Fig.3.11 b). This suggest the migration of iron ions from the surface into the bulk. In order to confirm this effect a depth profiling experiment with the use of TOF-SIMS was performed. The results show a steady decrease in the iron concentration starting from the surface and reaching tens of nanometers into the bulk Fig.3.12 (open points). The 2D images done during the depth profiling allowed to compose 3D images showing the Fe distribution.

While the as received crystals showed uniform depth distribution of the dopant, the reduction process greatly influenced the iron distribution showing regions where the iron content is much higher. Many of those regions formed characteristic iron-rich filaments most probably related to dislocations aligned along the (001) direction, what is shown in Fig.3.13 a). Furthermore, the XPS spectra after the long reduction and 15 minutes oxidation in air was done. As expected, Ti states with reduced valency were removed as a result of the chemical reconstruction related with the oxygen uptake. However no Fe was detected on the surface

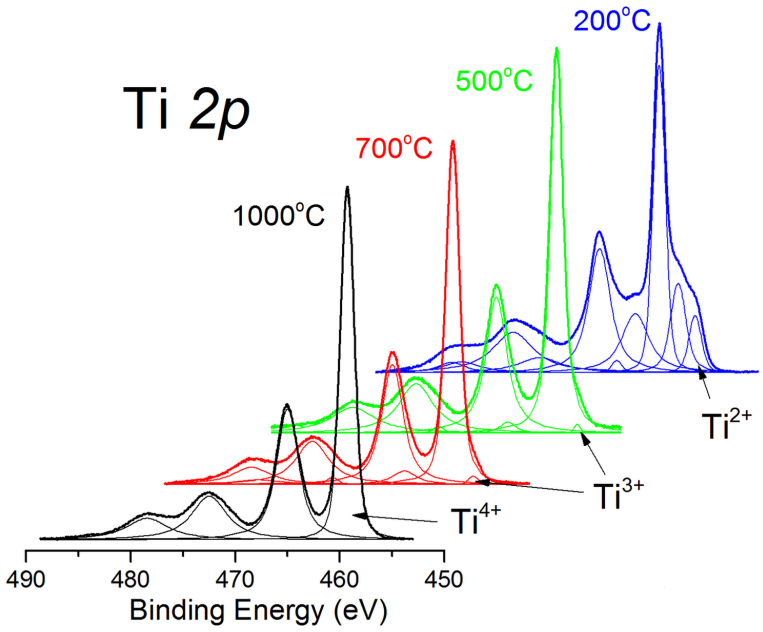

Figure 3.9: XPS measurement of the Ti core lines of Fe doped and reduced STO - The fit to the XPS Ti 2p core lines of the 0.13 % iron doped STO sample the during cooling.

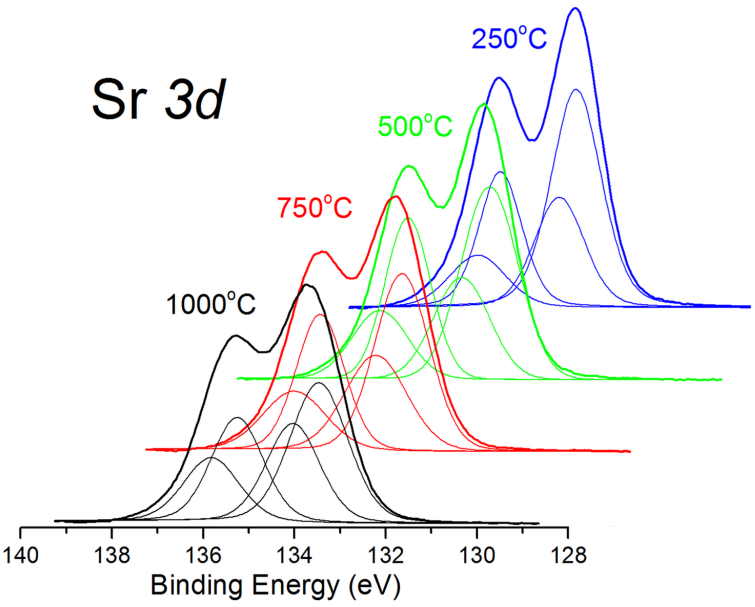

Figure 3.10: XPS measurement of the Sr core lines of Fe doped and reduced STO - The fit to the XPS Sr 3d core lines of the 0.13 % iron doped STO sample during heating.

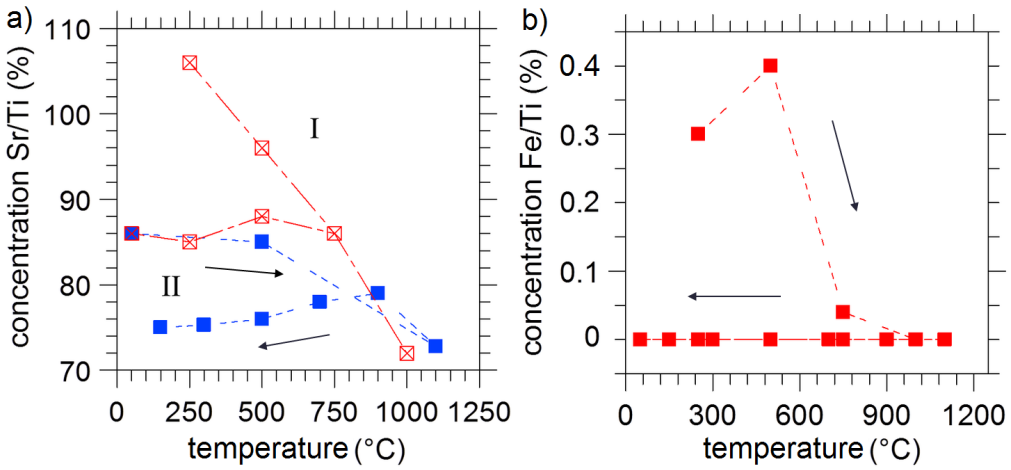

Figure 3.11: XPS measurement of the Fe core lines of Fe doped and reduced STO - The XPS results of the 0.13 % iron doped STO sample: a) the Sr/Ti ratio during subsequent heating and cooling cycles marked as I and II, b) the Fe/Ti ratio during one cycle of heating end cooling. The arrows indicate the direction of the temperature cycle.

as the iron distribution does not seem to be affected by the re-oxidation process. The re-oxidation was also performed with the use of oxygen isotope to measure the uptake of oxygen into the lattice. Samples reduced under high-vacuum conditions were subjected in-situ to an ^{18}O enriched atmosphere (97.26 % at 50 mbar) and then the depth profiles were performed.

Since the extended defects, such as dislocations, provide easy diffusion paths for oxygen, the obtained SIMS profiles are characteristic to the enhanced diffusion (pipe diffusion). The same experiment was repeated for several crystals, with changing incorporation temperature. The resulting graph is shown in Fig.3.13 b). Next, the data was fitted to the Arrhenius equation and the activation energy for the oxygen migration was calculated to be E_a=1.1 eV. This energy is in good agreement with the literature(148). All the observed changes are reflected in the measurements of other physical parameters, such as the surface topography and the local conductivity. For example the morphology of 0.45 % doped STO after prolonged reduction shows elongated, crystal-like shapes as seen in Fig.3.14 a), while the local conductivity image shows features, which are similar to the conducting lines found in 0.13 % Fe doped sample.

Yet, contrary to perfectly aligned conducting lines in 0.13 % Fe doped sample, currently observed features exhibit a direction distribution with a few degree

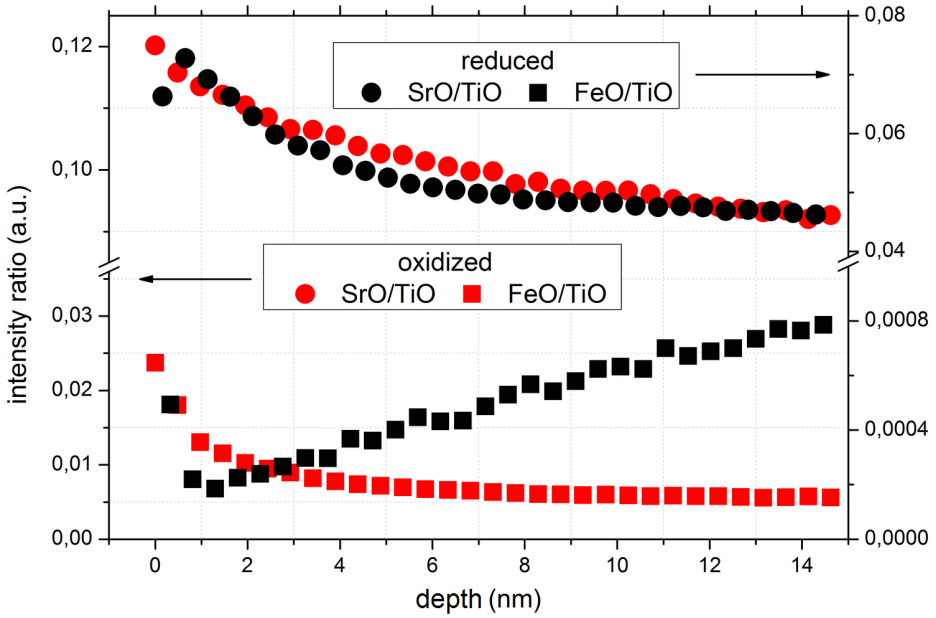

Figure 3.12: Fe doped and reduced STO sample TOF-SIMS measurement - profile - TOF-SIMS depth profiles for Fe doped STO single crystal after the reduction at 1100 °C (black points, scale on the right) and after oxidation at 1100°C (red points, scale on the left).

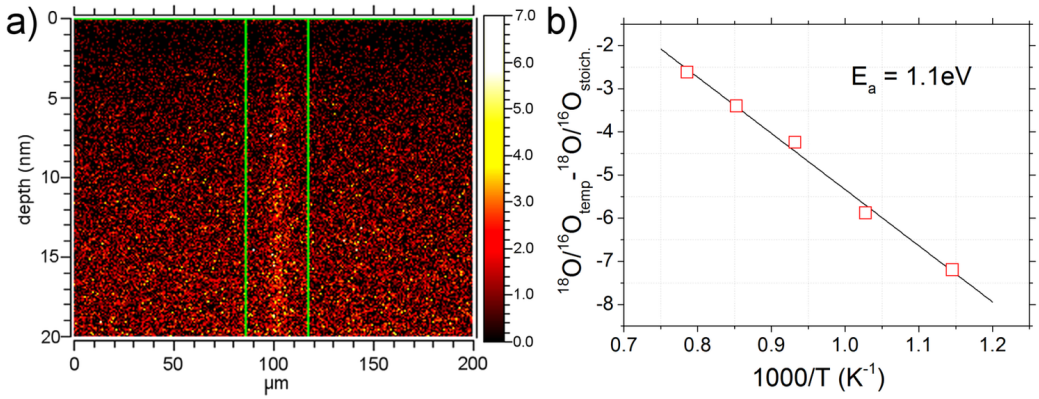

Figure 3.13: Fe doped and reduced STO sample TOF-SIMS measurement - image - TOF-SIMS results for Fe doped STO single crystal after the reduction at 1100 °C: a) the 2D slice from the 3D measurement showing FeO concentration in the plain perpendicular to the surface and b) the Arrhenius plot of the oxygen migration measured with the use of depth profiling experiments and ^{18}O as a tracer.

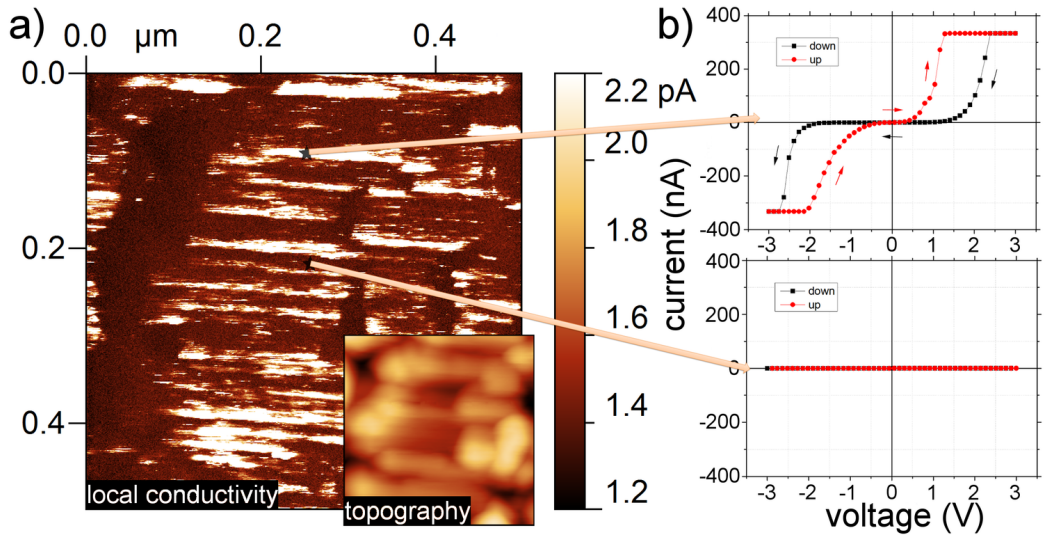

Figure 3.14: Fe doped and reduced STO sample LC-AFM measurement - The results from the LC-AFM for the reduced sample of STO doped with 0.45 % iron: a) the local conductivity measured with 500 mV bias along with the topography (inset), and b) the current-voltage (I-V) curves showing clear RS behavior (top).

spread. To have better insight into their structure, a series of magnifications along with electrical measurements was performed. The results showed that each line is in fact formed of conducting spots in the sizes ranging from several to tens of nanometers in diameter, and what is more important, they exhibit RS phenomena - Fig.3.14 b). In comparison, the regions between the conducting lines are insulating and do not show any RS behavior. It can be concluded that the SIMS depth profiles of the reduced crystals and photoemission studies show that Fe ions become very mobile at the temperature of about 700°C. Thermal treatment of the Fe doped crystals leads to a strong topographical, electrical and chemical modification of the crystal surface and the layers close to the surface.

3.3 Annealing in oxidizing conditions

For this experiments a number samples were oxidized at 1100°C and 200 mbar O_2 atmosphere. The strong reconstruction of the crystal surface was found accompanied with the formation of at least two new phases. Typical topography of 0.45 % doped sample after oxidation can be found in the Fig.3.15 a). As one

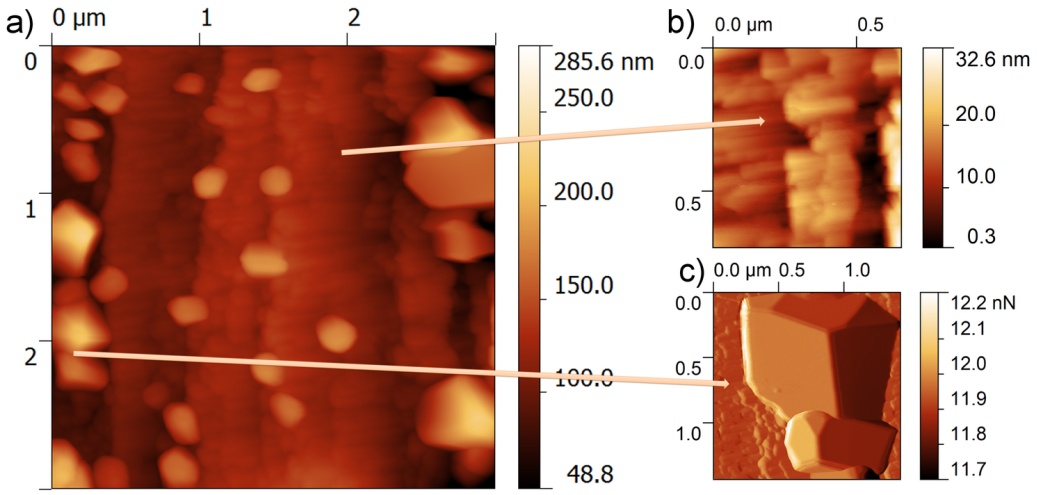

Figure 3.15: AFM measurement of Fe doped and oxidized STO sample. - The AFM results for the Fe doped STO crystal after oxidation: a) and b) the images of topography for two regions and c) the normal force image obtained in order to clearly show the formation of nanometer-sized crystals of SrO.

could expect, the surface of the STO after oxidation is insulating. No contrast in the AFM resistivity map was recorded, thus the current was lower than the equipment noise level of approximately 700 fA. This allows us to estimate the lower value for the sample resistivity for $1.4 \times 10^{13}\,\Omega$. One can notice a number of additional features (colored blue). The flat part of the topography - Fig.3.15 b) shows crystalline structure with the RMS parameter close to 4 nm. The magnification of one of the region on the crystal presented in the Fig.3.15 c) shows, that the observed objects are in fact small crystals with (or close to) cubic symmetry. The formation of such crystals was already found in the undoped STO, and connected to the formation of SrO phase(149). Contrary to the effects of reduction under UHV, oxidation leads to the increase of the Sr concentration on the surface and relative increase of the Fe content with respect to Ti as can be seen from depth profiles - Fig.3.12. To additionally confirm the results, the surface composition was investigated by the TOF-SIMS 2D maps. The results presented in Fig.3.16 show relatively strong differences in the chemical composition with good correlation between the Ti rich (red color) and Fe rich (blue color) regions. This effect is especially well visible on the overlay presented in Fig.3.16 d), where the purple color corresponds to a mixture of red and blue. This can indicate a selective segregation of iron into titanium oxides. On the other hand, the Sr rich

regions (green color) show anti-correlation with Ti and Fe, but still remains in the close vicinity of the Ti rich regions. This suggest the chemical decomposition of the surface under the influence of the oxidizing conditions and high temperature.

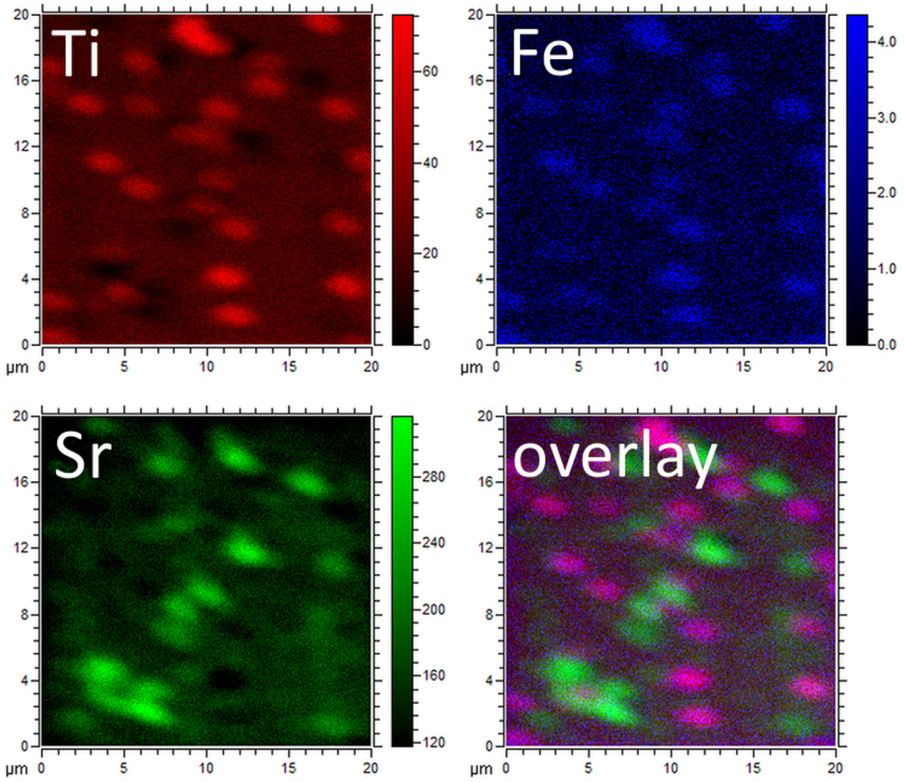

Figure 3.16: Fe doped and oxidized STO sample TOF-SIMS measurement - The 2D ToF-SIMS chemical composition maps of the Fe doped STO crystal after oxidation at 1100°C. The different colors correspond to: a) titanium, b) iron, c) strontium and d) overlay of Ti, Fe and Sr signals as indicated by the colors.

3.4 Conclusions

This chapter focused on the investigation of the STO single crystals doped with iron under the influence of the temperature and red-ox conditions. Preliminary characterization showed, that all investigated crystals (up to 0.45 % Fe) exhibited a non-uniform Fe distribution. The macroscopic XRF studies demonstrated a surprisingly high level of Fe concentration variation, which can be related to

the growth process by the Verneuil method with relatively high growth rate. At the microscopic level, the AFM resistivity maps showed stripe-like conducting structures, which are unique for the Fe doped STO system. This features are qualitatively different from the isolated conducting spots, that were found to responsible for RS behavior in the undoped STO(12). While the origin of the conducting stripes is unknown, their formation can be connected to the agglomeration of the complexes of Fe ions and oxygen vacancies at a small scale. What is more, the regularity (self organization) of the conducting stripes can be interesting for applications. The XPS data showed the existence of divalent and trivalent valence state of Fe, in agreement with the recent data for heavily doped STO epitaxial films (up to 5 % Fe)(150). The discrepancy between the results from this work and the literature, where the iron is typically at 3+ and 4+ oxidation state, can be explained by a strong association of iron to oxygen vacancies.

Furthermore, the temperature dependent studies performed in a wide range, showed the strong chemical surface instability of the studied crystals. Formation of new phases and separation of Ti(Fe) and Sr containing oxides was found for the samples oxidized at 1100°C, while reduction under vacuum led to a dramatic decrease of Fe content in the vicinity of the surface. Additionally, the Fe agglomeration suggests that the Fe ions are highly mobile at temperatures above 700 °C. While the main driving force responsible for diffusion is the chemical gradient, the path for the transport of both cations and anions must be provided by the easy diffusion paths - the extended defects. Moreover, the Fe rich filament structure was found for the first time, which was shown to be connected with the presence of the oxygen vacancies(150). Therefore one could expect that the extended defects found in the Fe doped STO single crystals, could be marked by the Fe ions.

4

Electrodegradation experiments

In the previous chapter, the behavior of the Fe doped STO crystals under the influence of high temperature and red-ox conditions was investigated. The results showed, that the stability of chemical composition, electronic structure and electric transport properties are very susceptible on the external stimuli. In this chapter, the effect of different stimulus - the electric field - is being investigated. The best example for the range of substantial changes that the STO crystals overcomes under electrical stress is the RS phenomenon itself(6, 12). It shows, that even small changes in the applied electrical field can lead to a large (at least 3 orders of magnitude) changes in the electrical conductivity. It is also known that the origin of the RS in pure STO is the I-M transition(12). The I-M transition in perovskites originates from the difference in the oxygen vacancy concentration along the network of extended defects(151). The extended defect can act as an easy diffusion paths enhancing ionic conductivity by at least several orders of magnitude, therefore even moderate thermal treatment under reducing conditions can introduce sufficient oxygen vacancies for the I-M transition(28, 101). The I-M transition can be also induced by the electric field. In fact it has been known for over 50 years that that the dc-voltage stress increases the conductivity of STO single crystals(152). This was termed as a electroreduction and was observed in many perovskites(151, 153). The electroreduction in STO is typically connected with the electro-coloration phenomena, which was extensively investigated by Waser and co-workers(154). Their experiments on the Al, Ni and Fe doped STO single crystals led them to formulate interesting conclusions:

1. In the case of Fe-doped STO, the conductivity increase during the electrodegradation process depends strongly on the iron concentration and was

found to be much higher for lower Fe concentrations.

2. Electro-migration of oxygen vacancies and the difference in their concentration in the crystal is the basis for the electro-coloration phenomena.

3. The oxygen partial pressure of the ambient atmosphere has no influence on the electro-coloration (electro-degradation) process.

Consequently, the quantitative model for resistance degradation was established on the basis of the point defect chemistry and transport equations(33). This model proved to be very reliable in several cases, such as the calculation of temperature-dependent ambipolar diffusion coefficients(155) or the conductivity profiles after after dc stress in iron-doped STO. In general the satisfactory agreement with the previously reported data can be found, although the RS behavior and the formation of bubbles under the electrode after electro-coloration showed that in fact the STO crystal is an open system and there is a significant exchange of oxygen with the surrounding atmosphere. Nevertheless other, more basic, discrepancies in the understanding and the interpretation of the STO physics and chemistry can be found. But one has to remember, that the defect chemistry is in fact a statistical approach which assumes that the defects are non-interacting and distributed randomly. What is more, is that the measurements and the great success of the defect chemistry originated from experimental measurements in macro scale. On the other hand, the nanoscale experiments reveal different, more complex world. The defects interacts with each other and forms a extended defects, which interact and governs macroscopic behavior of the crystal. In this world, the crystal acts just as a matrix for the most interesting nono-scale behavior. One can not treat the whole crystal as homogeneous sample any longer, since it is the small scale behavior that influence the behavior of the sample in macro scale. For example, in all previous electro-coloration experiments, the electrodes were either sputtered or attached to the sides of the investigated samples. Those are not very favorable conditions, since it was shown that the density of dislocations depends on the distance from the surface and is higher in the actual surface compared to the bulk(57). As a results, the defect concentration close to the surface can be several orders of magnitude higher than in the bulk, and can increase close to the edge of the crystal. Therefore, in this work a different electrode geometry is proposed (modified Valdes method).

In this chapter the results of the electro-coloration of the STO crystals will be presented. The sample used in this work were Verneuil grown STO with 0.06 % *at* and 0.13 % *at* of iron from various manufacturers (primarily from CrysTec). The samples were electroreduced at low pressure (10^{-8} mbar) and elevated temperature (250°C) using a DC voltage of 200 V. The electrical behavior with the focus on the RS phenomena was investigated during the electro-coloration experiments. What is more the evolution of the color front was observed and the AFM measurement of the oxygen bubbles trapped under the electrode was performed. It is also important to mention that this chapter is heavily based on the article written by the author titled: Electro-degradation and resistive switching of Fe doped STO single crystal(156).

4.1 Sample preparation

The Verneuil-grown single crystals of STO doped with 0.06 % Fe and 0.13 % Fe were cut into 10 × 10 × 0.5 mm^3 samples and epi-polished from both sides ((100) orientation - CrysTec, Berlin). Platinum electrodes with diameters of 1.0 mm (anode and cathode) and 0.3 mm (inner electrodes) were formed on top of the crystals. In the case of 0.06% Fe doped sample the 20 nm thick Pt electrodes were sputtered and in the case of 0.13 % Fe doped sample the electrodes were attached using high-purity Pt paste. The electroreduction procedure was performed at a temperature of ∼ 250°C under a low pressure of 10^{-8} mbar. The positive dc voltage was applied to one of the anodes with current compliance set to 10 mA (100 mA at further stages). During electroreduction, the potential drop was measured for all electrodes at all times.

4.2 Electro-coloration

Qualitatively, results for the samples with different doping were very similar, although the sample with lower iron concentration were formed significantly faster the color front emerged in a few minutes compared to several days for the sample with higher iron content. Therefore most of the results presented here are for the sample with lower iron content (0.06 %). The color of the as-received crystal was slightly brownish due to the Fe doping - Fig.4.1 a).

The experiment was started by first heating the sample to 250° C and then applying the maximum available voltage of 200 V with the current compliance

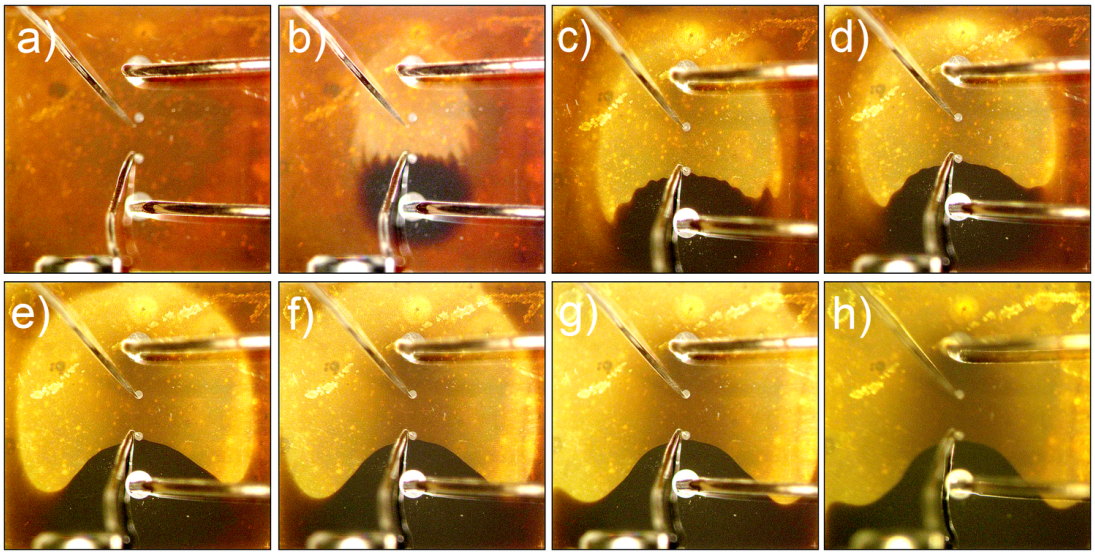

Figure 4.1: Electro-coloration process - part1 - Optical microscope images of electro-coloration process versus time: a) 0, b) 240, c) 360, d) 420, e) 520, f) 630, g) 800, h) 960 seconds. Experiment conditions: temperature $\sim$ 250°C, pressure 10^{-8} mbar, voltage 200 V, current compliance 10 mA. The bottom electrode is the anode, while the top is the cathode.

set to 10 mA. At the same time, measurement of the electrical behavior versus time was started. The first 1000 s (approximately 16 min) of electrical behavior can be seen in Fig.4.2. It is worth mentioning that the initial resistivity of the sample was roughly equal to 10 $M\Omega$ (taken from the first measured value after 5 ms of the experiment) and decreased quickly with time. The resistivity decrease can be seen from the behavior of the total current flowing through the sample (onset of Fig.4.2), which increased by roughly 3 orders of magnitude during the first 200 s to the value limited by the current compliance.

The qualitative explanation of the electro-coloration process includes the fact that under the experimental conditions used in this work (temperature close to 250°C) only the oxygen vacancies are considered to be mobile and the main point defects in the STO lattice are the Schottky defects(157). Therefore, the electric field causes the movement of charged particles in such a way that the positively charged oxygen vacancies $[V_{\ddot{O}}]$ drift to the negatively charged cathode(153). The existence of a path consisting of oxygen vacancies after the electrical stress (known as electroformation) was also shown in chromium-doped STO by X-ray absorption near-edge spectroscopy experiments(102). Simultaneously, a voltage drop

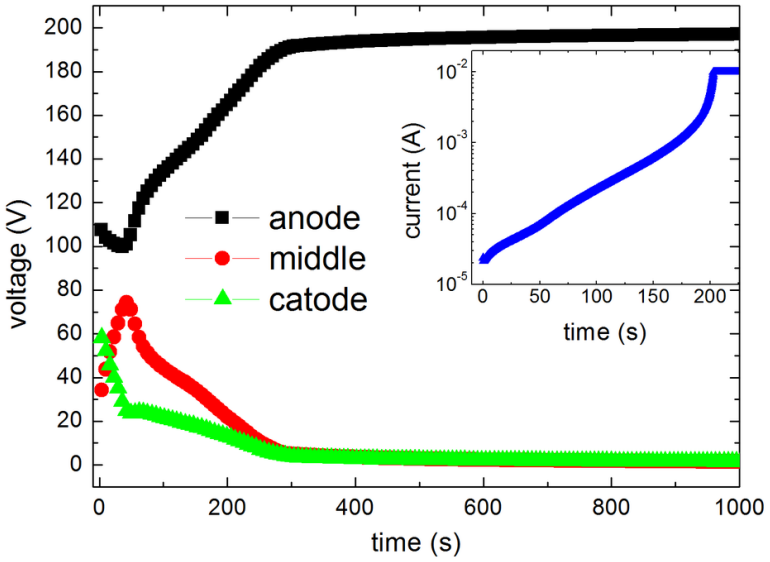

Figure 4.2: Electric measurements - Electric behavior during electroformation recorded separately for anode, cathode and middle of the crystal.

was observed across the different parts of the crystal and directly correlated with the oxygen vacancy concentration in the crystal in the following manner: increase (accumulation) of oxygen vacancy concentration at the cathode decreases its resistivity, while the opposite process is observed at the anode (Fig.4.2). At the same time, optical characterization showed that the two differently colored regions started to grow and moved towards each other until they touched. Next, the two regions grew covering the entire sample volume - Fig.4.1 b) - h). The details of the dark front movement along with the corresponding voltage drop can be found in Table.4.1. It was shown that the observed colors are characteristic of the reduced and oxidized forms of the iron in a Fe-doped STO single crystal(153, 158). The dark color around the anode originates from the presence of Fe^{4+}, while the light yellow color around the cathode originates from the iron at lower oxidation states Fe^{3+}(45). More recent examinations by electron paramagnetic resonance, Raman scattering and X-ray absorption of a very similar system - electroreduced 0.2 % *wt* Fe doped STO single crystal revealed more detailed characteristics, namely the presence of cubic Fe^{3+} centers with part of axial $Fe^{3+} - [V_{\ddot{O}}]$ in the cathodic region and predominance of Fe^{4+} in the anodic region(46). The general shape of the color boundary (front) emerging from the electrodes is consistent with the finite element calculations of the in-plane and out-of-plane electric field potential presented in Fig.4.3. The calculations assumed homogeneous conductivity of the

material.

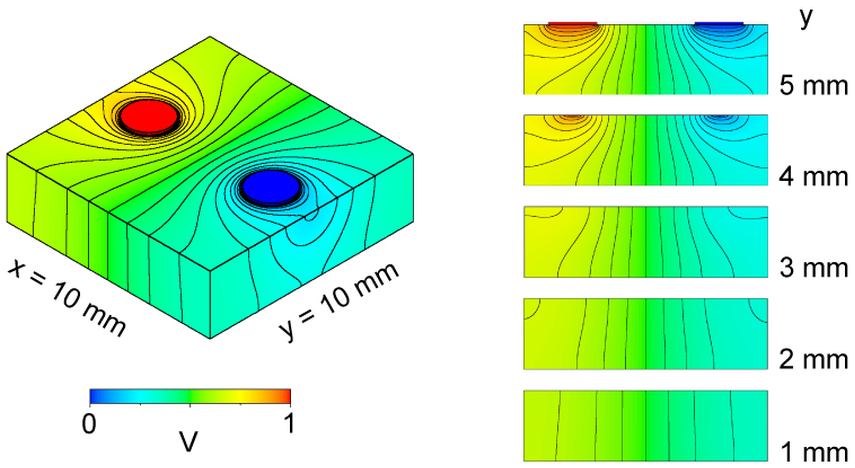

Figure 4.3: 3D electric potential distribution - 3D view of the electric field potential in the case of two round electrodes on top of the rectangular sample.

It can be seen, that in the first several hundred seconds of electro-coloration the color front becomes jagged with characteristic fingers - Fig.4.1 b), c) and d). The observed inhomogeneity is the result of the existence of easy diffusion paths, which enhance the ionic transport. An additional example of enhanced ionic conductivity can be found in Fig.4.1 h), where a small disturbance close to the very edge of the crystal can be seen (left side). The bright color there advances further down than in any other part of the crystal at this time. One can easily correlate this with the fact that the surface (or in this case edge) of the crystal has a higher density of defects than the bulk(57), which will increase the migration speed of the oxygen ions.

4.3 Oxygen migration

With the longer experimental times (up to 100 h), reduced region expands into the oxidized one as seen in Fig.4.6. This could be explained by the fact, that the ionic current is not completely blocked by the anode and by the crystal surface, and a substantial amount of oxygen is released. Since the oxygen can be released only in the region with a high positive electric field (anode), some changes in the anode are to be expected. The optical investigation of the anode material showed some topographic features, which are very similar to a bubbles - Fig.4.5 b) and

Time (s)	Dark front distance (mm)	Voltage drop across anode (V)
240	1.81	178.5
360	1.78	192.8
420	1.64	193.8
520	1.63	194.9
630	1.63	195.6
800	1.63	196.3
960	1.60	196.8

Table 4.1: Distance (measured on the line between anode and cathode) taken from the electro-coloration images along with the voltage drop corresponding to the region (anode) versus time.

c). One can assume, that the pressure of the oxygen was sufficient to deform the platinum electrode. There are other examples of similar features in various references(12, 159). Additionally, a nice example of filamentary transfer can be found in the sample after electro-coloration, namely the formation of stripes following the [100] and [010] directions emerging from the anode and propagating towards the cathode - in Fig.4.5 b).

The detailed characterization of the bubble geometry by the AFM allows to approximately calculate the pressure necessary for the formation of such bubble. For the calculations, the analytical solution for the bending of an uniformly loaded plate with a radius of a clamped at the edges was used(160):

$$h = \frac{P_0 a^4}{64D} \tag{4.1}$$

, where h is the average bubble height, P_0 is the pressure of oxygen inside the bubble. The assumed geometry in the model is presented in Fig.4.4. D is flexural rigidity given by:

$$D = \frac{Es^3}{12(1-v^2)} \tag{4.2}$$

,where s is the plate thickness, E is the Youngs modulus of the plate material and v is the Poisson ratio of the plate material.

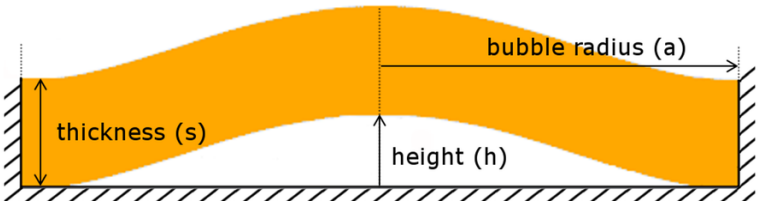

Figure 4.4: Model of a oxygen bubble geometry - Bubble geometry along with the description for the oxygen pressure calculations.

Taking the data from(161) for the mechanical properties of thin platinum films and data from AFM measurements, it was possible to calculate the average oxygen pressure inside the bubble to be equal to $6.91 \cdot 10^7$ Pa. Combining this information with the average volume of the bubble and the temperature during the experiment, the approximate number of oxygen ions trapped in the bubble was possible to estimate. Additionally, the equation of state given by the Redlich-Kwong equation of state modified by the Soave equation of state(162) with the critical parameters for the oxygen taken from the literature(163) was used to obtain the approximate value of $n = 2.0 \cdot 10^8$ per bubble. The optical microscopy shows approximately 10^5 bubbles in the anode area, thus the estimate total amount of oxygen released under the anode electrode during electrocoloration was close to $2 \cdot 10^{13}$ (10^{14} cm^{-3} in terms of volume). It must be kept in mind, that this value is the lower limit for the amount of released oxygen due to the partial transparency of the platinum films(164) or the fact that not all released oxygen could be trapped under the electrode. Although the obtained value cannot be compared directly to other types of measurements, one can try to place it in the context of the oxygen release under the high vacuum condition and elevated temperature in effusion experiments. In the case of undoped STO, the value of $3 \cdot 10^{14}$ cm^{-3} was reported(28), which is very close to result from this work. On the other hand, one cannot be sure that this amount of oxygen was in fact completely removed from the crystal; it could be possible that without electric field part of oxygen trapped inside the bubbles was incorporated back into the crystal.

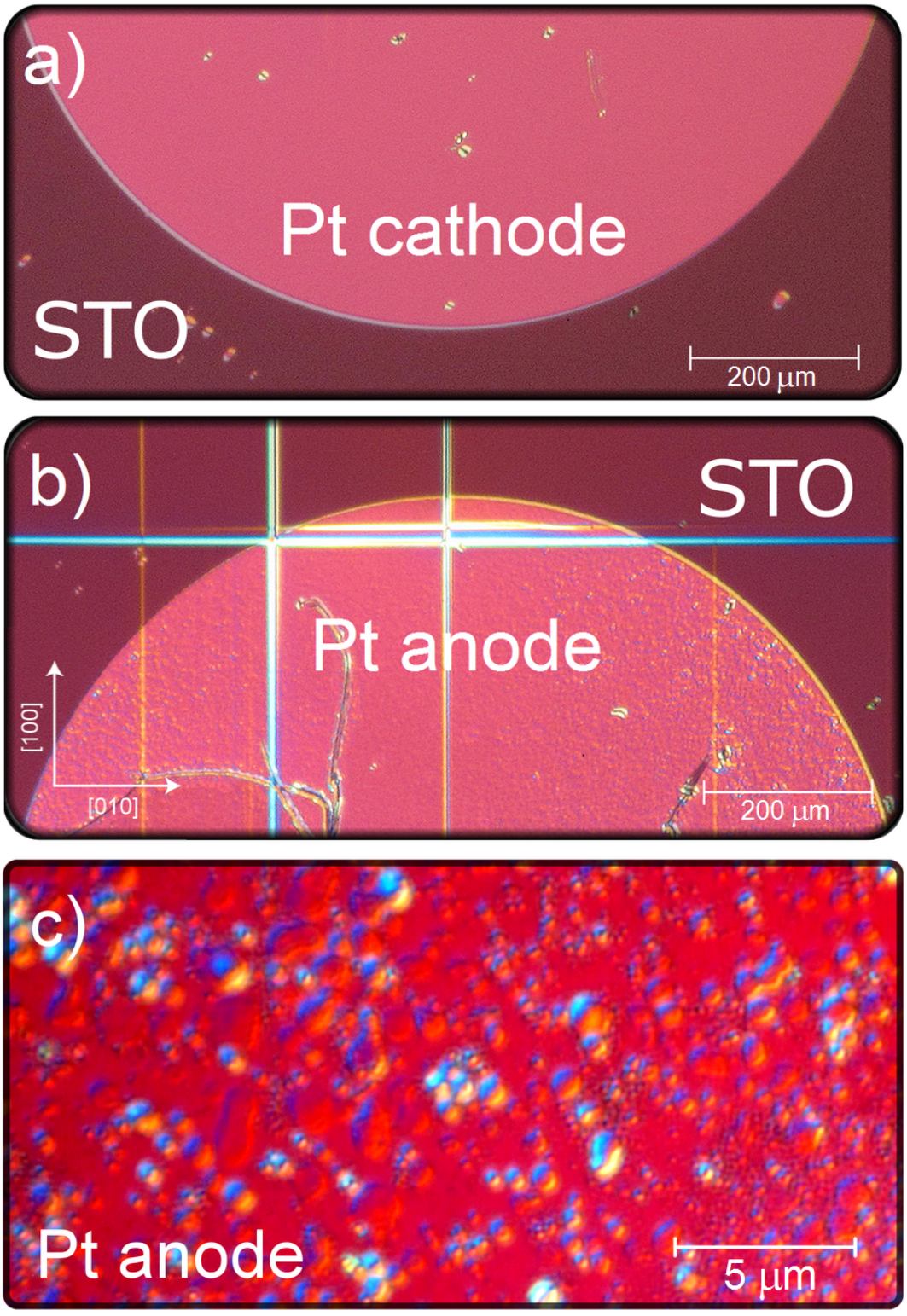

Figure 4.5: Sample view after electro-coloration - Images from the optical microscope (phase contrast) showing the sample after electro-coloration: a) in the cathode region, b) in the anode region, c) magnification of the anode region.

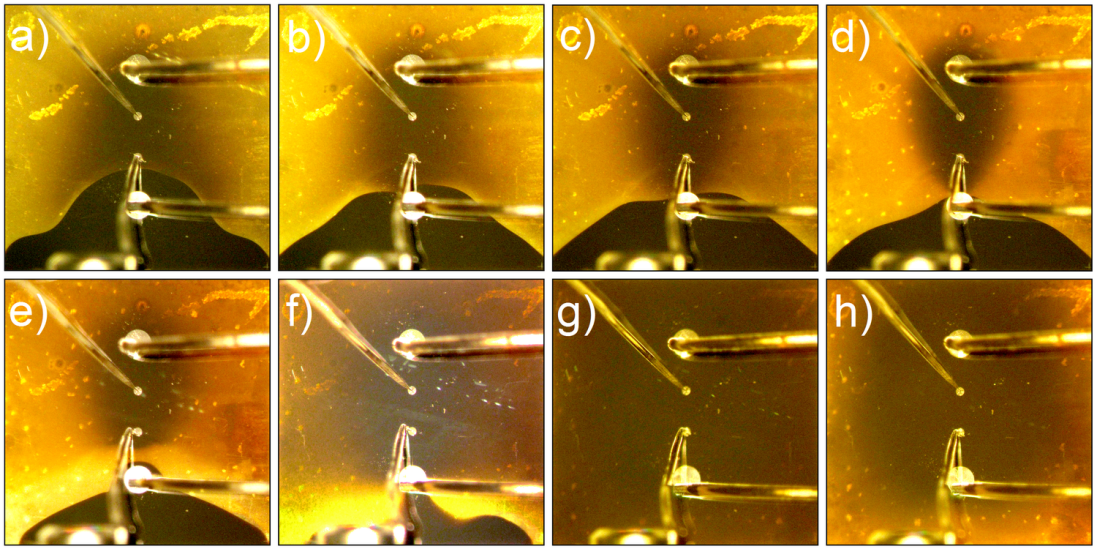

Figure 4.6: Electro-coloration process - part2 - Optical microscope images of electro-coloration process versus time: a) 1.5, b) 3.0, c) 4.5, d) 20, e) 50, f) 60, g) 80, h) 100 hours. Experimental conditions: temperature $\sim 250°C$, pressure 10^{-8} mbar, voltage 200 V, current compliance 100 mA. The bottom electrode is the anode, while the top is the cathode.

4.4 Extended electroreduction

The electro-coloration experiment was extended for several tens of hours and the temperature measurement were performed after certain time intervals. At the 20th hour of the experiment, all parts of the sample displayed semiconducting behavior - Fig.4.7 a). The total resistivity at room temperature decreased to $4\ k\Omega$. After the next 60 hours, the resistivity dropped further to $100\ \Omega$ as seen in Fig.4.7 b). The electrical behavior of the electrodes and the interior of the sample changed from semiconducting to metallic behavior. The experiment was continued for a total time of $100\ h$ resulting in the resistivity decreasing to $50\ \Omega$ at room temperature. The changes in electrical behavior can be correlated with color changes as seen in Fig.4.6 d), g), h). During prolonged electroreduction, slightly new color with blurred edges emerged from between the electrodes, slowly expanding to the whole sample. The dark region of oxidized STO as well as the bright yellow color of the reduced STO shrank leaving a uniformly colored sample after 80 h - Fig.4.6 g). Judging from the electrical measurements and from the fact that the new color emerged from the region between the anode and cathode,

where the oxygen vacancy concentration is highest(102), one can conclude that it originates from the high electron concentration (compensating high $[V_O^{\cdot\cdot}]$ concentration). This is consistent with the fact, that thermally reduced samples are also much darker than before reduction and that during our experiment the oxygen was continuously removed both by electric field and thermal reduction (substantial Joule heating at reducing atmosphere of 10^{-8} mbar). After approximately 100 h of the experiment the optical images of the sample were made - Fig.4.6 h). The edges of the crystal became brighter, again beginning from the region with the highest defect concentration (edge). Looking closely at the temperature measurements, indications of resistive switching phenomena can be found - Fig.4.7 b) and more clearly in c).

The rapid jumps in the resistivity, observed only near the anode, are related to switching between the on and off states by the conducting filaments. When the measurement was made, the system was far from equilibrium, therefore the removal of oxygen due to the electric field was countered by the migration of oxygen from the bulk through the network of extended defects, causing observable random changes in the conductivity.

4.5 Resistive switching

To confirm the RS behavior, the voltage-current (V-I) characteristics were recorded at different partial pressures - Fig.4.8. The RS hysteresis is clearly visible. What is interesting, is that RS is limited to the bulk and the anode, while there is no hysteresis at the cathode. It can be explained by the existence of very high concentration of oxygen vacancies at the cathode, which prevents the switching and the cathode is always in the on (low resistance) state. What is more, one can notice that there is some evolution in the RS behavior, namely some time is needed to reach stable switching. The switching curves always start from the low resistivity, to gradually reach lower resistivity switching curve.

The electroreduction experiment showed, that the oxygen can be easily removed from the crystal by the electric field. Thus, the Fe doped STO can be considered an open system in terms of oxygen exchange with the surrounding atmosphere. Consequently, one could predicted that by increasing the oxygen partial pressure in the experimental chamber, the overall resistivity of the system should increase. Naturally, the RS behavior should be also influenced. Indeed,

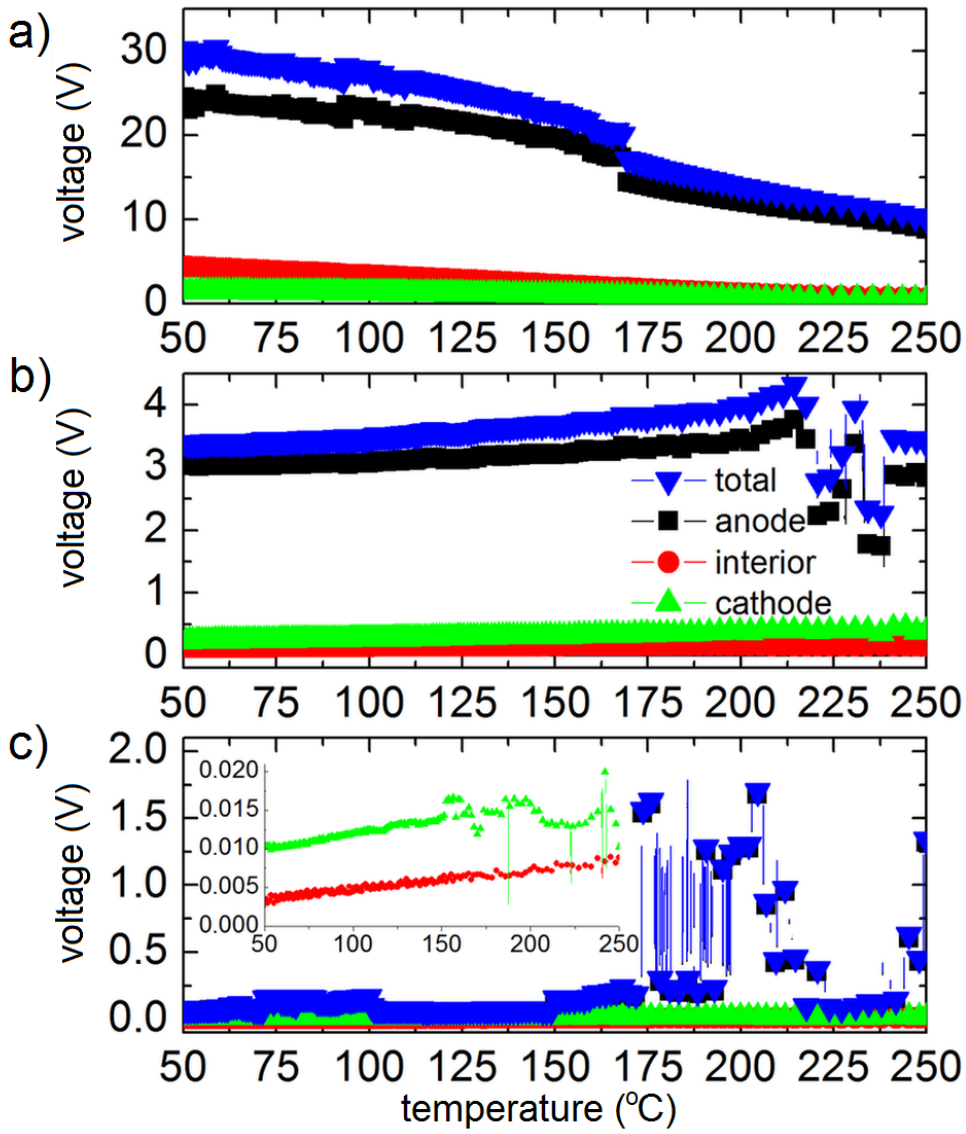

Figure 4.7: Electric measurements during electro-coloration - Electrical behavior of the sample as a function of temperature at different times of the electro-coloration experiment after: a) 20, b) 80 and c) 100 hours of electro-coloration.

this behavior was confirmed by the experiment, as the increase of oxygen pressure to 10^{-1} mbar was clearly visible in Fig.4.8. The observed changes were almost instantaneous, indicating that the process of incorporating the atmospheric oxygen into the lattice (bulk) is very fast. The oxygen bulk diffusion coefficient for STO is to small to explain this changes(165), therefore this experiment can serve as additional confirmation for the existence of fast diffusion paths.

Finally, the samples were transported *ex situ* into the UHV AFM/STM system. During this process, due to re-oxidation at ambient atmosphere, the color further changed as visible in Fig.4.9 d). The brownish/yellow color observed in the virgin sample was partially restored at the sample edges. The LC-AFM experiments performed in different regions are consistent with the previous results. The voltage applied to the conducting tip was set to -3 V for all measurements. The topography and the local conductivity maps are presented in Fig.4.9 a), b) and c). One can notice there are no significant changes in the sample topography, however the local conductivity exhibits significant differences. The cathode and the interior regions are well conducting, showing a large number of conducting spots with a diameter of 10 - 12 nm.

Those features were already observed and connected with the presence of the extended defects(12). At the same time the region close to the anode region is poorly conducting. Next the I-V curves were recorded by moving the AFM tip to one point and sweep the voltage. Such procedure was done in many points with various parameters, and the typical result is presented in the Fig.4.9. One can notice a clear RS behavior in all regions. What is interesting, that the I-V curves shows almost identical RS behavior both in I-V curve shape and the values. The threshold voltage above which the current rises significantly was found to be close to 3 V for both voltage polarities. However, there is significant difference in the smoothness of the curves: the current flowing through the cathode and the interior is somehow rugged, while the signal from the anode is rather smooth. The possible explanation for the phenomena comes from the fact, that the reduced parts of the sample (cathode, interior) were re-oxidize in the ambient atmosphere, while no additional oxidation could occur on the already oxygen-rich region (anode). The oxygen partially 'fill' the extended defect network, and when the external electric field is applied, the different 'branches' of the network will spontaneously switch from the insulating to conducting. Naturally in macro scale such 'branches' would

average over a large number and disappear from the measurements. In the nanoscale however, the measured resistivity should depend on how many of them are 'on' or 'off'. Of course a larger effect of electric field will change the oxygen (and the oxygen vacancy) concentration leading the the visible RS behavior. Additionally, the current flow will locally increase the temperature which would increase the oxygen migration. Consequently the anode region do not exhibit sharp jumps of the conductivity, since the concentration of oxygen ions is very large, and only the effect of collective movement of oxygen ions under the electric field is present.

4.6 Conclusions

The results shows the possibility of the electrical stimuli to induce the metal-insulator transition in a single crystal of strontium titanate doped with iron. Moreover, the dynamic of the I-M transition, combined with the formation of macro-scale streaks between the electrodes during the electroformation and nanoscale inhomogeneous conductivity on the surface, indicate the existence of fast ion transport paths (filaments) and the network of extended defects. The question concerning the exact nature of the enhanced ion transport, namely if the ions (oxygen vacancy) mobility is increased due to the lower symmetry in extended defects compared to the volume or if the fast transport may be caused by a local thermal excitation (regarding a filament as a 'heating rod' due to the higher electronic conductivity along extended defects) is a matter of scientific discussion. However the experiments showing fast re-introduction of the oxygen from the atmosphere observed as a rapid changes in the electrical behavior at room temperature, are in favor of the fast diffusion paths trough the extended defect network. The electro-coloration experiment demonstrated a strong connection between the evolution of the color front and the electrical properties of the investigated crystal. The RS behavior was also clearly shown, both on the large and small scale. Additionally, calculations of the total amount of oxygen removed from the crystal were performed, based on the formation of oxygen bubbles under the platinum electrode.

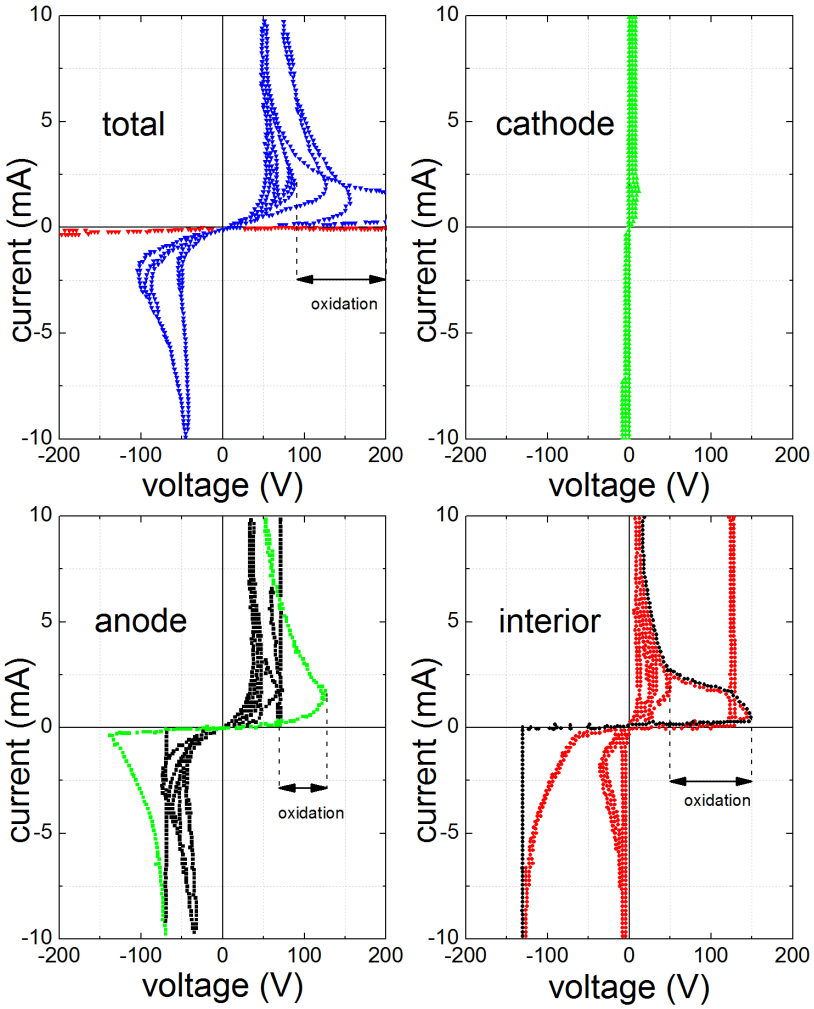

Figure 4.8: Resistive switching of STO - The voltage-current characteristics after electroreduction. The total resistivity was measured between the anode and cathode, while the bulk contribution was measured between the inner electrodes.

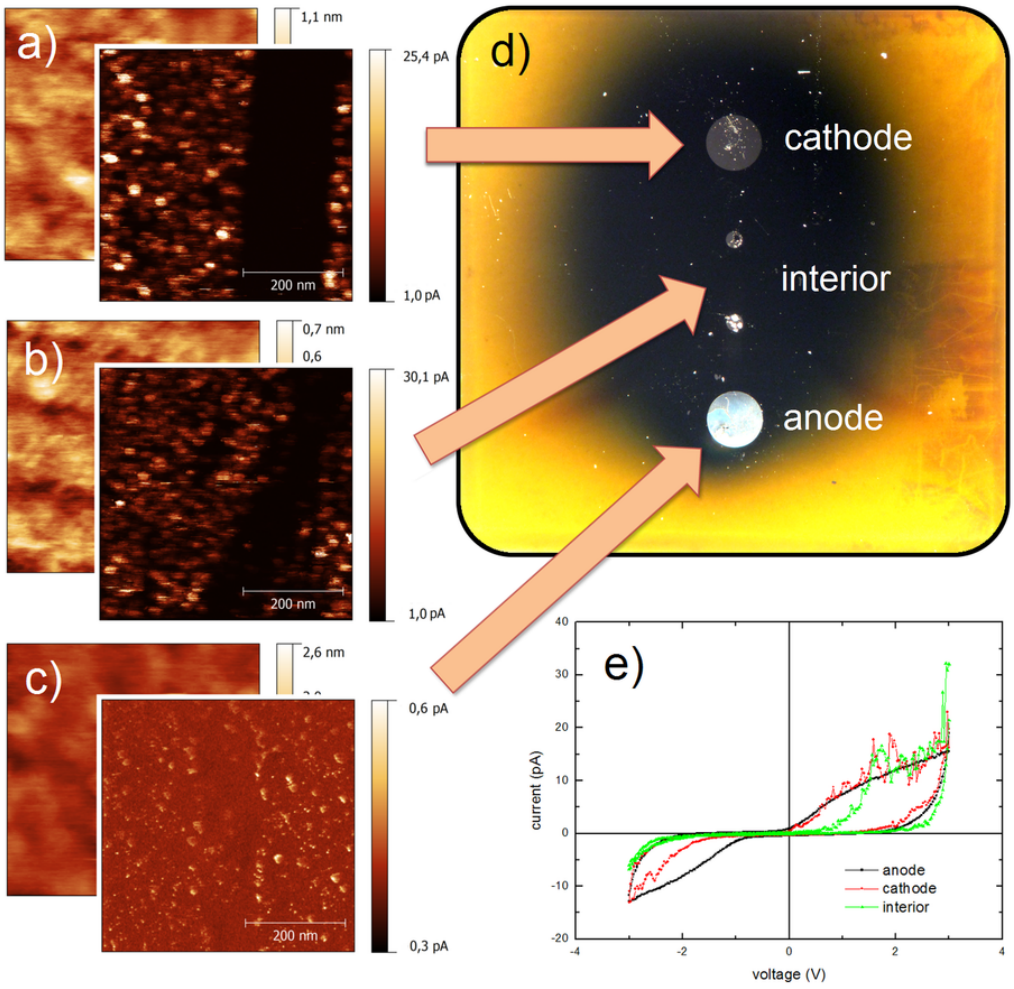

Figure 4.9: AFM measurements after electro-coloration - LC-AFM measurements of the sample after electroreduction. The topography and local conductivity maps for: a) cathode, b) interior, c) anode are presented. Optical image of the sample after electroreduction and re-oxidation in ambient atmosphere - d). The RS behavior of different components measured by the conducting tip - e).

5

Thin films of Fe doped $SrTiO_3$

While this work is focused mainly on the physics and the chemistry of iron doped STO single crystals, the applicative character of STO is also worth investigating. Unfortunately, the single crystals are not suitable for the implementation, mostly due to the high production costs. Therefore the idea of the thin films of iron doped STO fabrication emerged. Among other applications the RRAM is especially interesting, due to its non-volatile character and simplicity of use. Naturally the new type of memory has to posses a substantial advantages in comparison to the other types of memory, and in fact first RRAM possess high switching speeds and endurance, low energy consumption, good reproducibility and scalability, and finally the high density. Besides the Fe doped STO, several other RS oxides were proposed for the RRAM devices:

- binary systems: NiO(166), TiO(101), CoO(167), CuO and Fe_2O_3(168),
- ternary systems: $SrTiO_3$, $SrZrO_3$(11),
- quaternary systems: Cr-$SrTiO_3$(102) and Nb-$SrTiO_3$(14)
- quinary systems: $LaCaMnO_3$ and $Pr_{1-x}La_xCaMnO_3$(11).

Nevertheless, the Fe doped STO offers some advantages mentioned in the Chapter 1 and the thin film results can be related to, already obtained, single crystal data. Thus, this chapter focuses on the effect of the Fe doping (0, 1, 2 and 5 % *at*) on the surface properties (topography/local conductivity), electrical behavior (activation energy and band gap) and switching properties of thin films of Fe doped STO. Several techniques were implemented, such as: LC-AFM (current-voltage RS curves, conducting spot density statistic, measurement of activation

energy), XPS (oxidation states, valence band gap) and TOF-SIMS (distribution of the elements in micro- and nano- scales). Additionally, the MS and the magnetic measurements were applied in order to obtain additional information about iron distribution in the STO matrix.

5.1 Sample preparation

The typical RRAM memory cell is formed of a RS material (STO) sandwiched between the metallic electrodes. To simulate this geometry, the thin film samples were grown on the conducting substrate (STO doped with Nd), while the conducting tip of the AFM plays the role of second electrode. Nowadays a common approach for the good quality oxide thin film growth is Pulsed Laser Deposition (PLD) technique(169). It is relatively young preparation technique - the first experiments in laser deposition were carried out in the 1960s. During the 1970s and 1980s scientific interests in this technique was rather low, to finally take off in the late 1980s, after its success in growing in situ epitaxial high temperature superconducting films(170). The schematic of PLD is shown if Fig.5.1. The high energy laser working in a pulse mode is focused onto a target of the material to be deposited. With each laser pulse the small amount of the material is vaporized (ablated) and ejected from the target forming characteristic plume. The ablation plume provides the material flux for film growth. The PLD is specially interesting due to the fact that the material from the target, in many cases, is transported in a stoichiometric form. This ability originates from the non-equilibrium nature of the ablation process, where the high density of energy is absorbed by relatively small amount of target material. Depending on the energy that is absorbed by the target, one can distinguish three cases:

- low laser fluence (low absorption) - in region the laser will just heat the target causing evaporation of the material,
- medium laser fluence - the laser energy absorotpion is higher than the threshold for evaporation,
- high laser fluence (high absorption) - high energy density is absorbed causing formation of plasma plum.

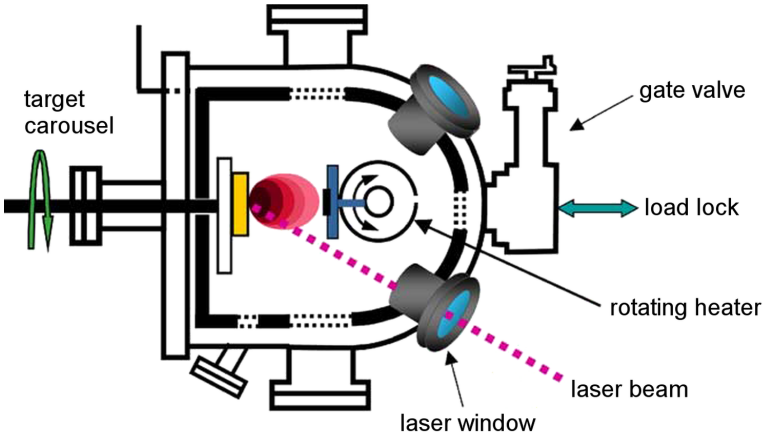

Figure 5.1: PLD - schematic - Schematic diagram of a pulsed-laser deposition system

The high absorption range the vaporization is not dependent on the vapor pressures of the constituent cations or sub-oxides. This is beneficial for the PLD technique, however such conditions requires a short duration of laser pulse, high energy density and high absorption. To meet this requirements, short wavelength lasers operating in the ultraviolet are used; typically excimer lasers operating at 193, 248, or 308 nm with pulse width of tens of nanoseconds and a laser pulse energy of several hundred mJ. The amount of the deposited material with each pulse depends on various factors, such as the background pressure, laser energy, target absorption coefficient and target-sample separation. Moreover the PLD technique provides several features that are desirable in the thin oxide films production:

1. It is possible to precisely control the growth process to the atomic level maintaining high deposition rates up to 100 Å(171).

2. The PLD technique can work effectively in large range of the background pressures, starting from the UHV to approximately 100 Pa(172). This is specially suitable for the oxide thin film production for two major reasons. First, in the production process an oxidizing agent is required (e.g. molecular oxygen) to allow the ablated cations and molecular oxygen to react. Second, in some applications the reduce of the kinetic energy of ablated species is necessary, which depends on the PLD chamber background pressure. Such moderation is necessary, since the plum can produce species

relatively high kinetic energies (up to 100 eV), which is sufficient to create defects in growing films.

3. The deposition using PLD is possible using either single or multiple targets. There is no specific requirement for the form (single crystal - ceramics), as long as the material possess a high optical absorption coefficient at the laser wavelength. What is more, the phase of the target does not need to be identical to the desired film, only the cation stoichiometry has to be. One has to keep in mind that the plum geometry and the thickness distribution is in general non-linear and that the material distribution depends strongly on both the laser (laser fluence, intensity profile, laser spot aspect ratio) and on the target (lasertarget interaction, physical properties) parameters.

There are also disadvantages of the PLD process. One of them is the possibility to eject micro sized particles, which can cause a island growth and are the source of strains and defects in newly deposited films. To avoid this problem, high density targets, velocity filters(173), off-axis laser deposition(174) or line-of-sight shadow masks(175) were implemented.

In this work, several samples of 20 nm thick Fe-doped STO with 0, 1, 2 and 5 % *at* concentrations were grown. Additionally, sample of 5 % Fe doped STO with 100 nm thickness was prepared for more bulk-sensitive techniques. To ensure the homoepitaxial growth the substrate was chosen to be Nb-doped STO single crystals (0.5 % *at* niobium concentration). As the ablation laser the KrF excimer laser 248 nm was used. Other parameters were set to: laser energy density 1.55 Jcm^{-2}, repetition rate of 5 Hz, deposition temperature 700°C and oxygen partial pressure of 0.25 mbar. It is necessary to mention that all samples were prepared by the Christian Lenser, who worked (at the time) in the Peter Grnberg Institute (PGI-7) Jlich. Prior to the measurements done under UHV conditions (10^{-9} - 10^{-10} Torr) the samples were heated to 300°C for the duration of 0.5 h in order to remove most of the physi- and chemi- sorbates from the surface.

5.2 Surface crystallography

The effect of the Fe-doping was investigated by the XRD technique, showing the crystal structure identical to the single crystal one. The cell parameters were also very close, however the the elongation in the c-axis with increasing Fe content

was found. The specific reflection of (002) was chosen to show the changes in the c-axis - Fig.5.2. The observed changes were most probably a result of the increasing point defects (and related extended defects) concentrations. Additional investigation by the LEED yielded 4-fold symmetry and P(1×1) structure, characteristic for (100) STO surface. No additional reflections were spotted, thus good quality STO surface was confirmed. Representative LEED patterns for a 0, 1 and 2 % doped samples are presented in the Fig.5.3. One can notice, that higher iron concentration influences diffraction spots sharpness - Fig.5.3 b) or the overall intensity - Fig.5.3 c). One can conclude, that larger Fe doping introduces higher quantity of structural defects (point and extended defects).

5.3 Surface composition

To measure the surface composition a high-resolution TOF-SIMS images were recorded. No major chemical inhomogeneities were found, besides the occasional micro-meter size inclusions. Those inclusion can originate either from the substrate itself or from the PLD technique, as mentioned in the sample preparation section. In-plane distribution of strontium, titanium and iron in the micro meter scale is presented in the Fig.5.4. Besides the Sr, Ti and O, trace amount of Na or Cl were found, which is a typical surface contamination. What is interesting some amount of Nd was also found. The only possible explanation is that it migrated from the substrate during thin film production. The investigation in smaller scales (2 μm × 2 μm) with the resolution of around 100 nm also showed no signs of in-plane inhomogeneities - Fig.5.5. All measured samples exhibited very similar properties, thus most of the results presented in this section comes from the sample with the highest doping.

The depth profile was also performed and the results were recalculated using tabulated values for the sputtering ions (sputtering energy of 0.5 keV) and the ion yields of measured elements(176). One can notice a small modulation of the titanium to strontium content, with the ratio of Ti/Sr close to 1 - Fig.5.4 d). The initial increase in the Ti concentration was very similar to the case of STO single crystals reduced in vacuum(149). Iron content showed constant decrease through the film thickness (around three times the starting concentration), while the concentration close to the surface was determined to be very close to the nominal one. A small increase at the interface between the substrate and thin film can

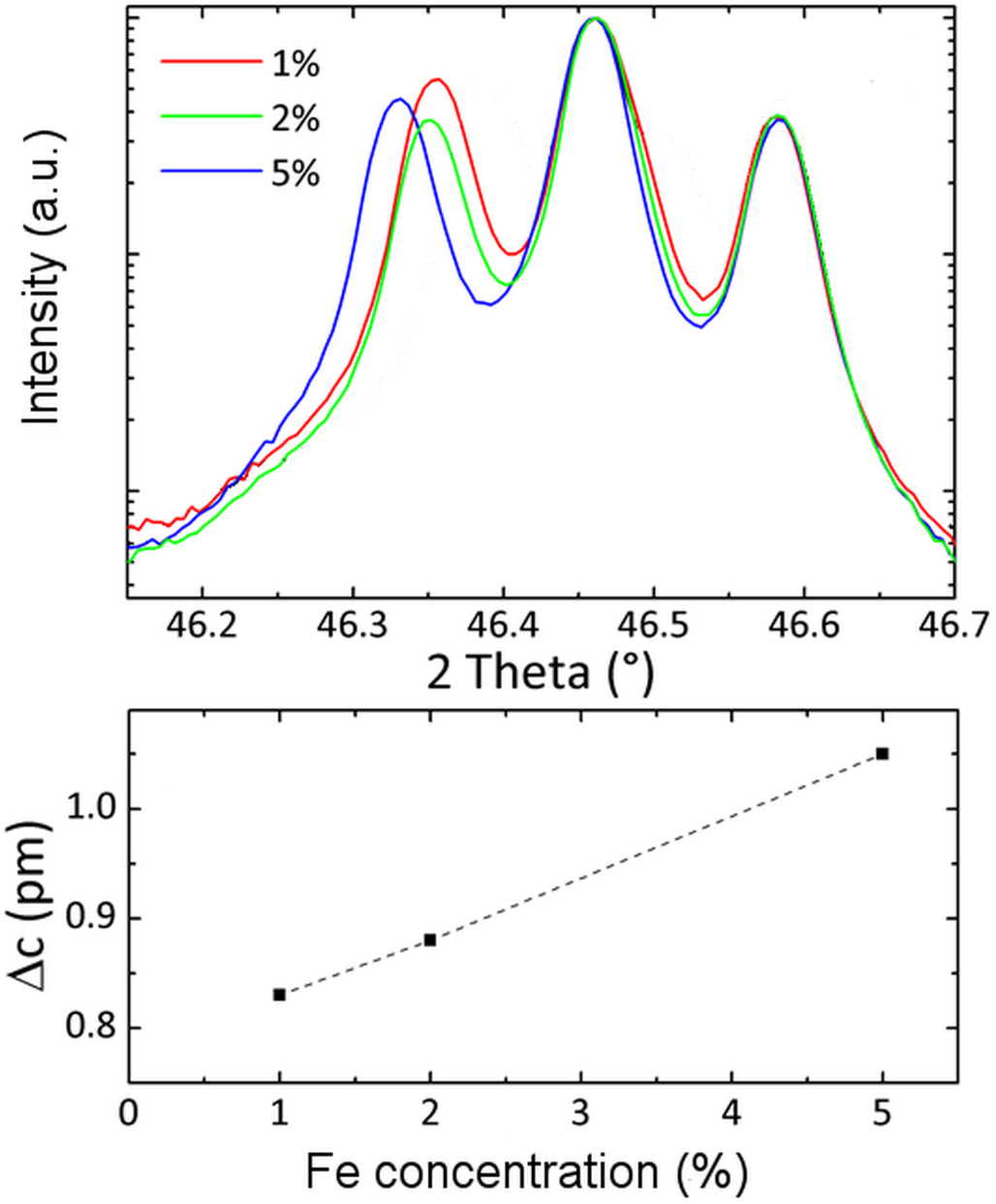

Figure 5.2: XRD results of Fe doped STO thin films. - The (002) reflections for the increasing Fe doping concentration for the investigated STO thin films (top) with the c-axis elongation graph versus the doping concentration (bottom).

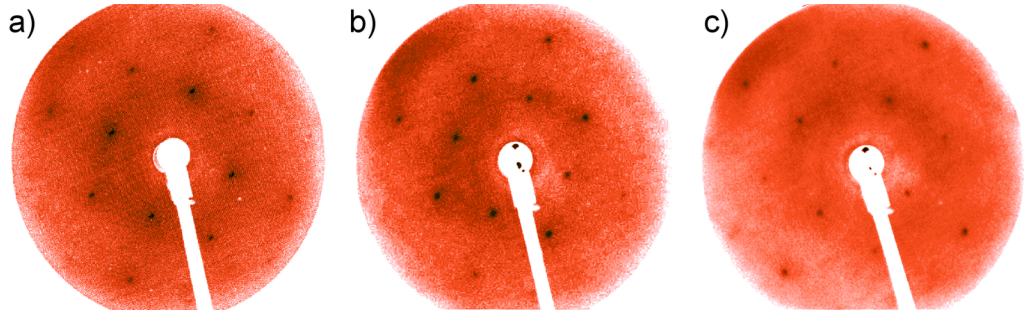

Figure 5.3: Typical LEED pattern for the Fe doped STO thin films. - A clear 4-fold symmetry characteristic for the cubic STO is visible. The LEED patterns of: 0 % Fe doped sample also called the reference sample a), the 1 % Fe doped sample b) and the 2 % Fe doped sample c). The LEED patterns were recorded for the electron energy close to 100 eV for each case.

Component	standard geometry 45°	grazing geometry 15°
1 % Fe	1.2 - 1.7 %	2.5 %
2 % Fe	2 - 5 %	10 %
5 % Fe	9 - 13 %	17 %

Table 5.1: XPS concentration measurement of the Fe doped STO thin films. The results from measurements in two geometries - normal and grazing - for the Fe concentration of Fe doped STO thin films. Data shows that the Fe concentration increases close to the surface.

be also noticed. Obtained results are consistent with the XPS measurements, where the increase of the iron concentration depending on the distance from the surface was detected. It was done by changing the angle of XPS detection and the X-ray radiation relative to the sample surface. The results for all samples and two different measurement geometries are presented in the Tab.5.1. It was found that the Fe and Nb migrates towards the sample surface. The mechanism for the migration can be similar to the one noticed in the single crystal sample described in the chapter 3. The extended defects plays a major role in this process, enhancing migration.

Further investigation of the Fe inhomogeneity in thin films led to the implementation of TEM technique, which showed large inhomogeneous contrast both

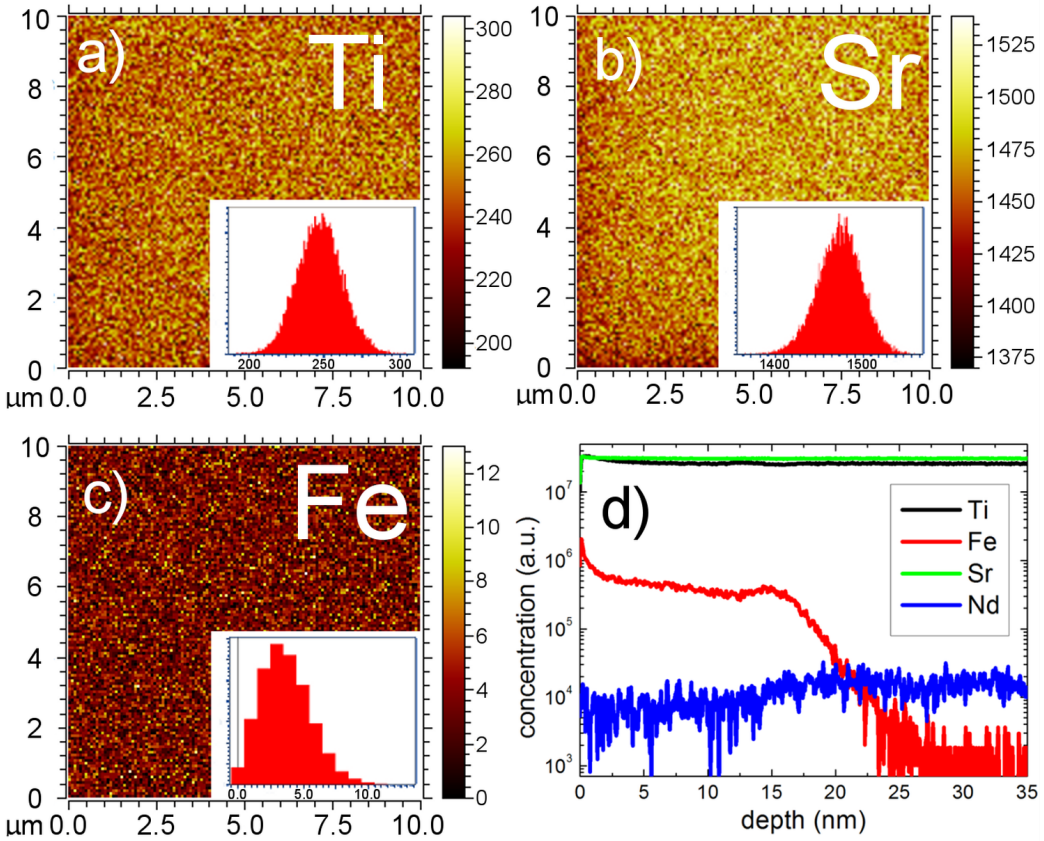

Figure 5.4: Surface element distribution for STO thin films. - TOF-SIMS measurements for the STO doped with 5% Fe along with the histograms of element distribution: a) titanium, b) strontium, c) iron and d) deep profile showing Ti, Sr, Fe and Nb components.

in bright and dark field of view - Fig.5.6. The contrast can not be directly correlated with the iron distribution, nevertheless it can illustrate that the thin films structure are far for perfect at nanometer scale. The measurement were performed at Peter Grünberg Institute (PGI), Forschungszentrum Jülich.

5.4 Further Fe inhomogeneity investigation

The XPEEM experiment were performed in order to obtain high magnification, chemically resolved images of 20 nm resolution or better (in perfect conditions). The highest contrast can be achieved for samples consisting of elements well spaced in the periodic table. In the case of Fe doped STO, there very little sepa-

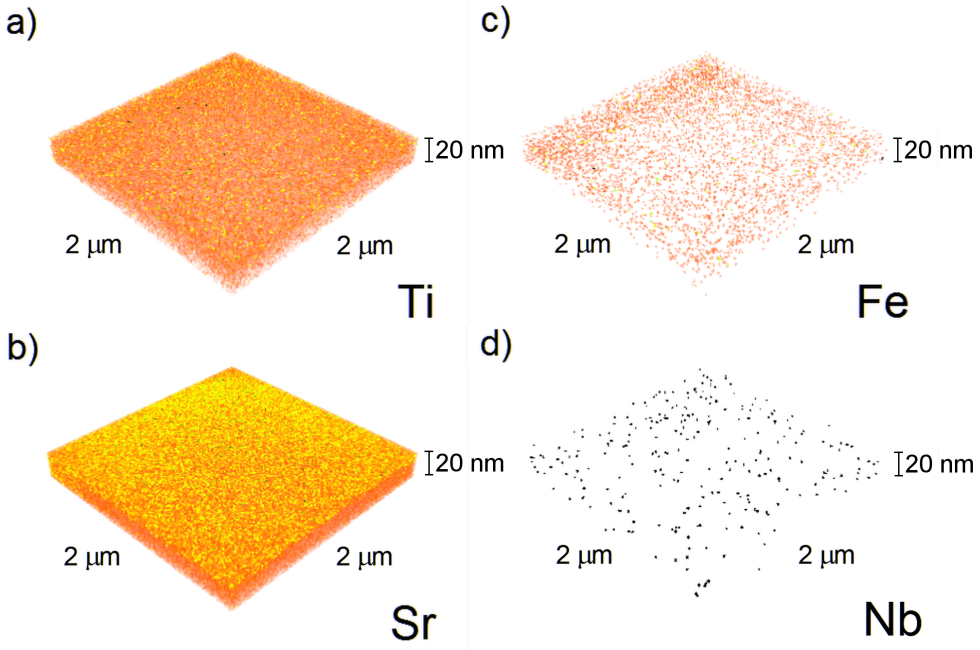

Figure 5.5: 3D image of element distribution for STO thin films. - The TOF-SIMS elements distribution in a form of 3d-pictures for the $SrTiO_3$ doped with 5 % Fe in a 2 μm × 2 μm scanning area. The showed elements are: a) titanium, b) strontium, c) iron and d) niobium.

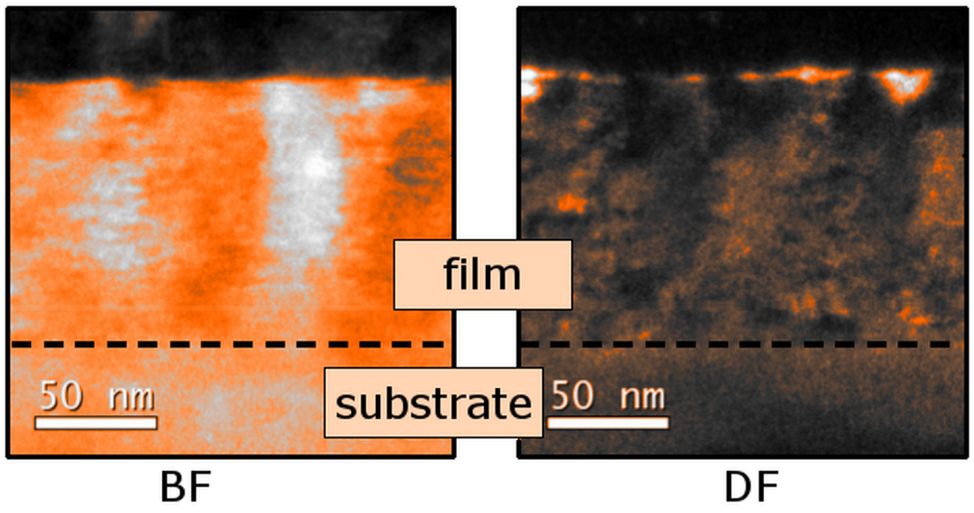

Figure 5.6: TEM images of STO thin film. - The bright field (BF) and dark field (DF) images obtained from the TEM technique, showing large contrast inhomonegeities in 100 nm thick STO film doped with 5 % Fe.

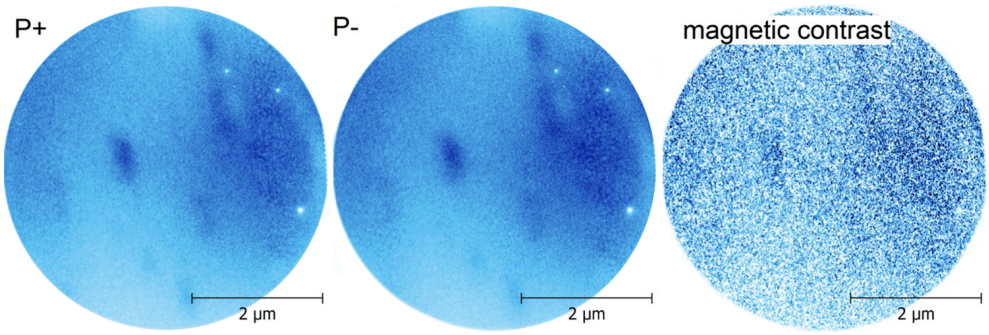

Figure 5.7: XMCD result on the Fe 712,7 eV edge. - The result obtained from the XPEEM equipment localized on the Swiss Light Source synchrotron. The both polarization (P+ and P-) of the incoming X-ray radiation are shown, as well as the their difference (XMCD signal) showing magnetic contrast. The measurement was done on the 5 % Fe doped STO thin film sample.

ration, which significantly reduce the final resolution. Nevertheless an interesting results were obtained on one of the sample - the 5 % iron doped thin film. An XPEEM image performed on the 7.127 keV energy (iron absorption edge) as well as the XMCD (difference between two polarization of the incoming X-rays) signal are presented in the Fig.5.7. Even though no Fe inhomogeneities were found (the ones visible on the P+ and P- image originates from the topography or the work function) a very small magnetic signal was found coming from the 100 nm inhomogeneities. There was no trace of similar results on on other samples. To confirm the presence of the ferromagnetic signal, the macroscopic magnetic measurements were performed using SQUID magnetometer. The results for the sample with the higher doping concentration of 5 % Fe, after substrate signal subtraction, are shown in the Fig.5.8. Very weak ferromagnetic signal can be found.

While the stoichiometric STO is diamagnetic, some instances of the ferromagnetism was reported in the literature(177). No clear explanation for this phenomenon is given, but the impurities or cation vacancies are suggested(178). Other explanation involves a 2D electron gas effects, as some experiments on the $LaAlO_3/SrTiO_3$ interface showed ferromagnetic behavior(179). Yet, in this work the influence of the impurities or cation nonstoichiometry was determined to be very unlikely. The XRF showed no magnetic impurities and XPS showed good cation stoichiometry. Naturally, the Fe can induce ferromagnetism(180), but only when sufficient concentration is reached. It was shown that the ferro-

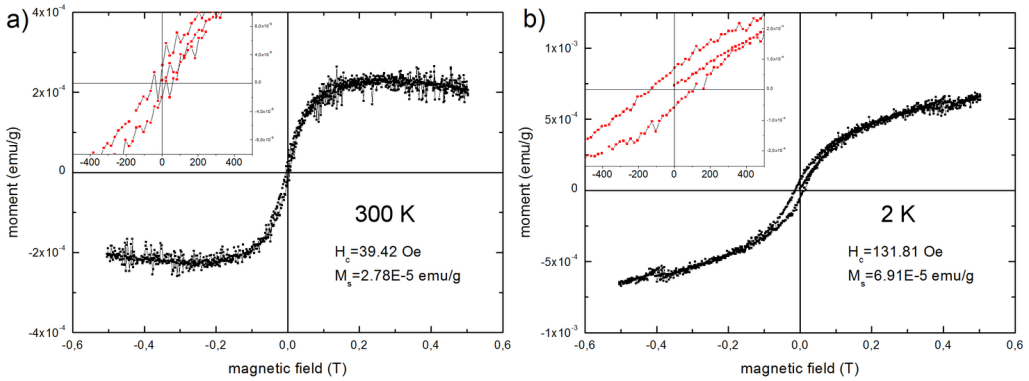

Figure 5.8: Magnetization measurements for the 5 % Fe doped STO thin film. - The magnetization for 5 % Fe doped STO thin film at: a) 300 K and b) 2K. The insets are the magnification of the region for small fields. Clearly visible hysteresis loops shows ferromagnetic interaction even at the room temperature.

magnetic behavior is not longer present in case of 20 % Fe doped epitaxial thin films of STO(181). Off course, this the 20 % limit is true exclusively in the case of homogeneously distributed iron, so one can expect that the nonhomogeneous distribution can significantly lower this limit.

To further confirm the presence of the ferromagnetism and to gather additional information about its source, the Mössbauer spectroscopy on the Fe ions was performed. Typically the MS geometry require significant volume of the material and it is not suitable for the thin films. However a variation of the method - the Conversion Electron Mössbauer Spectroscopy was implemented. In this method the primary gamma radiation interacts with the surface of the material and, due to converstion interaction, the electrons are emitted from the sample. The short mean free path of the electrons in solids give surface sensitivity (top 10 nm of the material). The result of a CEMS experiment performed on the higher doped sample (5 % Fe) is presented in the Fig.5.9. The numerical fitting was performed giving 3 separate components, which are summarized in the Tab.5.2. The components are described by 3 major parameters, and according to the results they were attributed to the various oxidation states. The relative area i.e. the ration of the components is also present. The three mentioned parameters are: isomer shift (δ), quadrupole splitting (ΔE_Q) and the magnetic hyperfine field (B_{hf}). The isomer shift is used primarily for the determination of the ion valency state but also for the ligand bonding state, electron shielding and

the electron-drawing power of electronegative groups. Typically the comparative study is done, as there is substantial literature on the iron MS. The quadrupole splitting comes from the interaction between non-spherical charge distribution of a nucleus (in this case Fe) and the asymmetrical electric field produced by an asymmetric electronic charge distribution or ligand arrangement. Thus, the quadrupole splitting gives information about local geometry and in the case of symmetrical distribution its value should be close to zero. The last parameter, the magnetic hyperfine field comes from the interaction of the nuclear spin moment with the magnetic field (Zeeman splitting). This parameter is directly related to the magnetism and magnetic interaction, and should vanish in the case of no long-range interactions. Thus the observed lines are related to:

- double line - a doublet suggests that the local symmetry of the iron ions is not cubic like in the case of Fe^{4+}. The isomer shift fits well with the values for the Fe^{3+}(182),

- single line - there is no splitting, thus the local symmetry is cubic, the isomer shift is close to 0, which fits well with the Fe^{4+} case(182),

- sextet - line formed of broad distribution of the magnetic filed, with the average field of 23.3 T (for the comparison B_{hf} for ferromagnetic α-Fe is equal to 33.3 T), the isomer shift suggest that this component stems from the Fe^{4+}.

The existence of the magnetic component confirms previous results, however even in the long measurement period the statistic of the measurement is not sufficient to perform full analysis. Nevertheless the source for the magnetic interaction can be from either vibronic Fe^{4+} O^{2-} Fe^{4+} or polaronic Fe^{4+} O^{2-} Fe^{3+}. Additionally the contribution from the antiferromagnetic Fe^{3+} O^{2-} Fe^{3+} virtual superexchange can not be excluded. Thus some remarks has to be given concerning the iron homogeneity.

As a summary, no direct evidence was found for the iron agglomeration. Nevertheless, the resolution of all available techniques were well above 50 nm, which is probably not sufficient to detect small agglomerates. However, the magnetic measurement strongly suggest, that the agglomeration of the Fe has to take place.

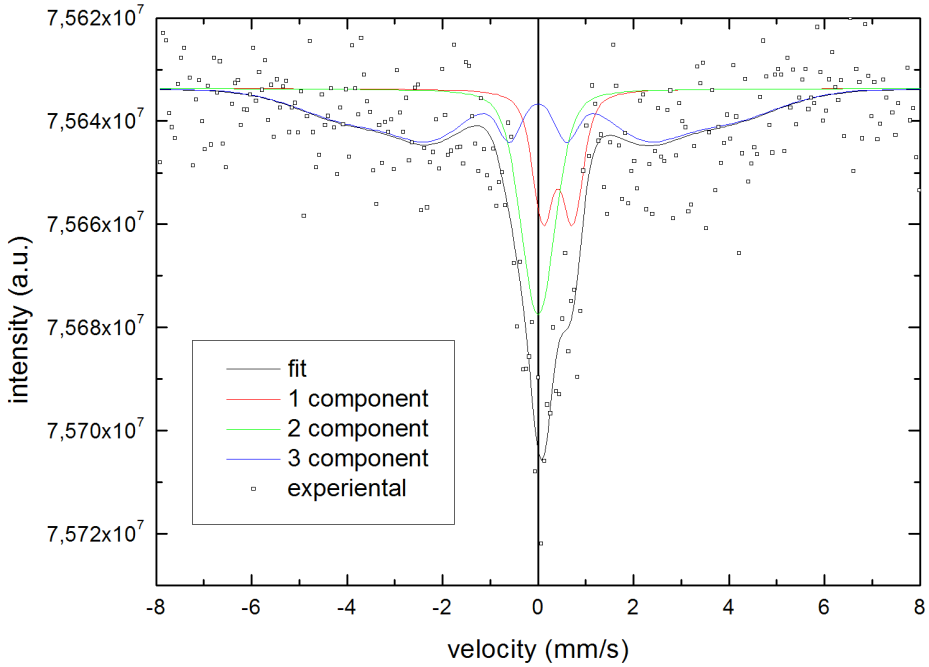

Figure 5.9: MS results for the 5 % Fe doped STO thin film. - The results for 5 % Fe doped STO thin film at room temperature is presented. The data was fitted using three components - one coming from the Fe^{3+} paramagnetic component and two from the Fe^{4+}.

Component	δ mm/s^{-1}	ΔE_Q mm/s^{-1}	B_{hf} T	oxidation state	area %
double line	0.42	0.62	-	Fe^{3+}	21
single line	-0.1	-	-	Fe^{4+}	28
sextet	-0.1	-	23.3	Fe^{4+}	51

Table 5.2: Mössbauer parameters for the 5 % Fe doped STO thin film. The best fit to the MS data shows three distinctive components. One for the Fe^{3+} and two for Fe^{4+}. One of the components shows sextet splitting, which is possible only in the presence of the magnetic interactions.

5.5 AFM measurements

In order to detect the RS behavior in the nanosclae, the LC-AFM technique was implemented. The sample topography was carefully studied, but the main focus was put on the local electrical behavior. In general, as-received thin film samples exhibited flat surface with barely visible terraces originating from the substrate. The substrate were prepared prior to thin film evaporation in high temperature and ambient atmosphere yielding flat single terminated surface with mono-atomic steps. The deposited films shows very grainy morphology suggesting a 3D growth of the film.

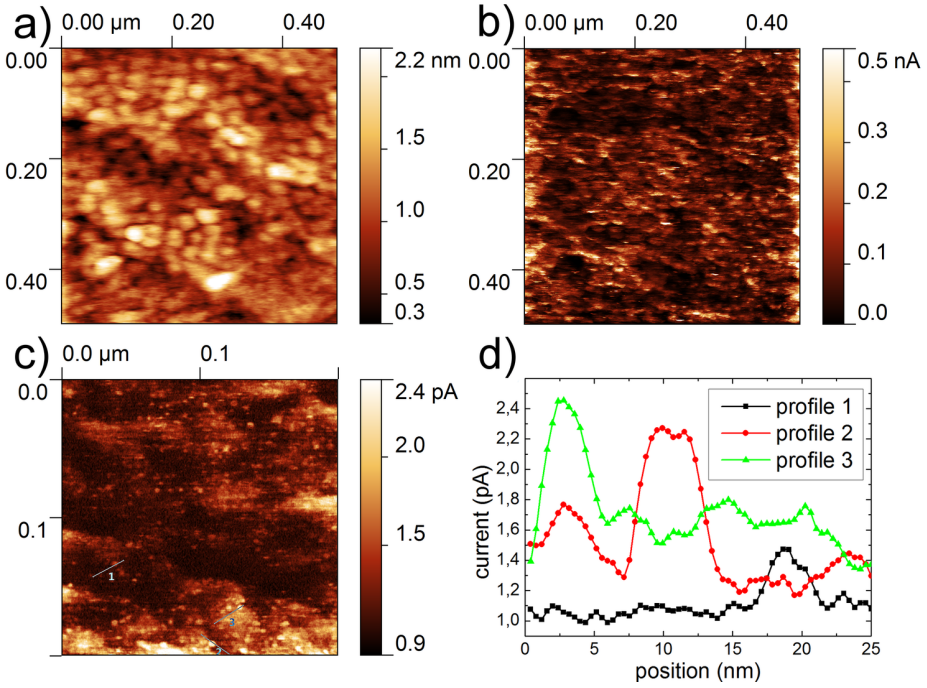

Figure 5.10: AFM investigation of 0 % Fe doped STO thin film. - 0 % Fe doped (reference) sample of thin film of STO obtained from LC-AFM measurements: a) topography, b) local current, c) small scale local current measurement and d) the profiles of conductive spots.

The average grains height are in the range of 1.0 - 1.2 Å. The RMS parameter typically used to quantify the surface roughness(183) was found to be in the range of 2 - 5 Ådepending slightly on the sample and on the preparation procedure. Additionally, one can notice 20 - 30 nm islands elevated above the surface by several nm. Their appearance depends strongly on the sample history, for example the

samples measured shortly after production were relatively free of them, whereas the samples measured over the period of weeks (or months) exhibited a large quantity of islands. The same effect was also spotted when the samples experienced reapeting cycles of UHV heating (up to 300 °C). Similar islands or droplets were found in lightly reduced and rapidly cooled single crystal STO, which was attributed to the formation of amorphous SrO on the surface(149).

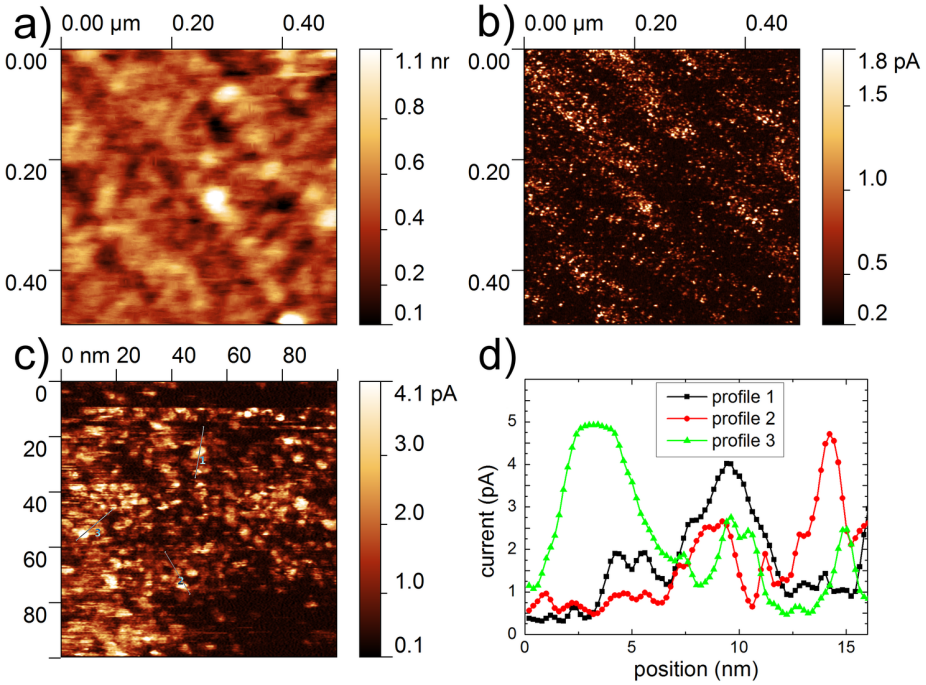

Figure 5.11: AFM investigation of 1 % Fe doped STO thin film. - 1 % Fe doped sample of thin film of $SrTiO_3$ obtained from LC-AFM measurements: a) topography, b) local current, c) small scale local current measurement and d) the profiles of conductive spots.

Moreover, the local conductivity measurements revealed that those islands are insulating, which is consistent with the electrical properties of SrO(184). The electrical measurements using conducting tip showed very inhomogeneous surface resistance. A number of well conducting spots in the weakly conducting matrix were found. It was already shown that the well conducting spots are the exist of filaments, formed of extended defects allowing for enhanced oxygen vacancy transfer. They are the intrinsic property of the material, and are typically just a few nanometers in diameter. Singular spot can be individually addressed and switched resistively by the AFM tip(12). Such filamentary conductivity can be

found in many binary and ternary oxides(185, 186) and in general is considered surface rather than bulk related(12, 187). The detailed comparison between the the topography and the conducting spots was made in order to rule out any artifacts connected with the tip-sample interaction. The results shows that the correlation was very low. Typical topography and local resistivity map can be found in the Fig.5.10 - 5.13. The average densities of the conducting spots ranged from $5{\cdot}10^{10}$ to $3{\cdot}10^{11}$ dots/cm^2. The average size of the conducting spots was found to be several nm, however the distribution was very large, which was surely heavily influenced by tip geometry and coating deterioration. Nevertheless, obtained densities were consistent with the densities obtained for other systems, like the STO thin films grown on $SrRuO_3$ substrate(99). The statistical information are summarized in the Tab.5.3.

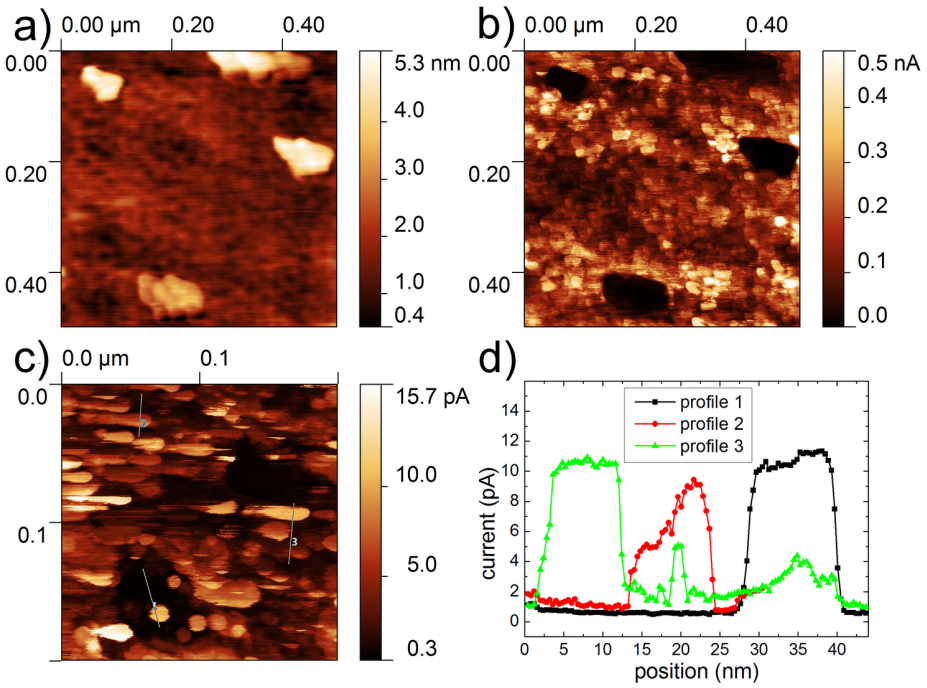

Figure 5.12: AFM investigation of 2 % Fe doped STO thin film. - 2 % Fe doped sample of thin film of $SrTiO_3$ obtained from LC-AFM measurements: a) topography, b) local current, c) small scale local current measurement and d) the profiles of conductive spots.

It is worth mentioning, that the topography and the local resistivity map of 5% Fe doped sample are slightly different from the samples with smaller iron concentrations. First, no amorphous, non-conducting SrO islands were found, and

Sample	RMS (nm)	density of conducting spots ($1/cm^2$)
0 % Fe	0.3	$5.8{\cdot}10^{10}$
1 % Fe	0.5	$9.5{\cdot}10^{10}$
2 % Fe	0.2	$1.29{\cdot}10^{11}$
5 % Fe	0.3	$2.44{\cdot}10^{11}$

Table 5.3: Statistical data on the LC-AFM data of thin films. Statistical data for the both topographical and electrical measurements performed for all investigated samples of $SrTiO_3$ thin films doped with iron. The uncertainties are: RMS = 0.2 nm and density = $1{\cdot}10^{11}$ $1/cm^2$.

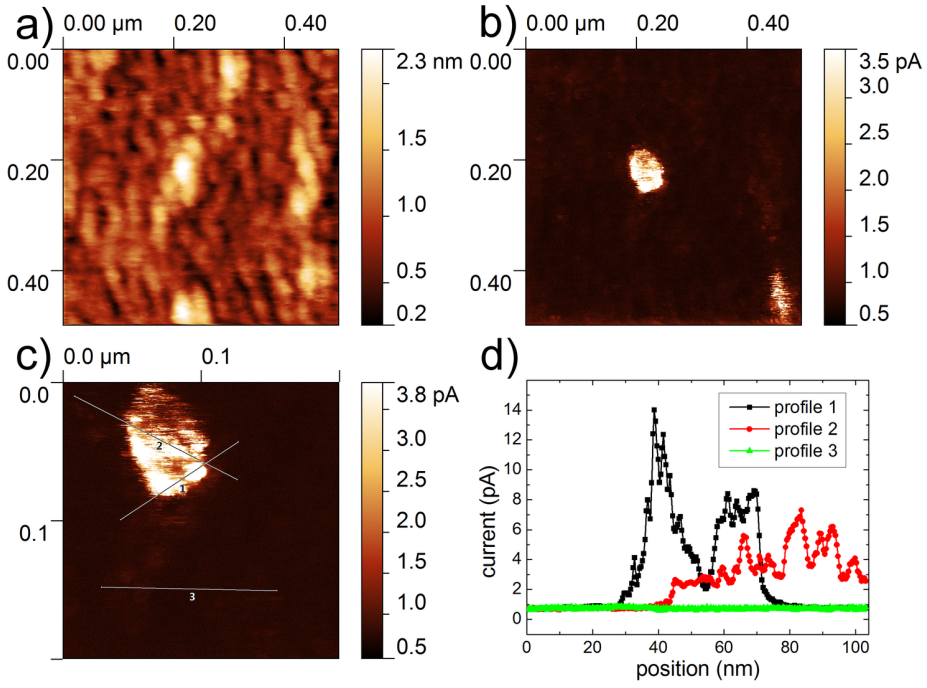

Figure 5.13: AFM investigation of 5 % Fe doped STO thin film. - 5 % Fe doped ample of thin film of $SrTiO_3$ obtained from LC-AFM measurements: a) topography, b) local current, c) small scale local current measurement and d) the profiles of conductive spots.

second the local conductivity looks qualitatively different. We found a number of relatively large - typically 40 - 80 nm well conducting areas, as can be seen in the Fig.5.13 b) and c). Further investigation revealed that they are formed of previously observed well conducting spots. One could link the presence of the well conducting areas with the iron inhomogeneity deducted from other experiments, but the direct correlation was not possible. Nevertheless, the ability to decorate the defects and extended defects by iron observed in the single crystals investigation can suggest that there are strong relation between the well conducting regions and the iron agglomeration. We did not observe the same effect for lower iron concentration, which could indicate concentration threshold of 5 %. This threshold however, may only be related to the observation of conducting areas on the surface, not the actual limit, above which the iron starts to agglomerate.

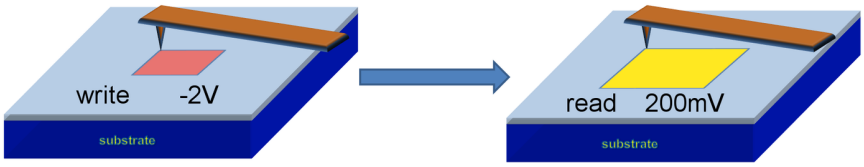

Figure 5.14: Schematic of the area RS experiment. - The schematic representation of the first type RS experiment including LC-AFM, where the surface is first switched by the higher voltage and then scanned using much lower voltage.

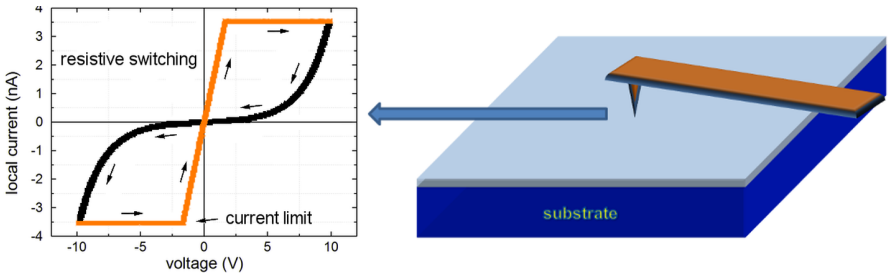

Figure 5.15: Schematic of the current-voltage RS experiment. - The schematic representation of the second type RS experiment including LC-AFM, where the current-voltage characteristic are gathered in a specific points on the sample surface.

In order to investigate the RS behavior of the thin films two types of experiments were performed:

- First was focused on the investigation of the surface RS. The polarized tip of the LC-AFM was used to scan certain area with sufficiently high voltage (write) and next the same region was scanned with much lower voltage (read) - schematically presented in the Fig.5.14. Thus, the changes in the conductivity before and after each scan as well as any changes in the topography could be detected.

- Second type o experiment was more local, the LC-AFM tip was set in one point and then voltage sweeps were done (I-V curves). This allowed to measure the response of the thin films very locally and detect the resistive switching in direct way - schematically presented in Fig.5.15.

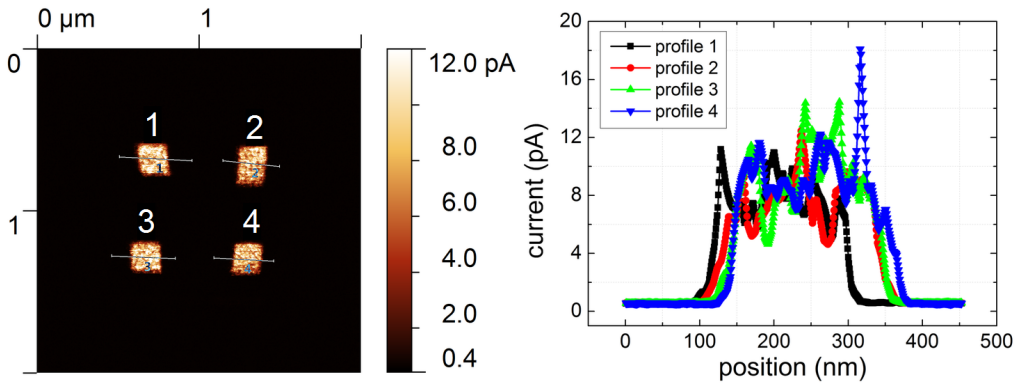

Figure 5.16: Surface RS experiment performed on the 2% Fe doped STO thin film. - The results show a local conductivity image recorded with the 200 mV bias by the LC-AFM after switching four regions with the higher negative voltage of -2 V (left). The profiles of the switched regions are also presented (right).

One has to keep in mind, that the sufficiently high currents flowing through the conducting tip can damage the tip. This current density limit is tip-dependent, and typically ranges from 10^7 to 10^8 A/cm^2. For this reason (among other), all commercial AFM are equipped in the current compliance features. In the case of data presented in this chapter the limiting current was equal to 333 nA, which is considered a safe value. The results from the first type of experiment are presented in the Fig.5.16, while all investigated samples exhibited very similar behavior. The presented image shows local resistance map in 2 $\times$ 2 μm region with 200 mV bias. The four region in the center was previously scanned with -2 V bias and then presented image was recorded. The current measured in the dark,

non-conducting region was equal to 0.56 pA, which is very close to the smallest current that can be measured by using applied LC-AFM setup. Therefore, it was not possible to determine the real value of current flowing trough the sample. By analyzing the profiles of the switched regions one can notice two features: the increase of the current flowing trough those regions and fact, that all regions exhibits very similar conductivity. The resistance of the switched regions decreased by the factor of 20 (lowest value).

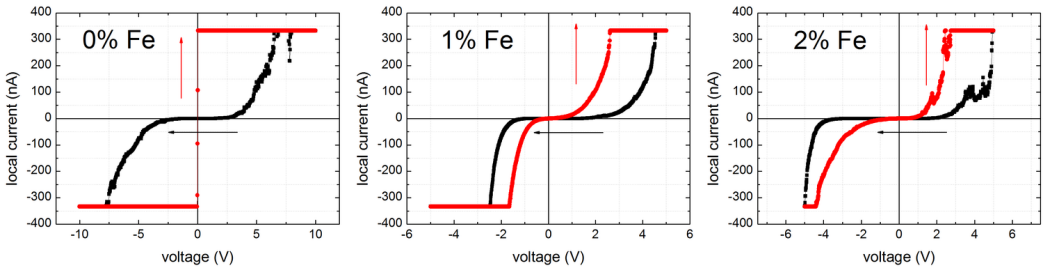

Figure 5.17: IV curves for the series of Fe doped STO thin films. - The chosen current-voltage characteristics recorded with the use of conducting tip and the LC-AFM equipment. The presented results are typical for the 0 % (left), 1 % (middle) and 2 % (right) Fe doped samples. The RS is clearly visible.

The results from the second type of experiment in a form of several chosen I-V curves are presented in the Fig.5.17. One can clearly recognize the RS behavior. The arrows points out the direction of the voltage sweeps. The origin of the RS behavior in thin films is identical to these in the single crystals: the negatively polarized tip repels the oxygen ions, which travels further from the surface. The oxygen vacancy concentration increases leading to the I-M transition. During this process the resistance of the material decreases significantly, and material transfer to metallic state - like in case of the 0 % Fe doped sample presented in the Fig.5.17. If the polarization of the tip is changed to positive, the oxygen ions are attracted and the metallic state is destroyed(12). The separate electroformation step was not necessary, since the first voltage sweep was sufficient to induce RS behavior. This could be due to the fact, that the thin film material consist of a much larger defect concentration that the single crystals, thus the oxygen vacancy concentration is high from the beginning. From this reason, even relatively small voltage was sufficient to produce RS response.

5.6 Activation energy

With respect to a deeper understanding of the current transport mechanisms the electrical temperature measurements using the LC-AFM was performed. For every 50 °C from the room temperature to 200 °C several (typically 5) local resistance maps with the size of 500 nm × 500 nm were made. Then the resistance was calculated and plotted against temperature and fitted to the Arrhenius formula:

$$R = \frac{R_0}{T} \cdot exp\left(\frac{-E_a}{k_B T}\right) \tag{5.1}$$

The resulting activation energies are showed in the Fig.5.18 and Tab.5.4. Higher iron concentration tends to decrease the activation energy, although the changes are rather small. Qualitatively, the obtained values are in good agreement with the XPS measurements(83), which yielded a band gap of approximately 0.4 eV for iron doped thin films and an increase in the density of states in-gap with the iron concentration. Nevertheless, the obtained values are significantly lower that those of the single crystals reported in this work. One can find a number of different values reported in the literature, starting from 0.3 eV(31) to 1.3 eV(188).

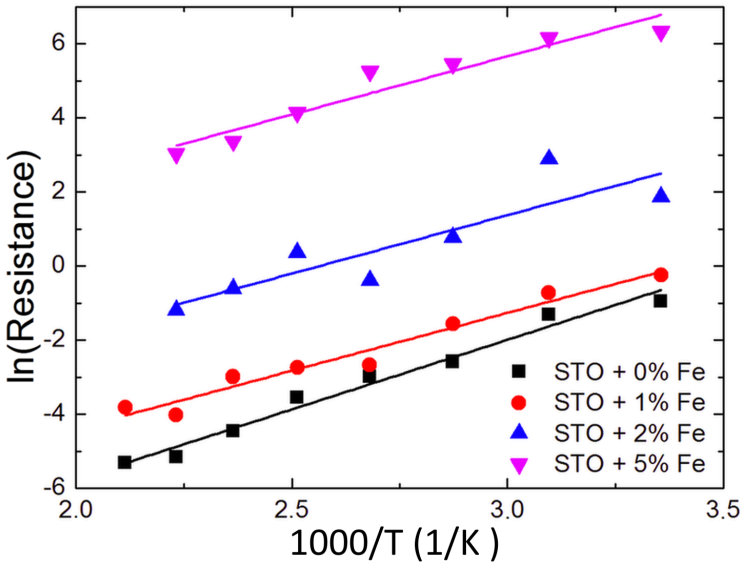

Figure 5.18: Activation energy measured for the Fe doped STO thin films. - LC-AFM temperature measurements for series of thin films of Fe doped $SrTiO_3$.

Sample	activation energy (eV)
0 % Fe	0.32
1 % Fe	0.27
2 % Fe	0.26
5 % Fe	0.25

Table 5.4: Activation energy obtained from the LC-AFM data on Fe doped STO thin films. The results from the best linear fit to the Arhenius plot for the electrical measurement of Fe doped STO thin films.

The easiest explanation for such variations in reported values can be the complex character of the STO surface, different preparation methods and the thermal history of the samples. However, further investigation performed in this work showed completely different mechanism, that is directly connected with the RS phenomena. During the previous experiment, the threshold voltage for the 'on' and 'off' state was found to be close to 5 volts, which was slightly influenced by the actual duration of the measurement. Namely, longer voltage pulses decreased the voltage threshold. Thus, the voltage previously considered 'safe' in a sense, that was not sufficient to induce RS transition, could be much lower that previously anticipated. In other words, the resistance of the investigated thin films might change during measurements. This would have substantial influence on the activation energy values.

In order to confirm those concerns, a number of experiment were performed. Completely new set of experimental data was gathered, by adding the voltage dependence on the typical LC-AFM resistance map versus temperature measurements. Thus, for each temperature step a set of I-V curves ranging from ± 0.5 V each in a raster of 100×100 points in the 500 nm $\times$ 500 nm region was measured. Again, at least 5 different region on the sample surface was investigated. Consequently, for each voltage, an activation energy was calculated and plotted versus voltage in Fig.5.19. What is more, a two plots were made - in the upper one only the data from selected 20 most conducting spots in each LC-AFM image was taken into the calculation, while in the bottom whole image was averaged. One can notice that there are some differences, which shows that the conducting spots behave differently than the 'matrix', which points out that they are different in the origin. One could assume that the activation energy should not be on the

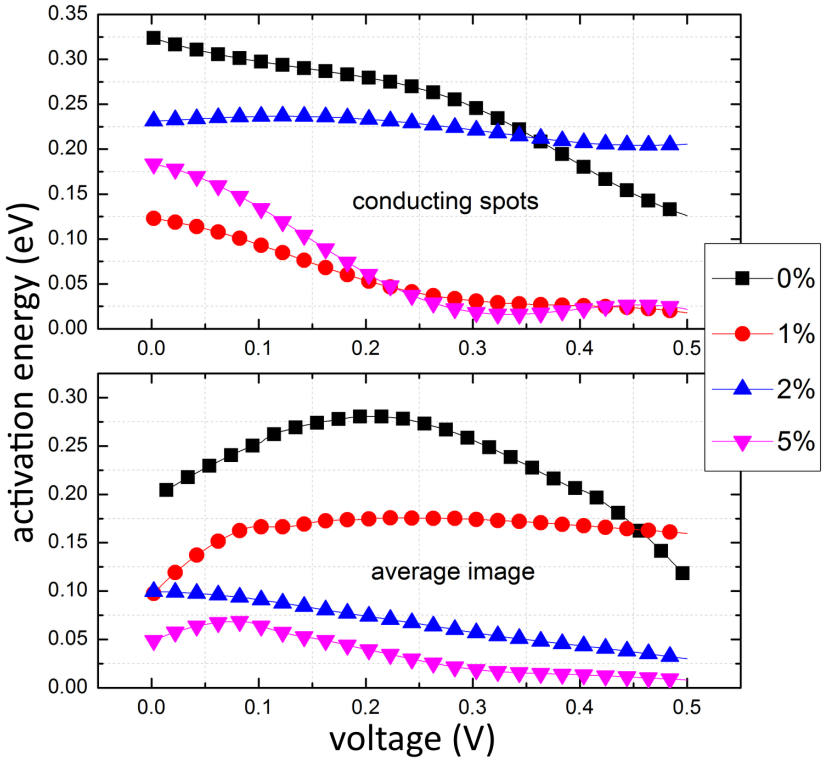

Figure 5.19: Activation energy versus voltage in Fe doped STO thin films. - The results obtained from LC-AFM temperature measurements for series of thin films of STO doped with iron showing a clear dependency on the applied voltage.

voltage. Nevertheless, in the case all investigated thin films, the dependency on the voltage is significant. Even the smallest applied voltage of 20 mV lead to the electrical modification of the surface during measurements. This could explain the difficulties in obtaining the real value of the activation energy for the STO thin films.

5.7 Conclusions

This chapter consist of the measurements on Fe-doped (0, 1, 2 and 5 % *at*) STO thin films. Good crystallographic structure was confirmed by XRD and LEED measurements. The element distribution obtained from the TOF-SIMS measurement (worse than 100 nm resolution) was shown to be homogeneous, both in

micro- and nano-scales. Nevertheless, several techniques indicated the possibility of iron agglomeration into regions of around 50 nm and less. The magnetic measurements clearly showed the existence of ferromagnetic contribution, that would be very unlikely in the case of random Fe distribution. The TOF-SIMS depth profiles showed iron and niobium migration, either during the preparation process or later during thermal treatment.

The topography and local conductivity experiment revealed generally flat surface with the RMS parameter below 0.5 nm. Local resistivity maps showed very inhomogeneous surface conductivity in form of very well conducting spots. The conducting regions were attributed to, already observed in the single crystals, exits of the extended defects network. Moreover, the temperature measurements allowed to calculate the activation energy, which was directly correlated with the oxygen vacancy migration. Unfortunately, it was discovered, that even the smallest applied voltage was sufficient to change the resistivity of the measured thin films, which resulted in the clear dependence of the activation energy on the applied voltage.

What can be considered a success, is that many features are very similar to those found in the single crystals, especially the RS behavior. The RS behavior was clearly observed, both as a typical I-V curves and as permanently switched surface area. This shows, that the thin films of Fe doped STO can be successfully used in the future RRAM applications. Nevertheless, one has to keep in mind that the obtained data can be influenced by the behavior of the thin film substrate.

6

Summary

The main objective of this work was to identify and understand the physical mechanisms underlying the phenomenon of the RS in the Fe doped $SrTiO_3$ material. Two basic types of materials were investigated: the single crystals and thin films. The main reason for this approach was to obtain the information about both: the fundamental physics (single crystals) and the material more suited for the applications (thin films). The samples with different iron concentrations, were modified by the temperature, electric field and chemical gradients. Resulting changes were investigated by a number of techniques that are characteristic to the solid state physics in the macro- and nano- scales.

Completed studies have shown that:

- Crystallographic structure of the starting crystals was in good agreement with the literature.
- Surprisingly high level of the Fe concentration variation, even for the relatively low Fe doping, was found.
- Local conductivity in nanoscale showed characteristic conducting stripes, not observed previously.
- Fe valence state was found to be a mixture of 2+ and 3+, contrary to the most of the reports on similar systems.
- Moderately high temperature treatment under oxidizing and reducing conditions led to huge chemical modification of the crystal surface, including formation of new phases and the decomposition of STO phase.

- High mobility of the Fe ions above 700 °C allowed for significant iron migration and preferential atoms localization (close to the extended defects).

Especially interesting is that the crystals exposed to the high temperature under various conditions undergone transformation and decomposition to other phases. This remains in the contrary to conventional model, where only the oxygen content in the form of $SrTiO_{3-\delta}$ was changing. Moreover, the affinity of the Fe ions to locate close to the extended defects was shown, as an formation of filament like Fe structure. The nanoscale RS behavior was also evident and did not differ significantly from the behavior in the undoped STO crystals. It was concluded, that the basic mechanism of RS in Fe doped STO is not influenced by the iron doping.

Similar results can be observed under the electrical stress. The electroformation and subsequent electro-coloration phenomena were investigated. The most prominent results showed:

- Electrical stimuli led to the I-M transition.
- I-M transition was connected to changes in the oxygen vacancy concentration and the movement of the oxigen ions along the extended defect network.
- Evolution of the color front was documented, and compared to the removal of oxygen ions from the material.
- Total number of the oxygen ions removed from the material during electroreduction experiment was estimated.
- RS behavior was found and measured both in macro- and nano-scales.
- Fast reaction of the electrical behavior to the surrounding atmosphere confirmed, that the oxygen can be removed and introduced to the system quite easily.

Strong connection between the evolution of the color front and the electrical properties of the samples were shown. Also the fact that the Fe doped STO crystal is in fact 'open' to the removal and introduction of the oxygen ions from the surrounding atmosphere was found.

The investigation of the thin films yielded promising results, especially in the similarities with the single crystal behavior. The most interesting findings consist of:

- Many hints that the Fe ions were inhomogeneously distributed in the STO matrix was found.
- Fe was found to be very mobile and typically was found to migrate away from the surface into the bulk.
- High susceptibility of the electrical parameters to the electrical stress led to high variation in the measured activation energy values.
- The RS behavior was confirmed and no clear voltage threshold for the set and reset voltage was found (up to several mV).

This results showed many similarities of the STO thin film and single crystals behavior. It seems possible to maintain good single crystal properties in more applicative thin films. What is more, the pursue for the 'perfect' or defect-free thin films is not always necessary, since it can be beneficial for the RS materials to posses slightly different structure or defect concentration. Nevertheless, there is still a long way from the basic investigations and prototypes to the commercial applications. It is also important to be more careful measuring the electrical properties of the RS material, since the properties of the investigated material can change during the experiment itself, leading to unreliable results.

Outlook

Investigation presented in this work showed that the RS is complicated phenomena. The complexity of the RS even increases, when one moves his attention from the macroscale, typically used to describe the properties of the materials, into nanoscale. In many cases, only the nanoscale experiments can provide crucial data necessary for better understanding of the fundamental physics. What is more, the observations in nano-scale clearly shows that the perfect crystals are really not so perfect as one could expect, which is strongly connected to structure defects and inhomogeneity of the dopant. The knowledge of the imperfection and the real state of the materials is not only useful from the fundamental point of view. I strongly believe it is necessary for the future investigation and the development of new technologies. As the case of the STO (and the Fe doped STO) shows, the extended defects, such as dislocations, are crucial for the RS behavior.

Therefore a careful investigations, mostly in nanoscale, can provides the ideas and the means to exploit the defects and imperfections for the benefit of new materials with outstanding properties.

Bibliography

[1] N. Setter and R. Waser. **Electroceramic materials**. *Acta Materialia*, **48**(1):151–178, January 2000. 1

[2] G. D. Wilk, R. M. Wallace, and J. M. Anthony. **High-κ gate dielectrics: Current status and materials properties considerations**. *Journal of Applied Physics*, **89**(10):5243, 2001. 1

[3] C Tragut and KH Härdtl. **Kinetic behaviour of resistive oxygen sensors**. *Sensors and Actuators B: Chemical*, **4**:425–429, 1991. 1

[4] OA Marina, NL Canfield, and JW Stevenson. **Thermal, electrical, and electrocatalytical properties of lanthanum-doped strontium titanate**. *Solid State Ionics*, **149**:21–28, 2002. 1

[5] H. Hilgenkamp and J. Mannhart. **Superconducting and normal-state properties of YBa[sub 2]Cu[sub 3]O[sub 7δ] -bicrystal grain boundary junctions in thin films**. *Applied Physics Letters*, **73**(2):265, 1998. 1

[6] R. Waser, Regina Dittmann, Georgi Staikov, and K. Szot. **Redox-Based Resistive Switching Memories - Nanoionic Mechanisms, Prospects, and Challenges**. *Advanced Materials*, **21**(25-26):2632–2663, July 2009. 2, 20, 22, 30, 31, 37, 39, 83, 99

[7] W. R. Hiatt and T. W. Hickmott. **Bistable Switching in Niobium Oxide Diodes**. *Applied Physics Letters*, **6**(6):106, 1965. 2

[8] K. L. Chopra. **Avalanche-Induced Negative Resistance in Thin Oxide Films**. *Journal of Applied Physics*, **36**(1):184, 1965. 2

[9] F Argall. **Switching phenomena in titanium oxide thin films**. *Solid-State Electronics*, **11**:535–541, 1968. 2

[10] J.F. Gibbons and W.E. Beadle. **Switching properties of thin Nio films**. *Solid-State Electronics*, **7**(11):785–790, November 1964. 2, 38

[11] Akihito Sawa. **Resistive switching in transition metal oxides**. *Materials Today*, **11**(6):28–36, 2008. 2, 40, 115

[12] K. Szot, Wolfgang Speier, Gustav Bihlmayer, and R. Waser. **Switching the electrical resistance of individual dislocations in single-crystalline SrTiO3.** *Nature materials*, **5**(4):312–20, April 2006. 2, 9, 40, 42, 43, 44, 61, 83, 87, 98, 99, 105, 111, 129, 130, 134

[13] a. Beck, J. G. Bednorz, Ch. Gerber, C. Rossel, and D. Widmer. **Reproducible switching effect in thin oxide films for memory applications**. *Applied Physics Letters*, **77**(1):139, 2000. 2

[14] C. Rodenbucher, W Speier, G Bihlmayer, U Breuer, R. Waser, and K. Szot. **Cluster-like resistive switching of SrTiO 3 :Nb surface layers**. *New Journal of Physics*, **15**(10):103017, October 2013. 2, 84, 115

[15] T. Menke, R. Dittmann, P. Meuffels, K. Szot, and R. Waser. **Impact of the electroforming process on the device stability of epitaxial Fe-doped SrTiO[sub 3] resistive switching cells**. *Journal of Applied Physics*, **106**(11):114507, 2009. 2, 83

[16] J W Anthony. *Handbook of mineralogy*. Number t. 1;t. 3;t. 5 in Handbook of Mineralogy. Mineral Data Publishing, 1990. 4

[17] H R Wenk and A Bulakh. *Minerals: Their Constitution and Origin*. Cambridge University Press, 2004. 4

[18] R. Merkle and J Maier. **How is oxygen incorporated into oxides? A comprehensive kinetic study of a simple solid-state reaction with SrTiO3 as a model material.** *Angewandte Chemie (International ed. in English)*, **47**(21):3874–94, January 2008. 4, 13, 14

[19] Ye. I. Vorob'yev, A A Konev, Yu V Malyshonok, G F Afonina, and A. N. Sapozhnikov. **TAUSONITE, SrTiO3 , A NEW MINERAL OF THE PEROVSKITE GROUP**. *International Geology Review*, **26**(4):462–465, April 1984. 4

[20] E M Levin, R S Roth, C R Robbins, H F McMurdie, and American Ceramic Society. *Phase diagrams for ceramists*. Phase Diagrams for Ceramists. American Ceramic Society, 1983. 4

[21] W D Kingery, H K Bowen, and D R Uhlmann. *Introduction to ceramics*. Wiley series on the science and technology of materials. Wiley, 1976. 6

[22] P M Woodward. **Octahedral Tilting in Perovskites. I. Geometrical Considerations**. *Acta Crystallographica Section B*, **53**(1):32–43, 1997. 6

[23] KA Muller and H. Burkard. **SrTiO3 An intrinsic quantum paraelectric below 4 K**. *Physical Review B*, **19**(7):3593–3602, 1979. 7

[24] Behnaz Rahmati Kalkhoran. *Microstructural Studies on the Reoxidation Behavior of Nb-doped SrTiO3 Ceramics*. PhD thesis, Universität Stuttgart, 2004. 7

[25] Lixin Cao, E Sozontov, and J Zegenhagen. **Cubic to Tetragonal Phase Transition of SrTiO3 under Epitaxial Stress: An X-Ray Backscattering Study**. *physica status solidi (a)*, **387**(181):387–404, 2000. 7

BIBLIOGRAPHY

[26] CS Koonce, ML Cohen, JF Schooley, WR Hosler, and DC Pfeiffer. **Superconducting Transition Temperatures of Semiconducting SrTiO_3**. *Physical Review*, **163**(2), 1967. 7

[27] ON Tufte and PW Chapman. **Electron mobility in semiconducting strontium titanate**. *Physical Review*, **442**(1964):4–10, 1967. 7

[28] K. Szot, W. Speier, R. Carius, U. Zastrow, and W. Beyer. **Localized Metallic Conductivity and Self-Healing during Thermal Reduction of SrTiO3**. *Physical Review Letters*, **88**(7):2–5, February 2002. 7, 17, 21, 27, 84, 99, 106

[29] Joachim Maier. *Physical Chemistry of Ionic Materials*. John Wiley & Sons, Ltd, Chichester, UK, April 2004. 8

[30] D M Smyth. *The Defect Chemistry of Metal Oxides*. Classic dielectric science book series. Oxford University Press, 2000. 8

[31] LC Walters and RE Grace. **Formation of point defects in strontium titanate**. *Journal of Physics and Chemistry of Solids*, **28**:239–244, 1967. 8, 135

[32] N. H. Chan, R.K. SHARMA, and D.M. SMYTH. **Nonstoichiometry in Undoped BaTiO3**. *Journal of the American Ceramic Society*, **64**(9):556–562, September 1981. 8, 9

[33] Tudor Baiatu, R. Waser, and Karl-Heinz Hardt. **dc Electrical Degradation of PerovskiteType Titanates: III, A Model of the Mechanism**. *J. Am. Ceram. Soc.*, **73**(6):1663–1673, 1990. 8, 41, 100

[34] L A Bursill and B G Hyde. **On the aggregation of wadsley defects in slightly reduced rutile**. *Philosophical Magazine*, **23**(181):3–15, 1971. 8

[35] F A Kroger and H J Vink. **Relations Between The Concentrations Of Imperfections In Crystalline Solids**. *Solid State Physics*, **3**:307–435, 1956. 8

[36] R Moos and KH Hardtl. **Defect Chemistry of Donor-Doped and Undoped Strontium Titanate Ceramics between 1000 and 1400 C**. *Journal of the American Ceramic Society*, **62**:2549–2562, 1997. 9

[37] Roger A De Souza. **The formation of equilibrium space-charge zones at grain boundaries in the perovskite oxide SrTiO3.** *Physical chemistry chemical physics : PCCP*, **11**(43):9939–69, November 2009. 9

[38] R Meyer, R. Waser, Julia Helmbold, and G Borchardt. **Cationic surface segregation in donor-doped SrTiO3 under oxidizing conditions**. *Journal of electroceramics*, **9**(1):101–110, 2002. 9

[39] N. H. Chan, R.K. Sharma, and D M Smyth. **Nonstoichiometry in SrTiO[sub 3]**. *Journal of The Electrochemical Society*, **128**(8):1762, 1981. 9, 39

[40] J Seidel, W Luo, S J Suresha, P-K Nguyen, a S Lee, S-Y Kim, C-H Yang, S J Pennycook, S T Pantelides, J F Scott, and R Ramesh. **Prominent electrochromism through vacancy-order melting in a complex oxide.** *Nature communications*, **3**:799, January 2012. 9, 16, 18, 30

[41] S Blügel. *Electronic Oxides - Correlation Phenomena, Exotic Phases and Novel Functionalities*. Lecture manuscripts of the ... Spring School of the Institute of Solid State Research. Forschungszentrum, Zentralbibliothek, 2010. 9

[42] J. G. R. Briggs. *Level Course in Chemistry*. Pearson Education South Asia, 2002. 12

[43] AE Bocquet, A Fujimori, T. Mizokawa, T. Saitoh, H. Namatame, S. Suga, N Kimizuka, Y. Takeda, and M. Takano. **Electronic structure of SrFe4+O3 and related Fe perovskite oxides**. *Physical Review B*, **45**(4):1561, 1992. 12, 86

[44] B L Gries. *Single Crystal Growth and Characterization of Ilmenite, FeTiO3, for Electronic Applications*. Texas A & M University, 1988. 12

[45] B. Faughnan. **Photochromism in Transition-Metal-Doped SrTiO_{3}**. *Physical Review B*, **4**(10):3623–3636, November 1971. 12, 85, 103

[46] Ch. Lenser, Aleksandr Kalinko, A. Kuzmin, Dzintars Berzins, J. Purans, K. Szot, R. Waser, and Regina Dittmann. **Spectroscopic study of the electric field induced valence change of Fe-defect centers in SrTiO3.** *Physical chemistry chemical physics : PCCP*, **13**(46):20779–86, December 2011. 12, 85, 103

[47] Ingrid Denk, Wolfram Munch, and Joachim Maier. **Partial Conductivities in SrTiO3: Bulk Polarization Experiments, Oxygen Concentration Cell Measurements, and Defect-Chemical Modeling**. *Journal of the American Ceramic Society*, **78**(12):3265–3272, December 1995. 12

[48] ANA CLÁUDIA LOURENÇO SANTANA MARQUES. *Advanced Si Pad Detector Development and SrTiO_3 Studies by Emission Channeling and Hyperfine Interaction Experiments*. PhD thesis, UNIVERSIDADE DE LISBOA, 2009. 12

[49] RD Shannon. **Revised Effective Ionic Radii and Systematic Studies of Interatomie Distances in Halides and Chaleogenides**. *Acta Crystallographica Section A: Crystal Physics, ...*, **32**:751–767, 1976. 12

[50] O T Sø rensen. *Nonstoichiometric oxides*. Materials science and technology. Academic Press, 1981. 16

[51] Tatsuo Fujii, Hirofumi Oohashi, Tatsunori Tochio, Yoshiaki Ito, Aurel-Mihai Vlaicu, and Sei Fukushim. **Speculations on anomalous chemical states of Ti ions in FeTiO3 observed by high-resolution X-ray Kβ emission spectra**. *Journal of Electron Spectroscopy and Related Phenomena*, **184**(1-2):10–15, February 2011. 17, 26

[52] J P Hirth and J Lothe. *Theory of dislocations*. Wiley, 1982. 17, 20

BIBLIOGRAPHY

[53] William D Callister. *Materials Science and Engineering*. John Wiley & Sons, Inc., 2007. 18

[54] C. Jia, a. Thust, and K. Urban. **Atomic-Scale Analysis of the Oxygen Configuration at a SrTiO3 Dislocation Core**. *Physical Review Letters*, **95**(22):225506, November 2005. 19

[55] LG Harrison. **Influence of dislocations on diffusion kinetics in solids with particular reference to the alkali halides**. *Transactions of the Faraday Society*, pages 1191–1199, 1961. 20

[56] A. D. Le Claire. **The analysis of grain boundary diffusion measurements**. *British Journal of Applied Physics*, **14**(6):351–356, June 1963. 21

[57] Renhui Wang, Yimei Zhu, and SM Shapiro. **Structural Defects and the Origin of the Second Length Scale in SrTiO_ {3}**. *Physical review letters*, **80**(11):2370–2373, 1998. 21, 100, 104

[58] H. Rogalla G. Koster, G. Rijnders, D. H. A. Blank. **Surface morphology determined by (001) single-crystal SrTiO3 termination**. *Physica C: Superconductivity*, **339**:215–230, July 2000. 24

[59] Hans Lüth. *Solid Surfaces, Interfaces and Thin Films*. Graduate Texts in Physics. Springer Berlin Heidelberg, Berlin, Heidelberg, 2010. 24

[60] PW Tasker. **The stability of ionic crystal surfaces**. *Journal of Physics C: Solid State Physics*, **4977**, 1979. 24

[61] C Noguera. *Physics and Chemistry at Oxide Surfaces*. Cambridge University Press, 1996. 24

[62] E. Heifets, R. Eglitis, E A Kotomin, J. Maier, and G. Borstel. **Ab initio modeling of surface structure for SrTiO3 perovskite crystals**. *Physical Review B*, **64**(23):235417, November 2001. 25, 26

[63] R A Evarestov, E A Kotomin, and Yu. F. Zhukovskii. **DFT study of a singleF center in cubic SrTiO3 perovskite**. *International Journal of Quantum Chemistry*, **106**(10):2173–2183, 2006. 26

[64] EA Kotomin, RI Eglitis, J Maier, and E Heifets. **Calculations of the atomic and electronic structure for SrTiO3 perovskite thin films**. *Thin Solid Films*, **400**(1-2):76–80, December 2001. 26

[65] V. E. Alexandrov, E A Kotomin, J. Maier, and R. a. Evarestov. **First-principles study of bulk and surface oxygen vacancies in SrTiO3 crystal**. *The European Physical Journal B*, **72**(1):53–57, October 2009. 26

[66] Vladimir I Anisimov, F Aryasetiawan, and A I Lichtenstein. **First-principles calculations of the electronic structure and spectra of strongly correlated systems: the LDA + U method**. *Journal of Physics: Condensed Matter*, **9**(4):767–808, January 1997. 26

[67] Jochen Heyd, Gustavo E. Scuseria, and Matthias Ernzerhof. **Hybrid functionals based on a screened Coulomb potential**. *The Journal of Chemical Physics*, **118**(18):8207, 2003. 27

[68] Jochen Heyd, Gustavo E. Scuseria, and Matthias Ernzerhof. **Erratum: Hybrid functionals based on a screened Coulomb potential [J. Chem. Phys. 118, 8207 (2003)]**. *The Journal of Chemical Physics*, **124**(21):219906, 2006. 27

[69] Thomas M. Henderson, Joachim Paier, and Gustavo E. Scuseria. **Accurate treatment of solids with the HSE screened hybrid**. *Physica Status Solidi (B)*, **248**(4):767–774, April 2011. 27

[70] Axel D. Becke. **Density-functional thermochemistry. III. The role of exact exchange**. *The Journal of Chemical Physics*, **98**(7):5648, 1993. 27

[71] S Piskunov, E Heifets, R.I Eglitis, and G Borstel. **Bulk properties and electronic structure of SrTiO3, BaTiO3, PbTiO3 perovskites: an ab initio HF/DFT study**. *Computational Materials Science*, **29**(2):165–178, February 2004. 27, 28

[72] D.M. Smyth. **The role of impurities in insulating transition metal oxides**. *Progress in Solid State Chemistry*, **15**(3):145–171, January 1984. 27

[73] S. Piskunov, E.a. Kotomin, E. Heifets, J. Maier, R.I. Eglitis, and G. Borstel. **Hybrid DFT calculations of the atomic and electronic structure for ABO3 perovskite (001) surfaces**. *Surface Science*, **575**(1-2):75–88, January 2005. 29

[74] Yu.F. Zhukovskii, E A Kotomin, S. Piskunov, and D.E. Ellis. **A comparative ab initio study of bulk and surface oxygen vacancies in PbTiO3, PbZrO3 and SrTiO3 perovskites**. *Solid State Communications*, **149**(33-34):1359–1362, 2009. 29, 89

[75] Fedwa El-Mellouhi, Edward N Brothers, Melissa J Lucero, and Gustavo E Scuseria. **Neutral defects in SrTiO3 studied with screened hybrid density functional theory.** *Journal of physics. Condensed matter : an Institute of Physics journal*, **25**(13):135501, April 2013. 29

[76] C L Jia, M Lentzen, and K Urban. **Atomic-resolution imaging of oxygen in perovskite ceramics.** *Science (New York, N.Y.)*, **299**(5608):870–3, February 2003. 30

[77] Stefan Rodewald, Jürgen Fleig, and Joachim Maier. **Microcontact Impedance Spectroscopy at Single Grain Boundaries in Fe-Doped SrTiO 3 Polycrystals**. *Journal of the American Ceramic Society*, **84**(3):521–530, March 2001. 30

[78] M. Vračar, A. Kuzmin, R. Merkle, J. Purans, E A Kotomin, J Maier, and O. Mathon. **Jahn-Teller distortion around Fe4+ in Sr(FexTi1x)O3δ from x-ray absorption spectroscopy, x-ray diffraction, and vibrational spectroscopy**. *Physical Review B*, **76**(17):1–12, 2007. 30, 32

[79] R. Evarestov, S. Piskunov, E A Kotomin, and G. Borstel. **Single impurities in insulators:Ab initio study of Fe-doped SrTiO3**. *Physical Review B*, **67**(6):064101, February 2003. 30

BIBLIOGRAPHY

[80] Xin Zhou, Jingying Shi, and Can Li. **Effect of Metal Doping on Electronic Structure and Visible Light Absorption of SrTiO 3 and NaTaO 3 (Metal = Mn, Fe, and Co)**. *The Journal of Physical Chemistry C*, **115**(16):8305–8311, April 2011. 30

[81] J. B. MacChesney, R. C. Sherwood, and J. F. Potter. **Electric and Magnetic Properties of the Strontium Ferrates**. *The Journal of Chemical Physics*, **43**(6):1907, 1965. 30

[82] V. Alexandrov, J Maier, and R A Evarestov. **Ab initio study of SrFexTi1xO3: Jahn-Teller distortion and electronic structure**. *Physical Review B*, **77**(7):075111, February 2008. 31, 33

[83] J. Szade, K. Szot, M. Kulpa, J. Kubacki, Ch. Lenser, R. Dittmann, and R. Waser. **Electronic structure of epitaxial Fe-doped SrTiO 3 thin films**. *Phase Transitions*, **84**(5-6):489–500, May 2011. 31, 86, 87, 135

[84] R Waser, editor. *Nanotechnology: Volume 3: Information Technology I (Nanotechnology(VCH))*. Wiley-VCH, Weinheim, 1st edition, 2008. 34

[85] N. Setter, D. Damjanovic, L. Eng, G. Fox, S. Gevorgian, S. Hong, a. Kingon, H. Kohlstedt, N. Y. Park, G. B. Stephenson, I. Stolitchnov, a. K. Taganstev, D. V. Taylor, T. Yamada, and S. Streiffer. **Ferroelectric thin films: Review of materials, properties, and applications**. *Journal of Applied Physics*, **100**(5):051606, 2006. 34

[86] J.M. Slaughter. **Materials for Magnetoresistive Random Access Memory**. *Annual Review of Materials Research*, **39**(1):277–296, August 2009. 34

[87] Leon Chua. **Memristor-the missing circuit element**. *Circuit Theory, IEEE Transactions on*, **CT-18**(5):507–519, 1971. 34, 35

[88] C Schindler and M Meier. **Resistive switching in Ag-Ge-Se with extremely low write currents**. *Non-Volatile Memory ...*, **00**(c):82–85, 2007. 37

[89] J. Y. Son and Y.-H. Shin. **Direct observation of conducting filaments on resistive switching of NiO thin films**. *Applied Physics Letters*, **92**(22):222106, 2008. 38, 39

[90] Jung-Bin Yun, Sejin Kim, Sunae Seo, Myoung-Jae Lee, Dong-Chul Kim, Seung-Eon Ahn, Yongsoo Park, Jiyoung Kim, and Hyunjung Shin. **Random and localized resistive switching observation in Pt/NiO/Pt**. *physica status solidi (RRL) Rapid Research Letters*, **1**(6):280–282, November 2007. 38, 39

[91] S. a. Hayward and E. K. H. Salje. **Cubic-tetragonal phase transition in SrTiO3 revisited: Landau theory and transition mechanism**. *Phase Transitions*, **68**(3):501–522, April 1999. 39

[92] JH Barrett. **Dielectric constant in perovskite type crystals**. *Physical Review*, **86**(1):1950–1952, 1952. 39

[93] JF Schooley, WR Hosler, and ML Cohen. **Superconductivity in Semiconducting SrTiO_3**. *Physical Review Letters*, **12**(17):474–475, 1964. 39

[94] K. van Benthem, C. Elsasser, and R. H. French. **Bulk electronic structure of SrTiO[sub 3]: Experiment and theory**. *Journal of Applied Physics*, **90**(12):6156, 2001. 39

[95] a. Spinelli, M. a. Torija, C. Liu, C. Jan, and C. Leighton. **Electronic transport in doped SrTiO_{3}: Conduction mechanisms and potential applications**. *Physical Review B*, **81**(15):155110, April 2010. 39

[96] Junwoo Son, Pouya Moetakef, Bharat Jalan, Oliver Bierwagen, Nicholas J Wright, Roman Engel-Herbert, and Susanne Stemmer. **Epitaxial SrTiO3 films with electron mobilities exceeding 30,000 cm2 V(-1) s(-1).** *Nature materials*, **9**(6):482–4, June 2010. 39

[97] M Hasan, R Dong, DS Lee, DJ Seong, HJ Choi, MB Pyun, and H Hwang. **A Materials Approach to Resistive Switching Memory Oxides**. *Journal of Semiconductor Technology and Science*, **8**(1):65, 2008. 40

[98] X. B. Yan, Y. D. Xia, H. N. Xu, X. Gao, H. T. Li, R. Li, J. Yin, and Z. G. Liu. **Effects of the electroforming polarity on bipolar resistive switching characteristics of SrTiO[sub 3δ] films**. *Applied Physics Letters*, **97**(11):112101, 2010. 40

[99] K. Szot, R. Dittmann, W. Speier, and R. Waser. **Nanoscale resistive switching in SrTiO3 thin films**. *physica status solidi (RRL) Rapid Research Letters*, **1**(2):R86–R88, March 2007. 40, 130

[100] Deok-Hwang Kwon, Kyung Min Kim, Jae Hyuck Jang, Jong Myeong Jeon, Min Hwan Lee, Gun Hwan Kim, Xiang-Shu Li, Gyeong-Su Park, Bora Lee, Seungwu Han, Miyoung Kim, and Cheol Seong Hwang. **Atomic structure of conducting nanofilaments in TiO2 resistive switching memory.** *Nature nanotechnology*, **5**(2):148–53, February 2010. 41

[101] K. Szot, M Rogala, W Speier, Z Klusek, a Besmehn, and R. Waser. **TiO(2)-a prototypical memristive material.** *Nanotechnology*, **22**(25):254001, June 2011. 41, 83, 99, 115

[102] M. Janousch, G.I. Meijer, U. Staub, B Delley, S.F. Karg, and B.P. Andreasson. **Role of Oxygen Vacancies in Cr-Doped SrTiO3 for Resistance-Change Memory**. *Advanced Materials*, **19**(17):2232–2235, September 2007. 41, 42, 102, 109, 115

[103] EZ Luo, JB Xu, W Wu, IH Wilson, B Zhao, and X Yan. **Identifying conducting phase from the insulating matrix in percolating metal-insulator nanocomposites by conducting atomic force microscopy**. *Applied Physics A*, **1174**(66):1171–1174, 1998. 44

[104] T Carlson. *Photoelectron and Auger Spectroscopy*. Modern Analytical Chemistry. Springer London, Limited, 2012. 48

[105] JC Vickerman and IS Gilmore. *Surface Analysis - The Principal Techniques*. John Wiley & Sons Ltd, 2nd edition, 2009. 51, 53, 74

[106] DA Shirley. **Many-electron and final-state effects: beyond the one-electron picture**. *Photoemission in Solids I*, 1978. 52

[107] S Morita, editor. *Roadmapof Scanning Probe Microscopy*. Springer Science & Business Media, 2006. 53

[108] G. Binnig, CF Quate, and C Gerber. **Atomic force microscope**. *Physical review letters*, **56**(9):930–933, 1986. 54

[109] Y. Martin, C. C. Williams, and H. K. Wickramasinghe. **Atomic force microscopeforce mapping and profiling on a sub 100-A scale**. *Journal of Applied Physics*, **61**(10):4723, 1987. 55

[110] H Takano, J R Kenseth, S S Wong, J C O'Brien, and M D Porter. **Chemical and biochemical analysis using scanning force microscopy.** *Chemical reviews*, **99**(10):2845–90, October 1999. 55

[111] Bharat Bhushan, editor. *Springer Handbook of Nanotechnology*. Springer Berlin Heidelberg, Berlin, Heidelberg, 2004. 59

[112] LB Valdes. **Resistivity measurements on germanium for transistors**. *Proceedings of the IRE*, **29**:1429–1434, 1954. 60

[113] B. Psiuk, J. Szade, H. Schroeder, H. Haselier, M. Mynarczyk, R. Waser, and K. Szot. **Photoemission study of SrTiO3 surface layers instability upon metal deposition**. *Applied Physics A*, **89**(2):451–455, June 2007. 60

[114] K. Szot, B. Reichenberg, F. Peter, R. Waser, and S. Tiedke. **Electrical Characterization of Perovskite Nanostructures by SPM**. In Sergei Kalinin and Alexei Gruverman, editors, *Scanning Probe Microscopy*, pages 746–775. Springer New York, 2007. 62

[115] M. Wojtyniak, K. Szot, and R. Waser. **The thermal stability of Pt/Ir coated AFM tips for resistive switching measurements**. *Applied Surface Science*, **257**(17):7627–7632, June 2011. 63

[116] A. Gruverman, O. Kolosov, J. Hatano, K. Takahashi, and H. Tokumoto. **Domain structure and polarization reversal in ferroelectrics studied by atomic force microscopy**. *Journal of Vacuum Science & Technology B: Microelectronics and Nanometer Structures*, **13**(3):1095, May 1995. 64

[117] M Nonnenmacher, M. P. OBoyle, and H. K. Wickramasinghe. **Kelvin probe force microscopy**. *Appl. Phys. Lett.*, **58**(25):2921–2923, 1991. 64

[118] Yves Martin, D.W. Abraham, and H.K. Wickramasinghe. **High-resolution capacitance measurement and potentiometry by force microscopy**. *Applied Physics Letters*, **52**(13):1103–1105, 2009. 64

[119] Manuel Palacio and Bharat Bhushan. **Nanomechanical and nanotribological characterization of noble metal-coated AFM tips for probe-based ferroelectric data recording**. *Nanotechnology*, **19**(10):105705, March 2008. 64

[120] Bharat Bhushan and Kwang Joo Kwak. **Platinum-coated probes sliding at up to 100 mm s 1 against coated silicon wafers for AFM probe-based recording technology**. *Nanotechnology*, **18**(34):345504, August 2007. 64

[121] Bharat Bhushan, Manuel Palacio, and Kwang Joo Kwak. **Thermally-treated Pt-coated silicon AFM tips for wear resistance in ferroelectric data storage**. *Acta Materialia*, **56**(16):4233–4241, September 2008. 64

[122] G M Sacha, M Cardellach, J J Segura, J Moser, a Bachtold, J Fraxedas, and a Verdaguer. **Influence of the macroscopic shape of the tip on the contrast in scanning polarization force microscopy images.** *Nanotechnology*, **20**(28):285704, July 2009. 65

[123] S. Doniach and M. Sunjic. **Many-electron singularity in x-ray photoemission andx-ray line spectra from metals**. *J. Phys. C: Solid State Phys.*, **3**:285–291, May 1970. 66

[124] A. Hiraki. **Low temperature reactions at Si/metal interfaces; What is going on at the interfaces?** *Surface Science Reports*, **3**(7):357–412, 1983. 66, 70

[125] PJ Grunthaner, FJ Grunthaner, and A. **Chemical bonding and charge redistribution: Valence band and core level correlations for the Ni/Si, Pd/Si, and Pt/Si systems**. *Journal of Vacuum*, **20**:680, 1982. 66

[126] L. Kövér, J. Tóth, and L. Dávid. **XPS investigation of Pt-Si interfaces formed during heat treatments in different (H2, O2) atmospheres**. *Vacuum*, **37**(1-2):125–127, 1987. 67

[127] R.M. Tiggelaar, R.G.P. Sanders, a.W. Groenland, and J.G.E. Gardeniers. **Stability of thin platinum films implemented in high-temperature microdevices**. *Sensors and Actuators A: Physical*, **152**(1):39–47, May 2009. 67

[128] J Yin, W Cai, Y Zheng, and L Zhao. **Effect of Pt film thickness on PtSi formation and film surface morphology**. *Surface and Coatings Technology*, **198**(1-3):329–334, August 2005. 67

[129] J Lee and B Kim. **Thermal dewetting of Pt thin film: Etch-masks for the fabrication of semiconductor nanostructures**. *Materials Science and Engineering: A*, **449-451**:769–773, March 2007. 67

[130] WG Rothschild, HC Yao, and HK Plummer Jr. **Surface interaction in the Pt - Al2O3 system. V: Effects of atmosphere and fractal topology on the sintering of Pt**. *Langmuir*, **2**(5):588–593, 1986. 70

[131] M Chen and L D Schmidt. **Morphology and sintering of Pt crystallites on amorphous SiO2**. *Journal of Catalysis*, **55**(3):348–360, 1978. 70

[132] D. B. Poker and C. E. Klabunde. **Temperature dependence of electrical resistivity of vanadium, platinum, and copper**. *Physical Review B*, **26**(12):7012–7014, 1982. 70

BIBLIOGRAPHY

[133] B E Warren. *X-ray Diffraction*. Addison-Wesley series in metallurgy and materials. Dover Publications, 1969. 72

[134] B D Cullity and S R Stock. *Elements of x-ray diffraction*. Pearson education. Prentice Hall, 2001. 72

[135] MichelA. Hove. **Low-energy electron diffraction Experiment and theory**. In P Grosse, editor, *Festkörperprobleme 25 SE - 68*, **25** of *Advances in Solid State Physics*, pages 517–522. Springer Berlin Heidelberg, 1985. 73

[136] B Beckhoff, B Kanngie_er, N Langhoff, R Wedell, and H Wolff. *Handbook of Practical X-Ray Fluorescence Analysis*. SpringerLink : B{ü}cher. Springer, 2007. 76

[137] Stephen Blundell. *Magnetism in condensed matter*. Oxford University Press, 2001. 77

[138] D P E Dickson and F J Berry. *M{ö}ssbauer Spectroscopy*. Cambridge University Press, 2005. 78

[139] G. Margaritondo. **Photoelectron spectromicroscopy and spectronanoscopy at synchrotrons: Growing impact on life sciences and materials science**. *Journal of Electron Spectroscopy and Related Phenomena*, **178-179**:273–291, May 2010. 79

[140] Doo Seok Jeong, Reji Thomas, R S Katiyar, J F Scott, H Kohlstedt, a Petraru, and Cheol Seong Hwang. **Emerging memories: resistive switching mechanisms and current status.** *Reports on progress in physics. Physical Society (Great Britain)*, **75**(7):076502, July 2012. 83

[141] D. Kajewski, R. Wrzalik, M. Wojtyniak, M. Pilch, J. Szade, K. Szot, Ch. Lenser, R. Dittmann, and R. Waser. **Local conductivity of epitaxial Fe-doped SrTiO 3 thin films**. *Phase Transitions*, **84**(5-6):483–488, May 2011. 83

[142] X. G. Chen, X. B. Ma, Y. B. Yang, L. P. Chen, G. C. Xiong, G. J. Lian, Y. C. Yang, and J. B. Yang. **Comprehensive study of the resistance switching in SrTiO[sub 3] and Nb-doped SrTiO[sub 3]**. *Applied Physics Letters*, **98**(12):122102, 2011. 84

[143] K. Szot and W Speier. **Surfaces of reduced and oxidized SrTiO_ {3} from atomic force microscopy**. *Physical Review B*, **60**(8):5909–5926, 1999. 84

[144] Agnieszka Leonarska, K. Szot, and Alicja Ratuszna. **Temperature evolution of the crystal structure in SrTiO 3 doped by W 6+ , Ni 3+ , Fe 3+ and La 3+**. *Phase Transitions*, **84**(11-12):1015–1027, November 2011. 84

[145] P. Adler, a. Lebon, V. Damljanović, C. Ulrich, C. Bernhard, a. Boris, a. Maljuk, C. Lin, and B. Keimer. **Magnetoresistance effects in SrFeO3δ: Dependence on phase composition and relation to magnetic and charge order**. *Physical Review B*, **73**(9):1–50, March 2006. 86

[146] Masashi Kawasaki, K Takahashi, and Tatsuro Maeda. **Atomic control of the SrTiO3 crystal surface**. *Science*, **266**:1–3, 1994. 87

[147] John Paul Strachan, Matthew D Pickett, J Joshua Yang, Shaul Aloni, A L David Kilcoyne, Gilberto Medeiros-Ribeiro, and R Stanley Williams. **Direct Identification of the Conducting Channels in a Functioning Memristive Device**. *Advanced Materials*, **22**(32):3573–3577, 2010. 90

[148] Avner Rothschild, Wolfgang Menesklou, Harry L Tuller, and Ellen Ivers-Tiffée. **Electronic Structure, Defect Chemistry, and Transport Properties of SrTi 1 - x Fe x O 3 - y Solid Solutions**. *Chemistry of Materials*, **18**(16):3651–3659, August 2006. 93

[149] K. Szot, W. Speier, J. Herion, and Ch. Freiburg. **Restructuring of the surface region in SrTiO 3**. *Applied Physics A: Materials Science & Processing*, **64**(1):55–59, December 1996. 96, 119, 129

[150] A. Kohl, D. Kajewski, Jerzy Kubacki, Ch. Lenser, Regina Dittmann, P. Meuffels, K. Szot, R. Waser, and J. Szade. **Detection of Fe(2+) valence states in Fe doped SrTiO3 epitaxial thin films grown by pulsed laser deposition.** *Physical chemistry chemical physics : PCCP*, **15**(21):8311–7, June 2013. 98

[151] K. Szot, W. Speier, and W. Eberhardt. **Microscopic nature of the metal to insulator phase transition induced through electroreduction in single-crystal KNbO3**. *Applied Physics Letters*, **60**(10):1190, 1992. 99

[152] G A Cox and R H Tredgold. **Time dependence of the electrical conductivity in strontium titanate single crystals**. *British Journal of Applied Physics*, **16**(4):427, 1965. 99

[153] Joseph Blanc and David L Staebler. **Electrocoloration in SrTiO3: Vacancy Drift and Oxidation-Reduction of Transition Metals**. *Phys. Rev. B*, **4**(10):3548–3557, 1971. 99, 102, 103

[154] R. Waser, Tudor Baiatu, and Karl-Heinz Hardt. **dc Electrical Degradation of PerovskiteType Titanates: I, Ceramics**. *J. Am. Ceram. Soc.*, **73**(6):1645–53, 1990. 99

[155] Ingrid Denk, J Claus, and J Maier. **Electrochemical investigations of SrTiO3 boundaries**. *Journal of the Electrochemical Society*, **144**(10):3526–3536, 1997. 100

[156] M. Wojtyniak, K. Szot, R. Wrzalik, C. Rodenbucher, G. Roth, and R. Waser. **Electro-degradation and resistive switching of Fe-doped SrTiO3 single crystal**. *Journal of Applied Physics*, **113**(8):083713, 2013. 101

[157] D M Smyth. **Defects and Order in Perovskite-Related Oxides**. *Annual Review of Materials Science*, **15**(1):329–357, August 1985. 102

[158] Zoltan J. Kiss. **PHOTOCHROMICS**. *Physics Today*, **23**(1):42, 1970. 103

[159] J. Joshua Yang, Matthew D Pickett, Xuema Li, Douglas a a Ohlberg, Duncan R Stewart, and R Stanley Williams. **Memristive switching mechanism for metal/oxide/metal nanodevices.** *Nature nanotechnology*, **3**(7):429–33, July 2008. 105

[160] S Timoshenko and S Woinowsky-Krieger. *Theory of plates and shells*. Engineering societies monographs. McGraw-Hill, 1959. 105

[161] A.L. Romasco, L.H. Friedman, L. Fang, R.a. Meirom, T.E. Clark, R.G. Polcawich, J.S. Pulskamp, M. Dubey, and C.L. Muhlstein. **Deformation behavior of nanograined platinum films**. *Thin Solid Films*, **518**(14):3866–3874, May 2010. 106

[162] Giorgio Soave. **Equilibrium constants from a modified Redlich-Kwong equation of state**. *Chemical Engineering Science*, **27**(6):1197–1203, 1972. 106

[163] G Liessmann, W Schmidt, and S Reiffarth. **Data compilation of the Saechsische Olefinwerke Boehlen**. Technical report, 1995. 106

[164] R. Schmiedl, V. Demuth, P. Lahnor, H. Godehardt, Y. Bodschwinna, C. Harder, L. Hammer, H.-P. Strunk, M. Schulz, and K. Heinz. **Oxygen diffusion through thin Pt films on Si(100)**. *Applied Physics A: Materials Science & Processing*, **62**(3):223–230, February 1996. 106

[165] Ingrid Denk, Frank Noll, and Joachim Maier. **In situ Profiles of Oxygen Diffusion in SrTiO3: Bulk Behavior and Boundary Effects**. *Journal of the American Ceramic Society*, **80**(2):279–285, 1997. 111

[166] I.G. Baek, M.S. Lee, S. Sco, M.J. Lee, D.H. Seo, D.-S. Suh, J.C. Park, S.O. Park, H.S. Kim, I.K. Yoo, U.-I. Chung, and J.T. Moon. **Highly scalable non-volatile resistive memory using simple binary oxide driven by asymmetric unipolar voltage pulses**. In *IEDM Technical Digest. IEEE International Electron Devices Meeting, 2004.*, pages 587–590. IEEE. 115

[167] Hisashi Shima, Fumiyoshi Takano, Hiro Akinaga, Yukio Tamai, Isao H. Inoue, and Hide Takagi. **Resistance switching in the metal deficient-type oxides: NiO and CoO**. *Applied Physics Letters*, **91**(1):012901, 2007. 115

[168] I. Inoue, S. Yasuda, H. Akinaga, and H. Takagi. **Nonpolar resistance switching of metal/binary-transition-metal oxides/metal sandwiches: Homogeneous/inhomogeneous transition of current distribution**. *Physical Review B*, **77**(3):035105, January 2008. 115

[169] David P. Norton. **Synthesis and properties of epitaxial electronic oxide thin-film materials**. *Materials Science and Engineering: R: Reports*, **43**(5-6):139–247, March 2004. 116

[170] a. Inam, M. S. Hegde, X. D. Wu, T. Venkatesan, P. England, P. F. Miceli, E. W. Chase, C. C. Chang, J. M. Tarascon, and J. B. Wachtman. **As-deposited high Tc and Jc superconducting thin films made at low temperatures**. *Applied Physics Letters*, **53**(10):908, 1988. 116

[171] X. D. Wu, R. E. Muenchausen, S. Foltyn, R. C. Estler, R. C. Dye, C. Flamme, N. S. Nogar, a. R. Garcia, J. Martin, and J. Tesmer. **Effect of deposition rate on properties of YBa2Cu3O7δ superconducting thin films**. *Applied Physics Letters*, **56**(15):1481, 1990. 117

[172] Jeffrey T. Cheung and Haluk Sankur. **Growth of thin films by laser-induced evaporation**. *Critical Reviews in Solid State and Materials Sciences*, **15**(1):63–109, January 1988. 117

[173] EV Pechen, A. V. Varlashkin, S. I. Krasnosvobodtsev, B. Brunner, and K. F. Renk. **Pulsed-laser deposition of smooth high-Tc superconducting films using a synchronous velocity filter**. *Applied physics ...*, **66**(April):2292–2294, 1995. 118

[174] B. Holzapfel, B. Roas, L. Schultz, P. Bauer, and G. Saemann-Ischenko. **Off-axis laser deposition of YBa2Cu3O7δ thin films**. *Applied Physics Letters*, **61**(26):3178, 1992. 118

[175] Z. Trajanovic, S. Choopun, R. P. Sharma, and T. Venkatesan. **Stoichiometry and thickness variation of YBa[sub 2]Cu[sub 3]O[sub 7x] in pulsed laser deposition with a shadow mask**. *Applied Physics Letters*, **70**(25):3461, 1997. 118

[176] A Benninghoven, F G Rudenauer, and H W Werner. *Secondary Ion Mass Spectrometry: Basic Concepts, Instrumental Aspects, Applications and Trends*. Chemical Analysis: A Series of Monographs on Analytical Chemistry and Its Applications. John Wiley & Sons, 1987. 119

[177] M. Khalid, a. Setzer, M. Ziese, P. Esquinazi, D. Spemann, a. Pöppl, and E. Goering. **Ubiquity of ferromagnetic signals in common diamagnetic oxide crystals**. *Physical Review B*, **81**(21):214414, June 2010. 124

[178] Yongjia Zhang, Jifan Hu, Ensi Cao, Li Sun, and Hongwei Qin. **Vacancy induced magnetism in SrTiO3**. *Journal of Magnetism and Magnetic Materials*, **324**(10):1770–1775, May 2012. 124

[179] A D Caviglia, S Gariglio, N Reyren, D Jaccard, T Schneider, M Gabay, S Thiel, G Hammerl, J Mannhart, and J.-M. Triscone. **Electric field control of the LaAlO3/SrTiO3 interface ground state**. *Nature*, **456**(7222):624–627, December 2008. 124

[180] M. Egilmez, G. W. Leung, a. M. H. R. Hakimi, and M. G. Blamire. **Origin of magnetism in La and Fe doped SrTiO[sub 3δ] films**. *Journal of Applied Physics*, **108**(12):123912, 2010. 124

[181] Hyun-Suk Kim, Lei Bi, G. F. Dionne, and C. a. Ross. **Magnetic and magneto-optical properties of Fe-doped SrTiO[sub 3] films**. *Applied Physics Letters*, **93**(9):092506, 2008. 125

[182] Peter Adler and Sten Eriksson. **Structural Properties, Mössbauer Spectra, and Magnetism of Perovskite-Type Oxides SrFe1-xTixO3-y**. *Zeitschrift für anorganische und allgemeine Chemie*, **626**(1):118–124, January 2000. 126

[183] J F Kenney and E S Keeping. *Mathematics of statistics*. Number pkt 2 in Mathematics of Statistics. Van Nostrand, 1947. 128

[184] NA Surplice. **The electrical conductivity of calcium and strontium oxides**. *British Journal of Applied Physics*, **175**, 1966. 129

BIBLIOGRAPHY

[185] C. Rossel, G. I. Meijer, D. Bremaud, and D. Widmer. **Electrical current distribution across a metalinsulatormetal structure during bistable switching**. *Journal of Applied Physics*, **90**(6):2892, 2001. 130

[186] Xin Chen, NaiJuan Wu, John Strozier, and Alex Ignatiev. **Spatially extended nature of resistive switching in perovskite oxide thin films**. *Applied Physics Letters*, **89**(6):063507, 2006. 130

[187] M. Rozenberg, I. Inoue, and M. Sánchez. **Nonvolatile Memory with Multilevel Switching: A Basic Model**. *Physical Review Letters*, **92**(17):1–4, April 2004. 130

[188] J Padilla and D Vanderbilt. **Ab-initio study of SrTiO3 surfaces**. *Arxiv preprint cond-mat/9802207*, **56**(3):1625–1631, 1998. 135

In the very end, the word cloud made of individually sized and colored words is presented. The highlight is based on the frequencies of occurrence within the body of text. Enjoy!